Micro-cavity optimization for single ion fluorescence detection

Abdelatief, Abdullah

2025

Document Version:
Publisher's PDF, also known as Version of record

Link to publication

Citation for published version (APA):
Abdelatief, A. (2025). *Micro-cavity optimization for single ion fluorescence detection*. Atomic Physics, Department of Physics, Lund University.

Total number of authors:
1

LUND UNIVERSITY

PO Box 117
221 00 Lund
+46 46-222 00 00

Micro-cavity optimization for single ion fluorescence detection

ABDULLAH ABDELATIEF
DEPARTMENT OF PHYSICS | FACULTY OF ENGINEERING, LTH | LUND UNIVERSITY

Micro-cavity optimization for single ion fluorescence detection

Micro-cavity optimization for single ion fluorescence detection

Abdullah Abdelatief

LUND UNIVERSITY

Thesis for the degree of Doctor of Philosophy
Thesis advisors: Dr. Andreas Walther, Dr. Adam Kinos
Faculty opponent: Dr. Brian Julsgaard

With the permission of the Faculty of Engineering at Lund University, the thesis will be publicly defended on Friday, the 21th of February 2025 at 9.15 a.m. in Rydberg's Hall, at the Department of Physics, Professorsgatan 1, Lund.

Organization:
LUND UNIVERSITY
Department of Physics
BOX 118
SE-221 00 LUND
Sweden

Document name:
DOCTORAL DISSERTATION

Date of disputation
2025-02-21

Author(s):
Abdullah Abdelatief

Sponsring organization:

Title and subtitle:
Micro-cavity optimization for single ion fluorescence detection

Abstract:

This thesis describes the work done on two open access microcavities that aims at detecting single rare-earth ions for quantum information applications. The initial microcavity faced mechanical instability due to its geometry, which limited robust design possibilities due to the 25 mm diameter space of the helium bath cryostat. A Purcell enhancement of 2.2 was realized for nanoparticles at 2.1 K, compared to an estimated enhancement of 18. The observed decrease in Purcell enhancement is attributed to the root mean square (rms) cavity length fluctuations, which resulted in a time-averaged Purcell effect. A cavity length jitter of 4 linewidths has been observed to cause significant fluctuations in the detected fluorescence signal, which hinders the detection of single ions, particularly in scenarios with low Purcell enhancement. Consequently, approximately 7 ions affect the fluorescence measurements. Nevertheless, our focus is on single ion detection, which is essential for quantum computer applications (see Chapter 8). In my thesis project, I focused on developing a new microcavity assembly to resolve the issues associated with the previous design. The mechanical design is detailed in Chapter 5, while Chapter 6 addresses the stability measurements. The objective of the new assembly is to attain high mechanical stability within a closed-cycle cryostat, providing sufficient space for a robust design and minimizing photon leakage from the stabilization beam to the fluorescence detection system. This integration enables the use of a continuous wave laser for stabilization, which contributes to reduced cavity length fluctuations during fluorescence collection and enhances the Purcell effect. To attain a significant degree of mechanical stability while minimizing error photons, higher-order modes, particularly those with odd indices, are employed as a stabilization beam. This approach is effective because odd-indexed higher-order modes exhibit minimal overlap with the single-mode fiber used for sample probing and fluorescence collection. Chapter 4 analyzes suppression in coupling efficiency due to odd-indexed higher-order modes, ranging from 10 to 10^2, depending on excited mode and cavity length. A challenge associated with higher-order modes is the diffraction loss resulting from the finite diameter of the fiber mirror, which is dependent on the mode order. This aspect is essential when employing higher-order modes for stabilization, as the cavity length stabilization depends on the slope of the fringe side used for stabilization. A cavity finesse of 1600 was measured for the TEM_{00} and TEM_{10} locking beams. In contrast, the finesse measurements for other higher-order modes showed a finesse of 800 for TEM_{30} and 400 for TEM_{50}, attributed to diffraction losses. The associated root mean square (rms) cavity length jitters ranged from 1.5 pm to 2.5 pm measured at room temperature and using side-of-fringe locking. A threefold improvement in stability has been achieved through the implementation of a tilt locking scheme, which can be attributed to the observed steeper slope. At a temperature of 10 K, a cavity length jitter of 15 pm has been measured using side-of-fringe locking. This increase in length fluctuation is primarily due to noise from the closed cycle cryostat, predominantly arising from the vibration noise generated by the pulse tube cryocooler. For the measured length fluctuations an enhancement of an effective Purcell factor of 15 is anticipated with the second generation microcavity assembly. This enhancement allows for excitation power levels below 100 nW, significantly reducing power broadening from 36 MHz to under 1 MHz. Since this is factor is less than the 7 ions we can currently resolve, we can expect that a single rare-earth ion should be resolvable with the current setup.

Key words:
Single rare-earth ion, quantum computing, microcavity, closed-cycle cryostat, cavity stabilization

Classification system and/or index terms (if any)

Supplementary bibliographical information

Language
English

ISSN and key title: 0281-2762, Lund Reports on Atomic Physics, LRAP-582

ISBN:
978-91-8104-366-2 (print)
978-91-8104-367-9 (PDF)

Recipient's notes

Number of pages:
161

Price

Security classification

Signature

Date

Micro-cavity optimization for single ion fluorescence detection

Abdullah Abdelatief

LUND UNIVERSITY

Faculty of Engineering, Department of Physics

ISBN: 978-91-8104-366-2 (print)
ISBN: 978-91-8104-367-9 (PDF)

ISSN: 0281-2762, Lund Reports on Atomic Physics, LRAP-582

Printed in Sweden by Media-Tryck, Lund University

Lund 2025

NORDIC SWAN ECOLABEL
Printed matter
3041 0903

Media-Tryck is a Nordic Swan Ecolabel certified provider of printed material. Read more about our environmental work at www.mediatryck.lu.se

MADE IN SWEDEN

Dedicated to
my father, mother, and wife

Table of Contents

Abstract **12**

Author's contributions **14**

Publications included in this thesis 14

Publications Not Included in this Thesis 15

Popular Scientific Summary **17**

1 Introduction **19**

1.1 Quantum computer platforms 19

1.2 Readout challenges with single rare-earth ions 20

1.3 Story of my thesis project 21

1.4 Outline of this thesis 22

2 Rare-Earth Ions and their Experimental Setup **24**

2.1 Rare-earth ion properties 24

2.1.1 Electronic configuration 24

2.1.2 Energy level structure 25

2.1.3 Homogenous and inhomogeneous linewidth 27

2.1.4 Key features of RE-ions for quantum computing 29

2.1.5 Readout scheme 29

2.1.6 Potential materials for cavity integration 30

2.2 Cryostats 31

2.3 Light sources 32

3 Fundamental Concepts of Light-Matter Interactions **34**

3.1 Closed quantum system 34

3.2 Open quantum system: Dissipation process 38

3.2.1 Quantum Master Equation 38

3.2.2 Solving the Master Equation 39

3.2.3 Coupling regimes 39

3.3 Enhancement of spontaneous emissions: Purcell Effect 41

3.3.1 Consideration of enhancement in our system 43

3.4 Fluorescence signal and power broadening 43

4 Optical Properties of Fiber-Based Microcavities 46

4.1 Fiber Fabry-Pérot microcavities 47

4.2 Microcavity Properties 48

4.2.1 Phase 49

4.2.2 Cavity TEM modes 51

4.2.3 ABCD matrix and stability condition 52

4.3 Transverse modes excitations 53

4.4 Diffraction loss 58

4.5 Coupling efficiency 60

4.5.1 Coupling through flat mirror 61

4.5.2 Coupling through fiber mirror 61

4.6 Evaluation of HOMs as a Stabilizing Beam 62

5 Mechanical Modeling and Assembly Design..63

5.1 The challenge 63

5.2 Performance of the first-generation setup 64

5.3 Requirements for improving stability 65

5.4 Implementations to the new design 66

5.4.1 Enhancing rigidity. 66

5.4.2 Stable moving components 66

5.5 New mechanical modelling 67

5.5.1 Material choices 68

5.5.2 Positioners 69

5.5.3 Spring systems 71

5.6 Assembly frequency response 72

6 Micro-cavity length stabilization 74

6.1 Cavity Assembly setup 74

6.1.1 Cavity building 74

....75

6.1.2 Cavity mirrors and coatings 76

6.1.3 Optical setup 76

6.1.4 Data acquisition 77

6.2 Experimental methods 78

6.2.1 Using higher order modes for cavity length stabilization 78

6.2.2 Doubly-resonant cavity 79

6.2.3 Measuring cavity parameters 80

6.2.4 Conversion factor 84

6.3 Locking schemes 84

6.3.1 Pound-Drever-Hall (PDH) 84
6.3.2 Side-of-fringe 85
6.3.3 Tilt locking 85
6.4 Feedback locking circuit analysis 86
6.4.1 Circuit performance 88
6.4.2 Noise suppression using feedback circuit 88
6.4.3 Noise amplitude analysis 89
6.5 Evaluating circuit performance at room temperature 90
6.5.1 Noise analysis 91
6.6 Error photon suppression 92
6.7 Stability in a closed-cycle cryostat 94
6.7.1 Pulse tube cryocooler noises 95
6.7.2 Microcavity performance in closed-cycle cryostat 95
6.8 How does the stability compare to other fiber cavity setups? 98
7 Neodymium as a readout ion 100
7.1 Single-readout ion and qubit ion requirements 100
7.2 Spectroscopic properties of Nd^{3+} doped Y_2O_3 102
7.2.1 A non-transparent ceramic 102
7.2.2 Nanocrystals in powder 102
7.3 Readout fidelity estimations 103
7.4 Scanning Cavity Microscopy 104
7.4.1 Sample preparations 104
7.4.2 Identification of Nd^{3+} nanoparticles 105
7.5 Room temperature measurements 106
7.5.1 Extinction measurements 106
7.5.2 Fluorescence detection 107
7.6 Cryogenic measurements 109
7.6.1 Purcell enhancement 111
7.6.2 Excited ions estimations 112
7.6.3 Power broadening and targeted ions estimations 112
8 Quantum Computer requirements and Outlook 114
8.1 Materials 115
8.2 Readout 116
8.2.1 Purcell enhancement: challenges and improvements 116
8.2.2 Optical coupling efficiency 119
8.3 Single-qubit gate operation 121
8.3.1 Integrated cavity with a thin film 122
8.4 Two-qubit gate operation 122

8.5 Processor nodes 123
8.6 Many nodes 123
Acknowledgments...**124**
References **125**
Research papers

Abstract

This thesis describes the work done on two open access microcavities that aims at detecting single rare-earth ions for quantum information applications.

The initial microcavity faced mechanical instability due to its geometry, which limited robust design possibilities due to the 25 mm diameter space of the helium bath cryostat. A Purcell enhancement of 2.2 was realized for nanoparticles at 2.1 K, compared to an estimated enhancement of 18. The observed decrease in Purcell enhancement is attributed to the root mean square (rms) cavity length fluctuations, which resulted in a time-averaged Purcell effect. A cavity length jitter of 4 linewidths has been observed to cause significant fluctuations in the detected fluorescence signal, which hinders the detection of single ions, particularly in scenarios with low Purcell enhancement. Consequently, approximately 7 ions affect the fluorescence measurements. Nevertheless, our focus is on single ion detection, which is essential for quantum computer applications (see Chapter 8).

In my thesis project, I focused on developing a new microcavity assembly to resolve the issues associated with the previous design. The mechanical design is detailed in Chapter 5, while Chapter 6 addresses the stability measurements. The objective of the new assembly is to attain high mechanical stability within a closed-cycle cryostat, providing sufficient space for a robust design and minimizing photon leakage from the stabilization beam to the fluorescence detection system. This integration enables the use of a continuous wave laser for stabilization, which contributes to reduced cavity length fluctuations during fluorescence collection and enhances the Purcell effect.

To attain a significant degree of mechanical stability while minimizing error photons, higher-order modes, particularly those with odd indices, are employed as a stabilization beam. This approach is effective because odd-indexed higher-order modes exhibit minimal overlap with the single-mode fiber used for sample probing and fluorescence collection. Chapter 4 analyzes suppression in coupling efficiency due to odd-indexed higher-order modes, ranging from 10 to 100, depending on excited mode and cavity length.

A challenge associated with higher-order modes is the diffraction loss resulting from the finite diameter of the fiber mirror, which is dependent on the mode order. This aspect is essential when employing higher-order modes for stabilization, as the cavity length stabilization depends on the slope of the fringe side used for

stabilization. A cavity finesse of 1600 was measured for the TEM_{00} and TEM_{10} locking beams. In contrast, the finesse measurements for other higher-order modes showed a finesse of 800 for TEM_{30} and 400 for TEM_{50}, attributed to diffraction losses. The associated root mean square (rms) cavity length jitters ranged from 1.5 pm to 2.5 pm measured at room temperature and using side-of-fringe locking. A threefold improvement in stability has been achieved through the implementation of a tilt locking scheme, which can be attributed to the observed steeper slope.
At a temperature of 10 K, a cavity length jitter of 15 pm rms has been measured using side-of-fringe locking. This increase in length fluctuation is primarily due to noise from the closed cycle cryostat, predominantly arising from the vibration noise generated by the pulse tube cryocooler. For the measured length fluctuations an enhancement of an effective Purcell factor of 15 is anticipated with the second generation microcavity assembly. This enhancement allows for excitation power levels below 100 nW, significantly reducing power broadening from 36 MHz to under 1 MHz. Since this is factor is less than the 7 ions we can currently resolve, we can expect that a single rare-earth ion should be resolvable with the current setup.

Author’s contributions

Publications included in this thesis

Paper I

Micro-cavity length stabilization for fluorescence enhancement using schemes based on higher order spatial modes

A. Shehata Abdelatief, A. J. Renders, M. Alqedra, J. J. Hansen, D. Hunger, L. Rippe, and A. Walther

Submitted.

I prepared and performed the experiments, analyzed the data and carried out the necessary calculations. Additionally, I simulated the stabilization feedback circuit and I wrote the manuscript.

Paper II

Optical coherence properties of nanoscale Kramers’ rare-earth ions for quantum applications.

Mohammed K. Alqedra*, Chetan Deshmukh*, Sebastian P. Horvath, Safi Rafie-Zinedine, Abdullah Abdelatief, Lars Rippe, Stefan Kröll, Andreas Walther, Bernardo Casabone, Hugues de Riedmatten, Diana Serrano, Shuping Liu, Alban Ferrier, Alexandre Tallaire, Hugues de Riedmatten, and Philippe Goldner;

Published in *Phys.review B.*

I assisted in the preparation of experiments, the configuration and alignment of the optical setup, and the data collection related to the Nd^{3+} ion in collaboration with Mohammed. The ICFO group performed the experiments and analysis on Er^{3+} and Paris group provided the nanocrystals and performed the initial material characterization.

Publications Not Included in this Thesis

Paper 1:

Method for an accurate measurement of nonlinear refractive index in the case of high-repetition-rate femtosecond laser pulses.

Abdullah Shehata, and Tarek Mohamed;

Published in *Optical Society of America B 36(5):1264-1251*.

I prepared and performed the experiments and analyzed the data and carried out calculations and I wrote the manuscript.

Paper 2:

Design of an optical trap for storing femtosecond laser pulses

Abdullah Shehata, Vladimir Chvykov, Reinhold Schuch, and Tarek Mohamed;

Published in *Appl. Opt. 57, 1212-1217*.

I performed the necessary calculations, analyzed the data and I wrote the manuscript.

Paper 3:

Cobalt enhanced nonlinear optical properties and optical limiting of zinc oxide irradiated by femtosecond laser pulses

Abdullah Shehata, Wael Z.Tawfik, and Tarek Mohamed;

Published in *Optical Society of America B 37(11): A1*.

I conducted the experiments, analyzed the resulting data, performed the necessary calculations, and I wrote the manuscript.

Paper 4:

Experimental investigations of nonlinear optical properties of soda-lime glasses and theoretical study of self-compression of fs laser pulse

Abdullah Shehata, Mona Ali, Reinhold Schuch, and Tarek Mohamed;

Published in *Opt. Laser Technol. 116, 276–283.*

I conducted the experiments, analyzed the resulting data, performed the necessary calculations, and I wrote the manuscript.

Paper 5:

Measuring the nonlinear optical properties of indium tin oxide thin film using femtosecond laser pulses

Mona Ali, Abdullah Shehata, Mohamed Ashour, Wael Z. Tawfik, Reinhold Schuch, and Tarek Mohamed;

Published in *Optical Society of America B 37(11): A139-A146*

I assisted in the preparation of experiments, and the data collection and assisted in the first draft.

Popular Scientific Summary

In an attempt to harness the power of quantum mechanics — the principles initially formulated to explain the behavior of light-matter interaction — we have made use of the coherent nature of atoms. This understanding has been applied to create innovative technologies like lasers, transistors, and semiconductors. Currently, we are witnessing the second quantum revolution, which is moving from observation to the realization of innovative quantum technologies exploiting true quantized states. A pivotal aspect of this evolution involves instances where quantum computers can execute calculations that exceed the capabilities of classical, leading to major breakthroughs. Quantum computers have a special benefit because they rely on the concept that quantum particles can exist in multiple states until they are measured, known as 'superposition'. Additionally, they take advantage of the ability of quantum systems to be linked together over long distances without needing to be physically connected, known as 'entanglement'. Maintaining quantum superposition and entanglement require well-isolated systems against environmental noise. One material that can achieve this is rare-earth ions embedded in crystals. These materials can hold quantum information for long durations when kept at very low temperatures. However, it is challenging to retrieve qubit states due to their prolonged excited states, leading to a very low emission rate. The atomic emission rate, a crucial property of matter, is influenced by interactions between atoms and their surrounding vacuums, largely influenced by the local environment. This phenomenon can be manipulated by positioning rare-earth ions within mirrors that create an optical cavity, which alters the density of the photonic vacuum states. This alteration has the potential to improve the rates of spontaneous emission, a phenomenon referred to as the Purcell effect, which may subsequently increase the speed at which information is extracted from the ion. Furthermore, high-performance quantum computing requires an extensive search of particular materials with good optical coherence characteristics.

The work in this thesis is focused on the development of a cavity consisting of two highly reflective mirrors that are spaced by a few microns of vacuum gap, which allows for the insertion of a diverse range of materials. The difficulty associated with this type of cavity lies in its susceptibility to external vibrational noise, including acoustic interference and thermal contractions that occur when cooling down to low temperatures necessary for good ion coherence. The presence of disturbances can interfere with the on-resonance excitation of ions, resulting in a deterioration of the information collected from them. To address this issue, we construct a highly rigid framework for housing the cavity components, which must possess a strong ability to mitigate external noise while allowing the stable and faster transverse scan of cavity mirrors to locate good ions. Additionally, we explored different stabilization protocols that can ensure on-resonance interactions with the narrow linewidth of the emitter over extended durations. The work in this thesis is also aimed at improving the performance of single photon detection utilized in quantum information processing and computing by reducing error photons from the stabilizing beam, leaking during measurements. Furthermore, we also explore new nanomaterials that can fit into the small scales of this cavity. These findings are crucial for showcasing a single-photon source that relies on a highly localized single ion within an optical cavity, utilizing rare-earth ions, which is a promising platform for the implementation of quantum computing to address the demanding challenges in this field.

1 Introduction

In the early 20th century, Einstein pointed out that quantum theory predicts a spookiness in understanding quantum entanglement, prompting him to describe it as "spooky action at a distance" [1]. Entanglement is a fundamental concept of quantum mechanics that describes a shared quantum state, between two or more quantum systems, such as a photon or an atom, even if they are separated by a large distance. Superposition is another important aspect of quantum mechanics because it allows a quantum system to exist in two states at the same time. The basic building block in a quantum information-carrying system is known as a quantum bit, or qubit, and is the key element of all quantum computations. After Richard Feynman's lectures in 1982 on the potential benefits of computing with quantum systems, researchers began actively looking at it. In 2022, the Nobel Prize in Physics was awarded to Alain Aspect, John Clauser and Anton Zeilinger, who made ground breaking contributions in understanding quantum entanglement. Today's quantum computers attract the attention of many large companies such as IBM, Intel, and Google, in addition to researchers.
Quantum computers can interfere the results of multiple paths of calculations instead of only manipulating each individually, as in classical computing. These can potentially solve different problems in materials science, drug discovery, and optimization, among others, where the performance of classical computers is insufficient. Furthermore, a quantum network made up of quantum repeaters and quantum computers might allow users to communicate while ensuring the security of sent data using quantum physics principles.

1.1 Quantum computer platforms

Approaches that are being considered as potential quantum computing platforms must meet a set of requirements outlined by DiVincenzo in 2000 [2]. Since Feynman's original thoughts for a quantum computer [3], a variety of technologies have emerged as viable platforms for gate-based quantum computing, including trapped ions [4], superconducting qubits [5], nitrogen-vacancy centers in diamonds [6], and quantum dots [7]. One challenge for researchers is that all platforms have different types of trade-offs and that currently no system is best at everything. For example, superconducting qubits have many qubits and high speed of their gates but short coherence time. Trapped ions have higher fidelities and longer coherence times, but controlling a large number of ions is challenging [4, 8].

As another alternative, rare-earth-ion-doped (REI) crystals have become a promising solid-state quantum system in recent years [9-12], owing to the excellent optical and spin coherence characteristics of the $4f$-$4f$ transitions when cooled to below 4K. This is the topic of this thesis project and the key advantages of RE ions for usage in quantum computing are given in the next chapter.

There are, however, certain challenges to consider. For instance, the technology is relatively less developed, as it has not demonstrated significant progress in comparison to other systems. One of the main reasons for this is that detecting single ions presents considerable difficulties. This subject forms the basis of my thesis and will be examined in greater detail in the subsequent sections.

1.2 Readout challenges with single rare-earth ions

Direct $4f$ readout of single RE ions is difficult due to the weak oscillator strengths (weak fluorescence/long lifetimes) [13, 14]. The emission rate γ_0 of a single isolated RE ion is inversely related to the optical excited state lifetime through the relationship $\gamma_0 = 1/T_1$, where T_1 is the lifetime. A lower T_1 facilitates the emission of a greater number of photons, thereby enhancing the detectability of the single ion needed for quantum computing. Consequently, minimizing T_1 is crucial for achieving effective detection. We therefore have competing interests: low T_1 to make it easier to read out, but long coherence time T_2, which demands a long T_1, to have good qubit properties. To circumvent this trade-off one can use different rare-earth elements as qubit ions and readout ions. In a quantum computer, it is beneficial to use different species for readout and qubit tasks. In this thesis project, co-dopants Nd and Pr are used, where Nd acts as the readout ion and Pr serves as the qubit ion. To improve detection of the readout ion, its emissions are enhanced by placing it in an optical cavity. For qubit ions, adequate operation can be achieved without cavity enhancement.

Fabry-Pérot microcavities can be used to address readout ions inside the lowest-lying 4f–4f transitions to enhance the emission from ensembles of ions and even resolve single ions [15]. Placing ions in a cavity enhances their emission rate by modifying the density of electromagnetic states available to the ions for optical decay into the cavity mode compared to ions in free space, which is known as the Purcell effect [16]. The emission enhancement is manifested by a reduction in the excited state lifetime of the readout ion by increasing the radiative decay rate by a factor F_P, known as the Purcell factor. Another important parameter to consider is the cooperativity (C), which is defined in terms of field decay rates [18]. Cavity-enhancing the decay rate γ might therefore result in a high cooperativity. When C

>> 1, the coherent coupling between emitters and photons leads to near-deterministic atom-photon interactions, making it possible to achieve cavity-based quantum gates [9]. Furthermore, the coupling of the ions to Fabry-Pérot microcavities might also be a promising solution to realize single emitters with a high degree of indistinguishability for quantum networking applications [17].

The cavities with large quality factors and small mode volumes compared to the scale of the optical wavelength help to produce the greatest emission enhancement. Several cavity types have been successful, including those made from a solid block such as ion-beam milled cavities [19], nano-photonic cavities [20], whispering-gallery-mode disc cavities [21], but also open access cavities, such as the Fabry-Pérot microcavities which are the main topic of this thesis [18, 22-27]. Solid cavity types offer stability against vibrations but are limited in material selection due to production methods. In contrast, open access cavities allow any material to fit within the desired microscales, but are harder to stabilize. The open access cavities are therefore crucial for high-performance applications like quantum computing, as good coherence properties often require special material selection, motivating the effort to overcome the stabilization challenge.

1.3 Story of my thesis project

The goal of this thesis project is to detect single RE ions using microcavities. Initially, Y_2O_3 nanocrystals doped with Nd^{3+} ions are employed to investigate the feasibility of Nd^{3+} ions as potential readout ions. The optical properties of these ions are examined through spectroscopic analysis to determine their suitability for this purpose. Subsequently, the nanocrystals are integrated into a fiber-based Fabry-Pérot microcavity by being spin-coated onto the cavity mirror and cooled down, with the aim of enhancing the spontaneous emission from Nd^{3+} readout ion by Purcell effect. Throughout my PhD, I focused on two microcavity assemblies. During my first three years, a first generation of the microcavity assembly was in operation where I detected ~ 7 ions of Nd^{3+} at 2.1 K using a cavity with a finesse of 3400. Achieving the level of single ion detection with the first cavity assembly presented a considerable challenge, primarily due to the mechanical stability required to maintain resonance with the emitter's narrow linewidth over extended durations. Mechanical vibrations contribute to root mean square (rms) jitter in cavity length, which in turn decreased the time-averaged Purcell factor of the system by a factor of 8. This decrease in the Purcell factor complicates the process of detecting single ions. The assembly was sensitive toward low frequency vibrations. This made it challenging to construct a high finesse cavity, which is required to achieve Purcell enhancement of the samples.

While working on the first cavity assembly, I gained valuable insights into how the assembly components and the electronics contribute to the cavity stability. The next step was to leverage this understanding to design and construct a new high-stability cavity assembly, employing simulation tools to assess its performance at low temperatures, with an emphasis on achieving mechanical stability of under 10 pm rms. During the final phase of my PhD, I focused on assembling and evaluating the mechanical performance of the new setup at room temperature and cryogenics using various stabilization protocols. We employed higher-order spatial cavity modes to achieve effective cavity length stabilization while reducing the leakage of error photons from the stabilization beam into the fluorescence detection setup. The technique of scanning cavity microscopy utilized the scattering losses from nanoparticles that were spin-coated onto the cavity mirror to determine the appropriate nanoparticle for measurement purposes. This configuration is then applied to conduct spectroscopic measurements on the identified rare-earth nanoparticles. We anticipate that these findings will be crucial for quantum technology implementations involving various emitter-cavity setups, and that the approach will be a valuable tool in meeting the extremely challenging demands.

1.4 Outline of this thesis

The thesis chapters are outlined as follows:

- **Chapter 2** presents the relevant background of the spectroscopic properties of rare-earth ions and their potential for quantum computing. The discussion includes the cryostats utilized for experiments, along with the laser employed for sample probing and cavity stabilization.
- **Chapter 3** presents the fundamental concept of quantum systems. The quantum master equation is used to discuss cavity-enhanced light matter interactions in various coupling regimes. The Purcell effect and cavity output signals, such as the fluorescence signal, are discussed.
- **Chapter 4** discusses optical properties of the fiber-based microcavity. Microcavity characteristics (such as cavity modes, Gouy phase, and stability conditions) are studied as well as mirror coating modelling. The modelling of transverse mode excitation, coupling efficiency, and diffraction loss caused by the fiber mirror's limited aperture are explored.
- **Chapter 5** presents the mechanical properties of the new microcavity assembly design. This chapter elaborates in detail about the design considerations, mechanical and electronic components. In addition to simulating the assembly mechanical performance at low temperatures.

- **Chapter 6** outlines the experimental work conducted on the newly developed cavity setup. It covers the construction of the cavity, the optical setup, and the doubly resonant technique employed for measuring the cavity parameters. Additionally, it presents the various stabilization protocols implemented to examine the stability of the new microcavity design. The analysis of the electronic closed-loop circuit, as well as the stability of the cavity at both room temperature and cryogenic conditions, is also presented. Furthermore, the error photons leaking from the locking beam into the single-mode fiber and subsequently to the fluorescence detector is addressed.

- **Chapter 7** presents measurements performed on Nd^{3+}- doped Y_2O_3 nanocrystals. It presents the spectroscopic measurements and the potential of using Nd^{+3} ions to read out a qubit is discussed. It discussed how the scanning cavity microscopy can be used to locate the Nd^{3+}-doped Y_2O_3 nanocrystals spin coated on the cavity mirror. It also presents the room temperature and cold measurements performed using the microcavity with Nd^{3+}- doped Y_2O_3 nanocrystals. The discussion includes the Purcell enhancement and the number of excited ions estimations. Furthermore, the necessary conditions for achieving single ion detection levels using the new microcavity.

- **Chapter 8** presents the outcomes related to the requirements for rare-earth quantum computers. To further advance this field, I identify potential enhancements that could contribute to achieving even greater results.

2 Rare-Earth Ions and their Experimental Setup

This chapter covers the properties of rare-earth-ion-doped crystals used in the experiments presented in this thesis. This chapter outlines the readout scheme employed for qubit state measurement, utilizing various materials integrated within the cavity. It also discusses the cryostats employed as cooling systems for the rare-earth samples, enhancing their coherence properties. Furthermore, the chapter covers the stabilized laser sources that are essential for the experiments, facilitating precise excitation of the rare-earth ions and enabling accurate measurements. By integrating these elements, the chapter aims to provide a comprehensive understanding of the experiments based rare-earth ions and the significance of each component in attaining the necessary coherence properties for quantum information applications.

2.1 Rare-earth ion properties

This section explores the origins of rare-earth crystals' unique properties for quantum applications. We will first examine the electronic configurations of rare-earth ions and their impact on coherence properties. Next, we will analyze energy levels and how the host crystal affects the wave function of rare-earth ions, enabling weakly allowed transitions for detection. The origins of homogeneous and inhomogeneous linewidths in rare-earth ions are discussed. It highlights the potential of RE ions in nanocrystals as a promising candidate for quantum computing.

2.1.1 Electronic configuration

The rare-earth (RE) elements are a group of seventeen metallic elements. These contain all fifteen lanthanides on the periodic table, as well as scandium and yttrium. When lanthanides are doped into solid crystals, they reside in either a double (RE^{2+}) or a trivalent (RE^{3+}) state with an electronic configuration of [Xe] $4f^{N}$. Where the occupied electrons, N, range from 1 to 14 for the different lanthanides, the f-orbital corresponds to the angular momentum quantum number of l=3, and the principal quantum number is 4. The $4f^N$ electron shell is closer to the nucleus than the outer filled 5s and 5p shells, which shields the $4f^N$ electron shell from external electronic disturbances. The observed long coherence times of these transitions can be attributed to this shielding effect. Lanthanides share considerable similarities in their chemical, physical, and electromagnetic properties. However, their primary distinguishing attributes lie in their magnetic and optical properties, which enable their utilization in diverse applications, including quantum technology [28-31], biomedical imaging [32-37], and laser stabilization [38-43].

2.1.2 Energy level structure

This thesis involves mostly praseodymium (Pr^{3+}) and neodymium (Nd^{3+}) co-doped into Yttrium oxide Y_2O_3 crystals. For RE^{3+} ions, as used in this work, two electrons are removed from 6s and one electron from the 4f shell while the 5s and 5p shells are remaining filled to act as shields. The electronic transitions within the 4f shell are not allowed due to parity conservation [44]. However, the non-centrosymmetric character of the doped crystals disturbs the wave function of the RE ions, resulting in weakly allowed $4f$- $4f$- energy transitions. The level configuration of the Nd and Pr-doped $LaCl_3$ crystal, as depicted in Fig. 2.1 (a), is also relevant to the rare-earth ions in Y_2O_3 crystals in our context. It is important to note that the crystal field splitting of ions within crystals is typically smaller than the intrinsic level structure of free ions, resulting in a resemblance across various host materials [45]. The energy levels of rare-earth ions in crystals are influenced by the free ion, crystal field, and applied magnetic field [45], with the free ion component mostly including Coulomb interactions and spin-orbit coupling. The energy levels have been defined as $^{2S+1}L_J$, where S, L, and J are spin, orbital angular momentum, and total angular momentum quantum numbers, respectively. Each level manifold exhibits a $2J + 1$ degeneracy.

RE ions with an odd number of electrons in the unfilled $4f$ shell, such as Er^{3+}, Yb^{3+}, and Nd^{3+}, are called Kramers' ions. Non-Kramer's ions have an even number of electrons in the unfilled $4f$ shell, and includes Eu^{3+}, Pr^{3+}, and Tm^{3+}. The energy levels of Kramer (Nd^{3+}) and non-Kramer (Pr^{3+}) ions comes from hyperfine interaction, i.e., interaction with the spin of the nucleus resulting in a variety of low-lying spin levels that can be used as qubit states as well as excited electronic levels that can couple to optical photons as shown in Fig. 2.1 (b) and (c).

The splitting of hyperfine levels ranges from MHz to a few GHz, depending on the ions and the host material. The hyperfine splitting levels of the ground state can exhibit long lifetimes at cryogenic temperatures, making them a suitable option for qubit states.

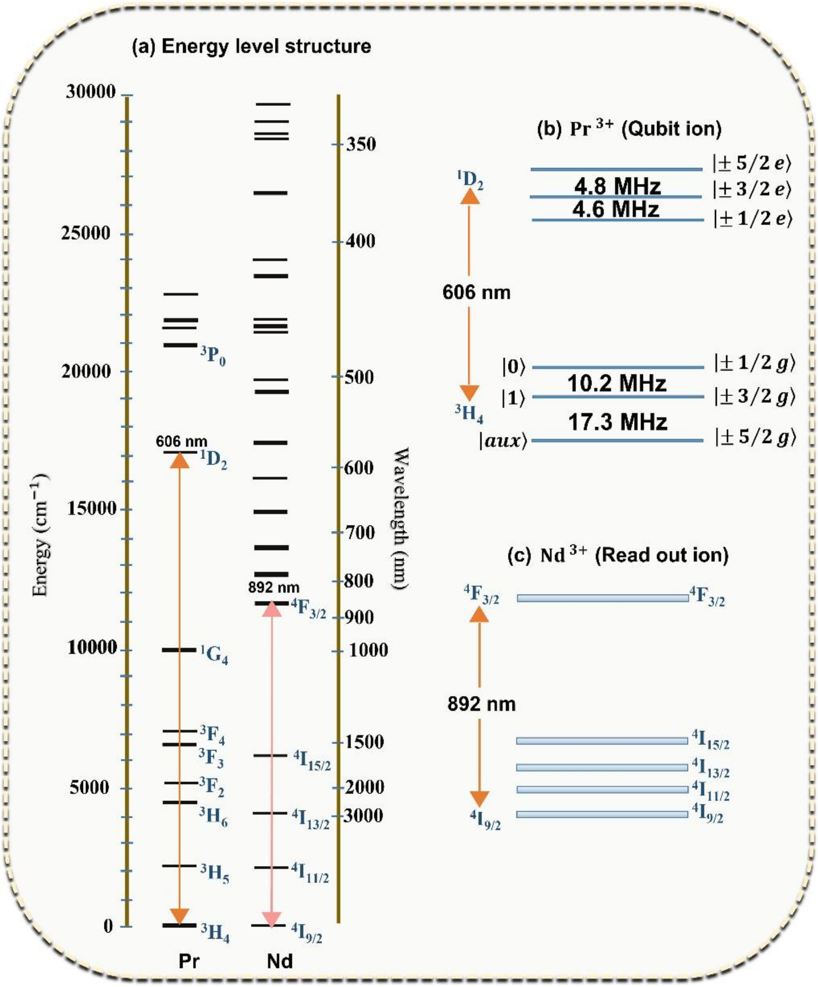

Figure 2.1: (a) Energy level diagram of trivalent Pr^{3+}, and Nd^{3+} ions in $LaCl_3$ with dominant optical transitions observed in Y_2O_3. The figure is reproduced from [47]. (b) illustration of the Pr^{3+} doped Y_2O_3 hyperfine structure of the first optically excited state and the ground, which is used as qubit. (c) Relevant energy level structure of Nd^{3+} in a crystal with the lowest optical transition at 892 nm, which used as a readout ion. It is reproduced from [15].

For Pr^{3+} doped Y_2O_3 crystals, the hyperfine levels |± 1/2 g⟩ and | ± 3/2 g⟩ are considered as qubit states for quantum computing. The qubit state can be manipulated by optical transitions at 606 nm targeting $^3H - ^1D$ hyperfine levels (see Fig. 2.1b). When RE ions are cooled down below 4 K, two of the hyperfine ground levels can be used as qubits, e.g., |0⟩ and |1⟩. These qubit states can be accessed using optical transitions to an excited state, which allows for precise control.

By repeatedly sending optical pulses, an empty spectral window of ions can be prepared. The qubit can be initialized into the desired ground state, such as |0⟩ state, by burning back the ions into the spectral region, thus separating the qubits from the non-qubit ion. State-selective optical transitions associated with hyperfine (qubit) states enable rapid, all-optical single-qubit gate operations [9], which are essential for the development of efficient quantum computing systems. The presence of non-qubit ions can lead to crosstalk with the qubit ion, potentially affecting the bandwidth of gate operations by necessitating an extension of gate duration to mitigate this issue, ultimately leading to a slowdown in the overall process.

For the readout ion, the transition of interest in this thesis project concerning Nd^{3+} is $^4I_{9/4} - {}^4F_{3/2}$ (illustrated in Fig. 2.1c). This transition is notable for its high oscillator strength [15, 46] and high branching ratio to the ground state, indicating an enhanced collection efficiency of the fluorescence at this wavelength. This feature is a primary motivation for exploring this transition for possible applications in single-ion readout, with further details provided in Section 7.1. Given that Nd^{3+} is a Kramers' ion, the crystal field induces a splitting of the $^4I_{9/2}$ state into five Kramers' doublets, while the $^4F_{3/2}$ state is divided into two Kramers' doublets. In the presence of a magnetic field, each doublet can be split into two singlets. Section 7.2 has a detailed discussion of this.

2.1.3 Homogenous and inhomogeneous linewidth

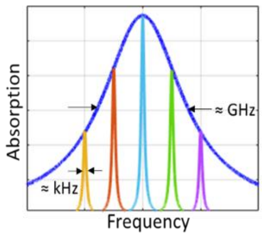

Figure 2.2: illustration of homogenous (colored narrow lines) and in-homogeneous (dark blue)

The homogeneous linewidth serves as a crucial measure of the coherence properties of rare-earth ions, playing an essential role in identifying the most appropriate candidate materials for quantum computing. A narrower homogeneous linewidth signifies a longer coherence time, enabling a qubit to maintain its quantum state for a more extended duration which is required for high fidelity gate operation before experiencing decoherence from environmental influences. The homogenous linewidth of an individual isolated rare-earth (RE) ion is inversely proportional to the lifetime of the optical excited state T_1, represented by,

$$\Gamma_0 = 1/2\pi T_1. \tag{2.1}$$

In crystals doped with RE ions different broadening mechanisms can restrict the homogeneous linewidth of the transition, resulting in a broader profile (see colored narrow lines in Fig. 2.2). Thermal broadening is one of the processes that can lead to an increase in linewidth, resulting from the interaction between crystal lattice phonons and the transition. This contribution to the homogeneous linewidth can be reduced by cooling the crystal below 4 K, utilizing the cryostat described in the following section. The homogeneous linewidth is also influenced by the dynamic processes taking place in the immediate surroundings of the rare-earth (RE) ion. For example, fluctuations in the nuclear spin and electronic spin of the host material can induce broadening. These effects can be reduced by choosing host crystals that have low magnetic moments, such as Y_2SiO_5 or Y_2O_3 and providing a sufficient magnetic field can help to freeze out electronic spin. Another factor that could affect the homogeneous linewidth is the change in the electric field around an ion when nearby ions are optically excited from their ground state. This effect led to a shift in the energy levels, with the magnitude of the change being inversely related to the cube of the distance between the ions. This effect can be mitigated by lowering the doping concentrations or using low intensities for optical excitations [15] to mitigate the power broadening effect.

As a consequence of the above broadening mechanisms, the homogeneous linewidth of a transition is not only limited by the lifetime of the excited state but also by the dephasing time ($T_2^\star$). The homogeneous linewidth, Γ_h, is associated to the coherence time, T_2, through a time-frequency Fourier transform:

$$\Gamma_h = \frac{1}{\pi T_2}, \tag{2.2}$$

The coherence time T_2 describes the total dephasing time due to finite excited state lifetime and the dephasing processes and can be written as:

$$\Gamma_h = \frac{1}{\pi T_2} = \frac{1}{2\pi T_1} + \frac{1}{\pi T_2^\star} \tag{2.3}$$

As previously mentioned, the mechanisms contributing to broadening may be somewhat diminished. This leads to an extended coherence time crucial for high-fidelity gate operation needed for quantum computing and for applications in laser stabilization and biomedical imaging [28-43]. In the doped crystal, there are many ions with – to some extent – overlapping frequency response. These ions can be used as an individual qubit, referred to as an ensemble qubit with the narrowness ultimately limited by the homogeneous width, which is about 7 kHz for Pr^{3+} [45] and sub-kHz for Eu^{3+} features among the narrowest optical linewidths [48].

RE ions have also an inhomogeneous linewidth (dark blue line shown in Fig. 2.2) due to the spatially dependent "DC Stark shift" and imperfections in the crystal, e.g., caused by the dopant ions, which differ in size from the ions in the host crystal. The physical environment experienced by the ions will differ due to this variability of the crystal fields, leading to distinct center frequencies for each overlapping ensemble of ions. This results in an inhomogeneous broadening of the absorption spectra of the crystal, which covers a broad range between 10-100 GHz.

2.1.4 Key features of RE-ions for quantum computing

Recent research highlights the primary benefits of rare-earth ions (REIs) in quantum computing applications (Ref. [9]). Notably, the optical coherence time is several ms, while the spin coherence time can be up to six hours under the influence of magnetic fields when cooled down to ~ 4 K. Qubits are differentiated by having different transition frequencies. To avoid crosstalk, each qubit must occupy its own frequency channel. A controllably broad inhomogeneous line and the tuning range of the laser used to control the qubits set the maximum number of qubit channels to ~ 10^2-10^3. The small spacing between the ions inside the crystal allows for strong coupling via, e.g., the dipole blockade mechanism [10]. This interaction can be utilized to carry out logical gate operations between different qubits [9]. This is also the mechanism that is used to identify the ions that can be used as qubits in the quantum processor (see Chapter 8). Transitions are available at the telecom wavelengths, e.g., erbium at 1.50 µm. Additionally, ensemble-based qubits consisting of ~ 10^9 ions may be used to increase interaction with single photons for quantum memory applications.

2.1.5 Readout scheme

Rare-earth ions-based quantum computing requires reading out the final state of a single qubit ion for quantum computing scalability [9]. Direct readout approaches use microcavity implementation due to the Purcell enhancement effect, which shortens lifetimes and enhances fluorescence rate. This approach could help enhance their weak emission rate.

Additionally, a significant challenge with REIs is that the same physical ion cannot serve both as a qubit and for readout purposes, as state-selective readout cannot be achieved through a cycling transition. This because when a qubit hyperfine state gets excited and falls back to the ground states, which are used as qubit states, it can decay into any qubit level, destroying state information.

This study presents a novel approach to overcome this problem by employing different physical ions. It utilizes readout ions that align with a high finesse cavity to enhance its spontaneous emission via the Purcell effect and to use its fluorescence to identify the qubit state that are outside the cavity resonance (see Section 6.1.2).

The scheme used for qubit state readout is shown in Fig. 2.3 and it can be summarized as follows: Two laser pulses with frequencies $\nu_1$and ν_2 are applied, resonant with the qubit state $|0\rangle \rightarrow |e\rangle$ and the readout ion coupled to a high finesse cavity, respectively. When the qubit is in state $|1\rangle$, as shown in Fig. 2.3a, the laser pulse does not excite the qubit ions, allowing the readout ion to continue emitting (ON). Conversely, if the qubit ion is in the state $|1\rangle$, as shown in Fig. 2.3b, the pulse excites it to the state $|0\rangle \rightarrow |e\rangle$. This transition results in a change in the permanent electric dipole moment, causing a shift in the transition of the neighboring readout

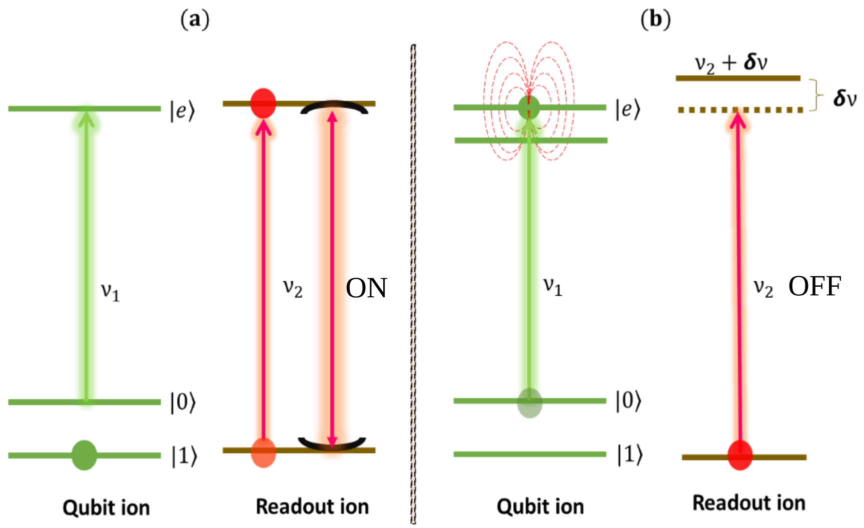

Figure 2.3: The readout ion functions as a sensor, detecting the states of nearby qubit ions through dipole-dipole interaction. The emitted fluorescence signal from the readout ion is coupled to high finesse cavity for Purcell enhancement, either (a) ON when the qubit ion state is |1⟩ or (b) OFF when the qubit ion state is |0⟩. This allows identification of the corresponding qubit ion's state (See the text for more details). Note that the dipole blockade scheme shown here is also used for the two-qubit gates discussed in Chapter. 8.

ion by $\delta\nu$, which depends of $\Delta\mu_{eg} = \mu_e - \mu_g$ and on the separation between the ions. As a result, the readout driving field becomes non-resonant with the detuned transition of the readout ion, leading to the absence of a fluorescence signal (OFF), which indicates that the qubit is in the state $|0\rangle$. This allows for state-sensitive detection by differentiating the photon counts based on whether the readout ion emits or does not emit (only background).

2.1.6 Potential materials for cavity integration

Numerous RE materials can be synthesized, including thin films, e.g., grown or polished down from bulk materials, and nanoparticles. One advantage of using the open access microcavity is its capacity to accommodate various materials at the required microscales. A key motivation for selecting nanoparticles for my thesis project was their availability at the onset of my PhD. Nanoparticles doped with rare -earth ions are significantly simpler to produce compared to thin films, for instance. Additionally, these nanoparticles can be precisely positioned in microcavities in a controlled manner, allowing for selective addressing of individual ions via spectral addressing [49, 50]. Moreover, confining rare-earth (RE) ions in nanoscale solid-state materials allows for high qubit densities with nanometer spacing, correspondingly strong qubit-qubit interactions [10]. One challenge associated with nanoparticles is their susceptibility to considerable extra dephasing processes ($T_{2, NP}$ $/T_{2, bulk} \approx 10^{-3}$). For future scalable production, a well-polished bulk YSO crystal could meet the requirements for good optical T_2 and readout [9].

2.2 Cryostats

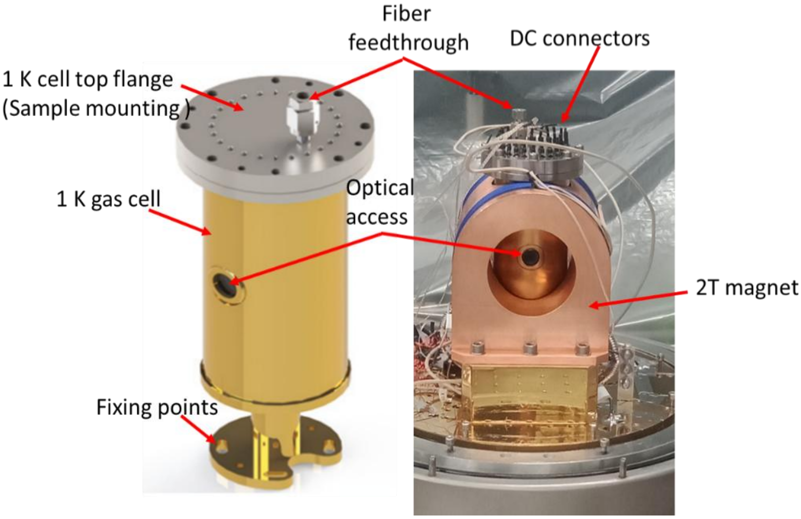

Figure 2.4: The left image displays the inner gas cell after it has been taken out of the cryostat. The upper flange serves as the connection point for various experimental setups. On the right, there is a photo of the MyCryoFirm with the inner gas cell installed along with the main parts of the cryostat.

Cryostats are essential for maintaining low temperatures, which significantly enhance the coherence properties of the rare-earth-ion-doped crystals. To attain optimal coherence properties, the RE ions need to be cooled to temperatures below 4 K. This thesis employs two cryostats, the Oxford Spectromag (SM400) and MyCryoFirm. The Oxford Spectromag, equipped with a 20-liter internal liquid helium reservoir, regulates temperature by modulating liquid helium flow rate, pressure, and vacuum pump operation. It allows optical measurements across a temperature range of 1.5 to 300 K and accommodates magnetic fields of up to 7 Tesla. However, operating the microcavity setup within this cryostat proved challenging due to its limited sample space of 25 mm in diameter, complicating the construction and operation of a stable, high-finesse cavity capable of three-dimensional scanning. The MyCryoFirm cryostat presents a significant advancement in cryogenic technology, offering extended operational durations of several weeks at a reduced cost compared to traditional bath cryostats. Unlike conventional closed-cycle cryostats that rely on conductive cooling, MyCryoFirm employs direct cooling of the sample through an exchange gas. This innovative device is capable of achieving a temperature of less than 2 K, accompanied by a cooling power of no less than 10 mW. It features a sample space designed for a 1 K gas cell (see Fig. 2.4), characterized by a diameter of 48 mm, which aligns well with the new assembly cavity design proposed in this thesis. Additionally, the design of the sample chamber facilitates accessibility for optical fibers and incorporates optical windows to support transmission experiments, while also providing DC and RF electrical connections to the sample. The primary difficulty associated with this type of cryostat lies in the mechanical vibrations, which measure approximately 10 nm rms on the cold plate. The development of a robust microcavity assembly is essential, one that exhibits considerable strength to suppress these vibrations, as discussed in Paper I.

2.3 Light sources

The primary light source utilized in this experiment was a continuous wave titanium-sapphire laser,[1] at a wavelength of 892 nm corresponding to the atomic transition line ($^4I_{9/4} - {}^4F^{3/2}$ transition of Nd^{3+}). The laser was frequency stabilized through the Pound-Drever-Hall technique to a reference cavity[2] that is both vibration isolated and temperature controlled. This stabilized laser source was directed through a double-pass acousto-optic modulator (AOM) configuration, with optical pulses being produced by an arbitrary waveform generator[3] (AWG). The output from the double-pass AOM was then coupled into a polarization-maintaining fiber, which facilitated the routing of the light to the experimental setup.

In this thesis project, an additional light source employed is a single-mode pigtailed distributed feedback (DFB) diode laser manufactured by Nanoplus in Germany, which operates at approximately 935 nm and delivers an output power of around 4 mW. This light source is used for actively stabilizing the cavity length throughout the experimental procedures. This diode laser employs a Peltier element for temperature stabilization, allowing for both temperature and current adjustments. This dual tuning capability ensures that the lock beam and the probe beam, operating at a wavelength of 892 nm, can concurrently align with their respective cavity resonances. Variations in temperature and current drift from the controllers result in a frequency drift that ranges from 21 MHz to 56 MHz over a 24-hour period, a range

[1] M-squared SolsTiS pumped with a Lighthouse Photonics Sprout system at 15 W.
[2] Menlo Systems GmbH, ORS-Cavity.
3 Agilent N8241A.

deemed adequate for maintaining the stability of the lock beam during the measurements.

3 Fundamental Concepts of Light-Matter Interactions

This thesis focuses on optimizing optical microcavities to improve the interaction between light and the weak transitions of rare-earth ions, thereby enhancing their efficacy for quantum information applications. This chapter establishes a theoretical framework for understanding light-matter interactions in optical cavities and the dynamics of quantum systems. This enables the investigation of various coupling regimes between atoms and the optical cavity. Furthermore, this chapter provides insights into the Purcell effect, outlining its fundamental principles and analyzing the various factors that affect the Purcell effect. The fluorescence signal generated by a single atom coupled to a cavity is analyzed, with a focus on the impact of power broadening on the excitation of off-resonant ions, which poses challenges to reaching the single ion level. This theoretical framework was important for modelling the operation of the cavity, and in turn essential for a successful design of a stable setup as will be discussed further in the coming chapters.

3.1 Closed quantum system

This section introduces the theoretical description of the dipole interaction between a single two level (TL) atom with a resonant transition frequency ω_a and an electric field sustained by the optical cavity as shown in Fig. 3.1. The theoretical concept is based on a Hamiltonian $\hat{H}$, which describes the total energy of the system provided by the Jaynes-Cummings Hamiltonian $\hat{H}_{JC}$ [51]. Under the rotating-wave approximation, the complete Hamiltonian $\hat{H}$ for the TL system coupled to an optical mode takes the form:

$$\hat{H}_{JC} = \hat{H}_c + \hat{H}_a + \hat{H}_i, \tag{3.1}$$

Where the first two terms correspond to the energies of the TL system $\hat{H}_a$ and the optical field $\hat{H}_c$. The energy stored in the interaction between the first two terms is given by the last term $\hat{H}_i$. The optical field Hamiltonian $\hat{H}_c$ can be derived by

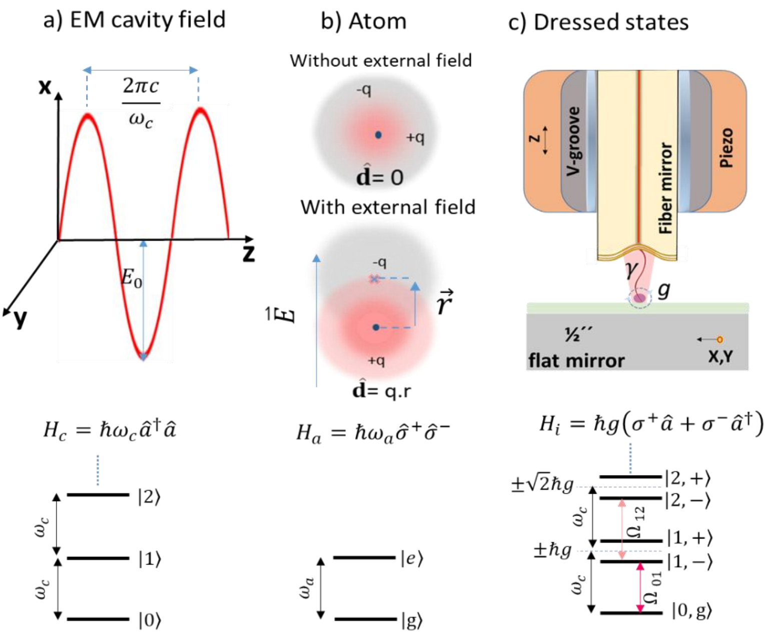

Figure 3.1: The interaction of a two-level atom with a single quantized mode of an optical cavity's electromagnetic (EM) field tuned to the cavity resonance ω_c. (a) EM wavevector is pointing along z while the electric field is polarized along the x axis. The EM field has a harmonic energy ladder where the steps count the number of excitations. (b) An atom is described as a two-level system with ground and excited states |g⟩ and |e⟩ with a transition frequency of ω_a. In an external electric field, the centroids of the negatively charged electron shell and the positively charged nucleus no longer coincide; an electrical dipole is induced. (c) The atom is coupled to the field and localized to an antinode, described by the anharmonic Jaynes-Cummings ladder. In resonance with one of the weak excitation fields, the system operates like a two-level system (red) as long as the transition to the next dressed states is not overdriven (light red).

quantizing the electromagnetic (EM) field in a one-dimensional cavity given by the wave equation solution:

$$\hat{H}_c = \hbar\omega_c(\hat{a}^\dagger\hat{a} + \tfrac{1}{2}) \approx \hbar\omega_c\hat{a}^\dagger\hat{a}, \tag{3.2}$$

We can justify ignoring the energy of the vacuum term $\hbar\omega_c/2$ in Eq. (3.2) if the assumption can be made that there are many field quanta in the cavity mode. This approximation is applied in the following derivations. The operators $\hat{a}^\dagger$and $\hat{a}$

represent the field amplitudes in the cavity mode, which are the creation and annihilation operators for photons, respectively.

Figure 3.1a shows different eigenstates corresponding to the states of different photon numbers where each photon contributes to the field by $\hbar\omega_c$ resulting in an equidistant energy ladder of the quantum harmonic oscillator. The TL single atom, as depicted in Fig. 3.1b, consists of ground state $|g\rangle$ and excited state $|e\rangle$ split by energy $\hbar\omega_a$. The atomic transition is described by the creation $\hat{\sigma}^+ = |e\rangle\langle g|$ and annihilation $\hat{\sigma}^- = |g\rangle\langle e|$ operators. The excited state population of the TL system is determined by $\hat{\sigma}^+\hat{\sigma}^- = |e\rangle\langle e|$ in units of $\hbar\omega_a$. The Hamiltonian that describes that state can be expressed as,

$$\hat{H}_a = \hbar\omega_a\, \hat{\sigma}^+\hat{\sigma}^-. \tag{3.3}$$

For a free atom, as discussed above, the transition between the states $|g\rangle \leftrightarrow |e\rangle$ using $\hat{\sigma}^+$and $\hat{\sigma}^-$operators induce an atomic dipole moment operator $\hat{\mathbf{d}}$ in the TL system. That means $\hat{\mathbf{d}}$ can be expressed as,

$$\hat{\mathbf{d}} = \mathbf{d}\,(\hat{\sigma}^+ + \hat{\sigma}^-). \tag{3.4}$$

where $\mathbf{d}$ represents the transition dipole moment. When the TL system is placed in the optical cavity, the TL system dipole moment in Eq. (3.4) interacts with the electric field of the cavity mode. This interaction can be described by the remaining Hamiltonian $\hat{H}_i$ in Eq. 3.1 and can be given as,

$$\hat{H}_i = -\hat{\boldsymbol{d}}\cdot \hat{E}_x(t). \tag{3.5}$$

Where $\hat{\mathrm{E}}_{\mathrm{x}}$ represent the electric field operator of the quantized field along the cavity z axis and polarized in the x direction as shown in Figs. 3.1a and 3.1b. The $\hat{\mathrm{E}}_{\mathrm{x}}$ field operator can be described using the $\hat{a}^\dagger$and $\hat{a}$ operators mentioned in Eq. (3.2),

$$\hat{\mathrm{E}}_{\mathrm{x}}(t) = \sqrt{\frac{\hbar\omega_c}{2\epsilon_0 V}}\,\epsilon_x\,(\hat{a}^\dagger e^{-i\omega_c t} + \hat{a}e^{i\omega_c t}). \tag{3.6}$$

where V is the cavity mode volume, ϵ_0 is the dielectric constant for free space. ϵ_x is the field polarization unit vector.

Various considerations must be considered to proceed with the interaction Hamiltonian derivation given in Eq. (3.5). As in the TL system, a single atom is located at the antinode of the quantized optical mode field, so the atom experiences spatially constant field amplitudes. The dipole $\mathbf{d}$ of the free single atom is considered to be polarized in the x direction as the electric field. Using those considerations together with Eqs. (3.4) and (3.6), the interaction Hamiltonian in Eq. (3.5) can be rewritten as,

$$\hat{H}_i = \sqrt{\frac{\hbar\omega_c}{2\epsilon_0 V}}\mathbf{d}(\hat{\sigma}^+ + \hat{\sigma}^-)(\hat{a}^\dagger e^{-i\omega_c t} + \hat{a}e^{i\omega_c t}). \quad (3.7)$$

This interaction can be simplified using the rotating-wave approximation mentioned earlier. The $\hat{a}^\dagger$ and $\hat{a}$ field operators can be represented as time varying field amplitudes with ω_c, and the $\hat{\sigma}^+$and $\hat{\sigma}^-$operators oscillate between the atomic states with the resonance frequency ω_a. The fast oscillation components can be ignored from Eq. (3.7), resulting in [15],

$$\hat{H}_i = \hbar g\big(\hat{\sigma}^+\hat{a} + \hat{\sigma}^-\hat{a}^\dagger\big). \quad (3.8)$$

Where g is the dipole coupling strength, which quantifies the interaction strength. Assuming the dipole is properly aligned with the electric field, the maximum value is given by [18]:

$$g_0 = \sqrt{\frac{\omega_c\,\mathbf{d^2}}{2\,\hbar\,V\epsilon_0}} = \sqrt{\frac{3\lambda_c{}^2 c\,\gamma}{4\pi\,V}}. \quad (3.9)$$

Eq. (3.9) gives the maximum coupling strength, which depends on three parameters, two related to the TL system, the atomic dipole transition strength **d** and the decay rate γ, whereas the third is related to the cavity geometry V. However, the effective coupling strength has one more parameter that depends on the position of the atom with respect to the cavity mode, and this can be given by,

$$g\,(r) = g_0\,\psi(r), \text{where}\,\psi(r) = \left[\frac{\omega_0}{\omega(z)}\right]\,\sin\,(kz)e^{-(x^2+y^2)/\omega_0^2} \quad (3.10)$$

where $\psi(r)$ is the spatial distribution of the Hermit-Gaussian HG_{00} cavity mode standing field. The higher order spatial modes discussed in chapter 4 are not employed for atom excitation; instead, they serve the purpose of stabilizing the cavity length. In contrast, a different wavelength of the HG_{00} probe beam is utilized to excite the rare-earth ions. For a stationary atom located at the maximum field antinode in the cavity ($g = g_0$), the full Jaynes-Cummings Hamiltonian writes,

$$\hat{H}_{JC} = \hbar\omega_c\hat{a}^\dagger\hat{a} + \hbar\omega_a\,\hat{\sigma}^+\hat{\sigma}^- + \hbar\,g\,\big(\hat{\sigma}^+\hat{a} + \hat{\sigma}^-\hat{a}^\dagger\big). \quad (3.11)$$

As shown in Fig. 3.1c, the eigenstates of the Jaynes-Cummings Hamiltonian are arranged in doublets (except for the unchanged ground state, |0, g⟩), which we call the n^{th}-order dressed states, |n, ±⟩, where n = 1, 2... corresponding to the photon number. If the atom is in resonance with the cavity ($\omega_a = \omega_c$), the splitting of the doublets can be given as $2\hbar g\sqrt{n}$=$\hbar\Omega$, where $\Omega = 2g\sqrt{n}$ is called the Rabi frequency.

3.2 Open quantum system: Dissipation process

3.2.1 Quantum Master Equation

Equation (3.11) describes an isolated quantum system. For any practical system, dissipation from coupling to the environment causes the quantum system to decohere into several states, which can model using an open system. There are two sources of dissipation processes in our case: photons leak out from imperfectly reflecting cavity mirrors at a rate of 2κ and the TL system spontaneously emit photons into free space at a rate of 2γ. These dissipation processes can be included in the system by using the quantum master equation [52], which describes the time dependence of the coupled atom–cavity system. To derive the induced dynamics, the coupling system must be driven by an external light source. In our case, the cavity with TL system is driven by a coherent probe field for fluorescence measurements discussed in Section 7.5.2. The probe beam can operate in two modes: continuous-wave (CW), which is used to locate the good nanoparticle for measurements as well as cavity length and finesse measurements, and pulsed mode, which is used to excite the TL system and collect the fluorescence signals. For the CW driving mode, the Hamiltonian takes the form of $\widehat{H}_{d1} = \hbar\varepsilon\left(\hat{a} + \hat{a}^{\dagger}\right)$, which adds a photon rate of ε to the cavity field, and $\widehat{H}_{d2} = \hbar\Omega(\hat{\sigma}^{+} + \hat{\sigma}^{-})$ for the pulse mode where the atom excitation is driven by the Rabi frequency, Ω, of a probe beam.

In the Schrödinger picture, the density matrix $\rho = \sum_i c_i \, |\Psi_i\rangle\langle\Psi_i|$ is used to describe the ensemble of states with c_i giving the probability of the system being in the state $|\Psi_i\rangle$. The time evolution for ρ is given by the master equation formalism [53]:

$$\frac{d}{dt}(\rho) = \frac{-i}{\hbar}[H, \rho] + \mathcal{L}_c\rho + \mathcal{L}_a\rho, \tag{3.12}$$

where $\mathcal{L}_c$ and $\mathcal{L}_a$ represent the Lindblad operators which takes into account the dissipation process: cavity decay losses, and the atom spontaneous emission, respectively. The first term of Eq. (3.12) describes the coherent evolution of the driven system, and includes the density matrix ρ and the Hamiltonian $\widehat{H}$. The Hamiltonian $\widehat{H}$ takes the form,

$$\widehat{H} = \widehat{H}_{JC} + \widehat{\mathrm{H}}_d, \tag{3.13}$$

Where $\widehat{\mathrm{H}}_d$ is the driving Hamiltonian, which is defined by the specific excitation mode used (continuous wave or pulse mode) and $\widehat{H}_{JC}$ presented in Eq. (3.11).

3.2.2 Solving the Master Equation

For a weakly excited atom, the population of the excited state $\langle\hat{\sigma}^{+}\hat{\sigma}^{-}\rangle$ is small, and the transitions shown in Fig. 3c become limited to $|0,\mathrm{g}\rangle$, and $|1,\pm\rangle$. The total state vector Ψ(t) can be written as [53],

$$\Psi(t) = c_{+}(t)|1,+\rangle + c_{-}(t)|1,-\rangle + c_{0}(t)|0,g\rangle, \tag{3.14}$$

where the components $c_{\pm}(t)$ represent the complex amplitudes of the atom and cavity excitations. Eq. (3.12) can be solved analytically and the derivation can be found elsewhere (see, e.g., [53, 54]), we will only state the results. The solution yields the population of the excited state $\langle\hat{\sigma}^{+}\hat{\sigma}^{-}\rangle$ and the average intracavity photon $\langle\hat{a}^{\dagger}\hat{a}\rangle$, which can be rewritten as,

$$\langle\hat{\sigma}^{+}\hat{\sigma}^{-}\rangle = \left|\frac{igE}{\tilde{\gamma}\,\tilde{\kappa}+g^{2}}\right|^{2}, \langle\hat{a}^{\dagger}\hat{a}\rangle = \left|\frac{E\,\tilde{\gamma}}{\tilde{\gamma}\,\tilde{\kappa}+g^{2}}\right|^{2} \tag{3.15}$$

where E represents the pump amplitude for the atom excitation, $\tilde{\gamma} = (\gamma + i\Delta_{pa})$, and $\tilde{\kappa} = (\kappa + i\Delta_{pc})$. $\Delta_{pa} = (\omega_{p} - \omega_{a})$ and $\Delta_{pc} = (\omega_{p} - \omega_{c})$ are the pump-atom detuning and the pump-cavity detuning, respectively. The cavity field can be expressed more clearly as,

$$\langle\hat{a}^{\dagger}\hat{a}\rangle = \frac{E^{2}/\kappa^{2}}{1+\left(\Delta_{pc}/\kappa\right)^{2}}\,\frac{1}{|1+2\tilde{C}|^{2}}, \text{ where } \tilde{C} = \frac{g^{2}}{2\tilde{\kappa}\tilde{\gamma}} \tag{3.16}$$

We have now separated the expression into two factors: The first term represents the intracavity field of the bare cavity given in the Lorentzian curve while the second stands for the dressing induced by the atom. We have introduced a convenient term called the atom complex cooperativity $\tilde{C}$, which on resonance can be given as $C = g^{2}/(2\kappa\gamma)$ [18]. This expression represents the cavity figure of merit that compares the rates of lossy processes, κ and γ, with the energy exchange between the field and the atom, g.

3.2.3 Coupling regimes

Different coupling regimes can be established depending on the comparative values of the atom-cavity coupling strength g, the decay rate of the electric field in the cavity κ, and the spontaneous emission rate of the atom in free space, γ. In the limit $g \to 0$, one retrieves the bare cavity Lorentzian profile (see Fig. 3.2, black dashed curve), which is the standard profile of the Fabry-Pérot resonator with a linewidth κ.

Strong coupling regime: In this regime the coupling ($g \gg \kappa, \gamma$), therefore it is high enough for the atom and the cavity field to exchange the energy several times before

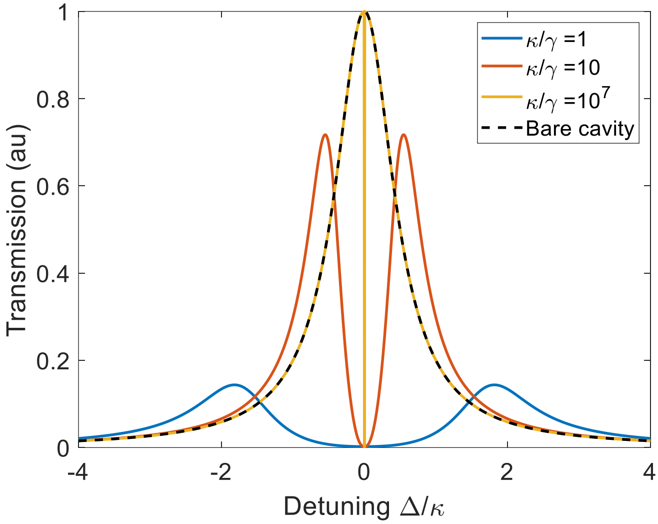

Figure 3.2: Transmission through the cavity for a resonant atom-cavity system vs. detuning $\Delta = \Delta_{pa} = \Delta_{pc}$ in units of cavity decay rates κ. The cavity transmission is given for different cavity to atom linewidth ratios (solid lines). The solid lines represent a cavity with one atom and the system is in the strong (blue with $g = 5$ κ , and dark orange with $g = 1.5$ κ) and fast (bright orange with $g = 6 \times 10^{-4}$ κ) coupling regimes. The parameters of our cavity are (g, κ, γ) = 2π × (10 MHz, 17 GHz, 0.32 kHz) gives a cooperativity of C=10. This is consistent with the fast-coupling regime bright orange plot. The dashed line represents an empty cavity ($g = 0$) which shows one peak centered on resonance $\Delta = 0$. The transmission ($T = \kappa \langle \hat{a}^{\dagger} \hat{a} \rangle$) are normalized to the bare cavity transmission.

leaking out of the cavity and, therefore, oscillates between the electronic and optical system (vacuum Rabi oscillations). This regime is represented in Fig. 3.2 as a dark orange and blue line at different coupling strengths, $g = 1.5\kappa$ and $g = 5\kappa$, respectively. As we detune the cavity from resonance, it exhibits two peaks with equal amplitude.

This single-photon Rabi splitting or normal-mode splitting can be understood as follows (Fig. 3.2): In a resonant atom-cavity system the atomic absorption degrades cavity finesse (defines the total loss in cavity), resulting in low intracavity and transmitted power. As the laser is detuned away from resonance, atomic absorption decreases and transmission increases until the cavity loss caused by atomic absorption no longer limits constructive interference from numerous round trips.

Further detuning reduces intracavity power and constructive interference within the cavity. This yields two symmetric transmission peaks at $\Delta = 0$.

Fast coupling regime: The fast-coupling regime can be achieved when the cavity decay rate $\kappa \gg g, \gamma$. In this scenario, because the cavity decay rate exceeds the atom-cavity coupling rate g, a photon emitted by an excited atom will exit the cavity before the atom has the opportunity to reabsorb it. This regime relates to our cavity in the context of this thesis, which investigates a mode volume of 5 λ^3 and a finesse of 3000, using Nd^{3+} ion-doped nanoparticles with a branching ratio of 23%. The parameters are specified as $(g, \kappa, \gamma) = 2\pi \times$ (10 MHz, 17 GHz, 0.32 kHz). In this regime, the cavity decay rate κ is significantly greater than both g and γ. As a result, the atomic absorption diminishes the cavity transmission at resonance, resulting in the absence of the Rabi splitting. Rather, there is a dip in a narrow region around the atomic resonance point with a width corresponding to the atomic linewidth γ. This regime is plotted as a bright orange line in Fig. 3.2.

The presence of the cavity in this regime is to modify the optical density of states, thereby increasing spontaneous emission rate, a phenomenon known as the Purcell effect. This effect is utilized to improve the emission rate of Nd^{3+} readout ion-doped nanoparticles, which are integrated into the microcavity, an essential component for quantum computing based single rare-earth ion.

3.3 Enhancement of spontaneous emissions: Purcell Effect

The decay rate of an excited atom, according to Fermi's Golden Rule [55], is proportional to the density of the final states $\rho(\omega)$ and the dipole coupling strength g between the field and the TL atom and given by,

$$\gamma_{|e\rangle \to |g\rangle} = 2\pi\, g^2 \rho(\omega). \tag{3.17}$$

Where g is given by Eq. (3.9). In free space, the density of states $\rho(\omega)$ have a continuum of radiation modes, and the decay rate results from integration over the coupling to all modes. As a result, the atom-field interaction is still weak, and any coherent coupling to the TL system will be lost due to dissipation from all surrounding modes. For a TL system integrated into an optical cavity with finesse $\mathcal{F}$, the density of states of the TL system is just the cavity's structure factor, given by the Lorentzian spectrum feature and can be defined as,

$$\rho(\omega_a) = \frac{1}{\pi} \frac{\kappa/2}{(\kappa/2)^2 + (\omega_c - \omega_a)^2}. \tag{3.18}$$

where κ, ω_c, and ω_a are defined previously, and representing the cavity decay rate, cavity frequency, and atomic resonance frequency, respectively. As given in Eq. (3.18), the existence of the cavity modifies the density of states, resulting in a notably higher decay rate into the cavity mode, which acts as the only resonant loss channel in contrast to free space. On resonance ($\omega_c = \omega_a$), the density of states given by Eq. (3.18) becomes $\rho(\omega_a = \omega_c) = 2/\pi\,\kappa$. Using Eq. (3.17) the decay rate into the cavity mode becomes,

$$\gamma_c = \frac{\gamma_{|e\rangle \to |g\rangle}}{4} = \frac{g^2}{\kappa}. \tag{3.19}$$

Notably, divide by 4 to consider only the emissions occurring within the cavity mode. The total decay rate can be written in terms of the cooperativity which is given by Eq. (3.16),

$$\gamma_{tot} = \gamma + \frac{g^2}{\kappa} = \gamma\,(1 + 2\mathrm{C}) \tag{3.20}$$

The existence of the cavity clearly has the potential to influence the atom's decay rate, which now consists of two terms: one related to the free space decay rate γ and the other part describing the decay rate to the cavity mode g^2/κ.

The ratio of the total decay rate to the free space decay rate γ is the so-called *Purcell enhancement* and can be given as,

$$\frac{\tau_0}{\tau_c} = \frac{\gamma_{tot}}{\gamma} = \left(1 + \zeta F_p\right). \tag{3.21}$$

Where τ_c is the reduced lifetime as compared to free space lifetime τ_0. $F_p = 2C$ is the Purcell factor and is defined as the ratio of the spontaneous emission rate in the cavity γ_c (see Eq. 3.19) to the one in free space γ and ζ defines the branching ratio of the relevant transition. The factor $F_{\text{eff}} = \zeta F_p$ is defined as the effective Purcell factor. The Purcell factor can be expressed in relation to the parameters of the cavity as follows,

$$F_p = \frac{g^2}{\kappa\gamma} = \frac{6}{\pi^3}\left(\frac{\lambda}{n}\right)^2 \frac{\mathcal{F}}{w_0^2}. \tag{3.22}$$

Where n is the refractive index inside the cavity, λ is the wavelength, $\mathcal{F}$ is the cavity finesse and w_0 is the cavity mode waist.

In the context of our cavity parameters discussed in the previous section on the fast-coupling regime, the effective cooperativity is approximately ζC ≈ 9. This results in an effective Purcell effect of $F_{\text{eff}} = \zeta F_p = 2\zeta C$ =18. This value represents the expected improvement in the emission rate of Nd^{3+} within cavity parameters mentioned above.

3.3.1 Consideration of enhancement in our system

Several factors that are not accounted for in the theoretical calculations may impede the achievement of the Purcell enhancement value ($F_{\mathrm{eff}} = 18$). The derivations assume the particle is at an antinode of the standing wave field, maximizing coupling strength, g. However, the effective coupling strength also depends on the atom's position relative to the cavity mode, as described by Eq. (3.10). An additional factor that can influence the Purcell enhancement is the degree of overlap between the emitter linewidth Γ_h and the cavity linewidth κ. The earlier derivations are based on the assumption that the emitter homogeneous linewidth Γ_h is significantly narrower than the cavity linewidth κ, which is referred to as the fast cavity regime. In contrast, in the bad emitter regime where $\Gamma_h \gg \kappa$, such as Nd^{3+} readout ion at room temperature, the effective Purcell factor decreases in accordance with $F_{\mathrm{eff}} \propto \kappa/\Gamma_h$. The ratio of κ/Γ_h for Nd^{3+} ions at the relevant transition ${}^4I_{9/4} - {}^4F_{3/2}$ is about 0.04, indicating minimal Purcell enhancement at room temperature. This aligns with the measurements presented in Section (7.5.2), highlighting the necessity of conducting experiments at cryogenic temperatures, as this condition allows the emitter linewidth to narrow down to just a few kHz. The last factor that greatly influences the Purcell effect of the readout ion is the root mean square jitter in the cavity length [56, 57] due to the mechanical noise coupled to the cavity mode from the noisy surroundings. This presents a primary challenge when dealing with open access cavities. This effect can be reduced by building a highly stable cavity assembly and working on different stabilization techniques to improve the stability of the cavity length during the measurements which is the main topic of this thesis.

3.4 Fluorescence signal and power broadening

In Chapter 7 we will discuss experiments, where an atom inside a cavity will be driven by a probe beam with Rabi frequency Ω. According to the Bloch equations [55], a strong driving field ($\Omega \rightarrow \infty$) tends to equalize the populations (half of the atoms are excited). Equivalently the excited state has a steady state population ρ_{ee} given as [55],

$$\rho_{ee} = \frac{\Omega^2}{(2\Delta_{pa})^2 + 2\Omega^2 + 4\gamma_{tot}{}^2} \tag{3.23}$$

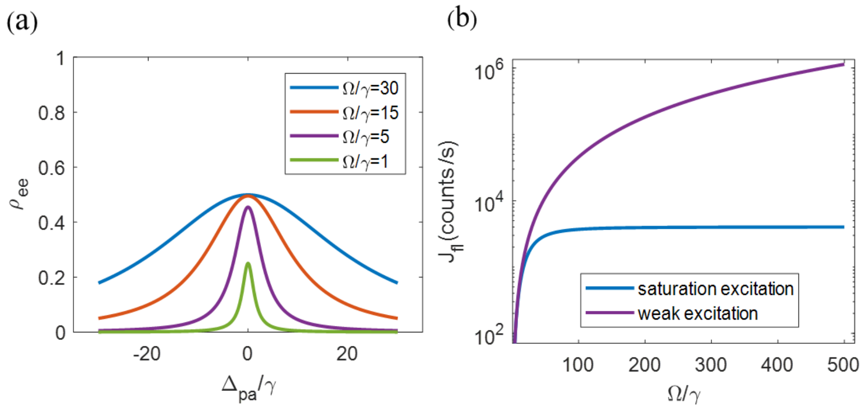

Figure 3.3: (a) The power broadening effect is represented as a modification of the Lorentzian lineshape to different Rabi frequencies that is proportional to the amplitude of the excitation field. This phenomenon shows that the effective linewidth increases as the power of the laser used increases, even if the laser's linewidth remains constant. This is due to the laser intensity approaching the saturation intensity of the transition. (b) shows the on resonance ($\Delta_{pa}= 0$) fluorescence signal as a function of Rabi frequencies to linewidth transition ratios in the saturation and weak excitation scenarios. This obtained for collection efficiency of η=10% and cooperativity of 10.

With full width at half maximum (FWHM) given as [55],

$$\text{FWHM} = \sqrt{\gamma^2 + 2\Omega^2} \tag{3.24}$$

Where γ_{tot} represents the total decay rate given by Eq. (3.20). The cavity fluorescence signal is generated by atoms emitting photons at a rate of 2γ into the cavity mode, which are then enhanced by a Purcell factor of $F_p = 2C$. The TL system fluorescence signal on the resonance can be derived as,

$$J_{fl} = 4\gamma C\eta \left(\frac{s/2}{(1+2C)^2+s+(\Delta_{pa}/\gamma)^2}\right) \tag{3.25}$$

where $s = \Omega^2/2\gamma^2$ represents the saturation parameter and we have introduced the parameter η to account for the total coupling efficiency between intracavity photons to the detector used for fluorescence detection. Equation (3.25) represents the fluorescence signal in steady state where the excited state population saturate at

$\rho_{ee} = 1/2$, (see Fig. 3.3a, blue line). In the limit of weak excitation where $s \ll 1$, and for no detuning between pump and atom, $\Delta_{pa} = 0$, Eq. (6.25) is given as[4],

$$J_{fl} = 4\gamma C\eta \left(\frac{s/2}{(1+2C)^2}\right) = \eta \frac{\kappa}{2}\left(\frac{\Omega}{g}\right)^2 \left(\frac{2C}{1+2C}\right)^2 \tag{3.26}$$

Equation (3.26) presents the fluorescence signal based on the assumption of weak excitation (see Fig. 3.3b, purple line). This equation can be used to represent the resulting fluorescence signal of TL atom driven by coherent excitation [54], which is relevant to our discussion in Chapter 7.

As depicted in Fig. 3.3a, linewidth profile indicates a 'power broadening' that scales with $\sqrt{s} = \Omega/\sqrt{2}\gamma$. This reflects that using a high excitation power for TL system can improve the fluorescence signal (see Fig. 3.3b, purple line); however, it may also lead to power broadening, which can hinder the ability to achieve single-ion level by facilitating off-resonant excitation of adjacent ions. This effect is discussed later in Section 7.6.3 and is used to calculate the total number of excited ions at low temperature.

[4] $\frac{x}{x+M} \cong \frac{x}{M}$ $for\ x \ll 1\ and\ M > 1.$

4 Optical Properties of Fiber-Based Microcavities

The experimental difficulties encountered with two generations of microcavity configurations, which will be elaborated upon in Section 5.1, have led me to conduct a more thorough examination of the operational functions involved. These challenges are primarily based on integrating stability with fluorescence detection, especially when the wavelengths of the stabilization and fluorescence beams are similar. This situation requires the development of innovative techniques that maintain cavity stability while simultaneously allowing for the probing of samples with an alternative beam. In addition to understanding our experiments, this analysis can also allow us to make well supported suggestions for future improvements.

This chapter explores different properties of fiber-based Fabry-Pérot microcavities, higher-order spatial modes, diffraction loss, and coupling efficiency between the cavity mode and the single-mode fiber (SMF)-based mirror.

4.1 Fiber Fabry-Pérot microcavities

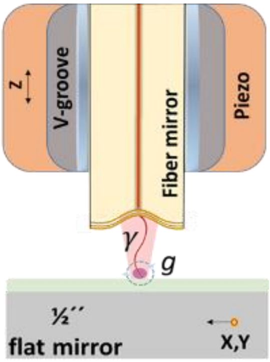

Figure 4.1: Schematic of fiber based Fabry-Pérot microcavity. The cavity is composed of a concave fiber mirror and a flat macroscopic mirror, with nanoparticles exhibiting a decay rate γ positioned between them, coupled to the cavity mode with a coupling strength of g.

Based on earlier discussions, it is obvious that an atom-cavity coupled system has a figure of merit that we want to maximize: single atom cooperativity, C. In terms of the cavity parameters, it can be written as: $\mathrm{C} = g^2/2\kappa\gamma = \left(3{\lambda_c}^2\,\mathcal{F}/\pi^3 w_0^2\right)$, where λ_c is the wavelength, $\mathcal{F}$ is the cavity finesse, w_0 is the cavity mode beam waist. As a result, achieving high cooperativity necessitates small waist and high finesse. A small waist of about 1.4 µm can be accomplished by combining a small radius of curvature, R_c, for the mirrors and a small cavity length, L. Fiber Fabry-Pérot microcavities (FFPCs) succeed at achieving high finesse while maintaining small radii of curvature with very low roughness [18]. Hunger, Reichel, and colleagues [18, 58] made a breakthrough in FFPCs by integrating high-quality mirrors on optical fiber end facets (see Section 6.1). FFPCs are produced by micromachining the tip of an optical fiber with CO_2 laser ablation [18, 59]. This approach produces surfaces with controlled ellipticity [60] and very low roughness, resulting in reduced scattering loss, allowing micro-machined fiber tips to be used with high-finesse mirrors. Curved mirrors with different radius of curvatures 20−65 µm and different finesse 600 and 3000 were designed for our cavity as part of the PhD project of Mohammed Alqedra [15].

As shown in Fig. 4.1, the microcavity in our setup is formed by two high-reflectivity mirrors facing each other: one flat mirror acts as a sample holder, while the second one is a fiber-based mirror for sample probing and fluorescence collecting. These mirrors are typically made up of two highly reflecting Distributed Bragg Reflectors (DBR), which can confine light in a limited mode volume as small as a few wavelengths cubed [61] and hence enhance light-matter interaction. The quality factor of the FFPCs is not a fixed quantity but depends on the separations between the cavity mirrors. The microcavity assembly depicted in Fig. 4.1 is equipped with three nanopositioners indicating as x, y and z, enabling precise control over the fiber mirror and the lateral scanning of the flat mirror that supports the samples. This arrangement allows for dynamic tuning of the resonance frequency, making it possible to target multiple ions at different frequencies and the open geometry allowing flexibility in material selection, an essential aspect of quantum computing as previously discussed in Section (2.1.6). Furthermore, a notable characteristic of the fiber-based microcavity is its integration with optical fibers, which efficiently couples light for detection or further use within a network. The numerous benefits of FFPCs position them as an excellent option for meeting the demands of quantum computers, especially when compared to alternative cavities like focused ion beam milled cavities [19] and nanophotonic cavities [20].

To provide an elementary understanding of the topics employed throughout this thesis, the operating principle and basic characteristics of Fabry-Pérot resonators must first be introduced.

4.2 Microcavity Properties

Consider an open resonator that consists of two mirrors $M_{i=1,2}$, as shown in Fig. 4.2a. The cavity mirrors are separated by a distance L and have a power reflectivity and transmittance given by $R_i = |r_i|^2$ and $T_i = |t_i|^2$, where r_i and t_i are the frequency dependent reflectivity and transmittivity respectively. In such a cavity, light is confined along the cavity axis; as a result, light bounces back and forth according to the cavity parameters of each mirror (such as reflectivity, diameter, and curvature) and other loss channels caused by objects within the cavity. The finite cut-off diameters (D = 2a) of the mirrors may produce diffraction loss to beams with larger transversal size such as higher order transverse modes that are excited within the cavity. This may result in a higher order mode suppression and a reduction in the finesse as detailed below. With a resonator of this kind, three parameters may be used to describe the stable resonance, and they need to be unchanged after one complete round-trip:

(i) The phase introduced to the beam as it propagates,

(ii) The field amplitude along the cavity axis,

(iii) The transverse distribution of the on-axis beam profile.

In the following discussion, we will investigate the origins of the phase and the transverse modes inside the microcavity formed by the curved mirror and the flat mirror. Then, we will demonstrate how to excite the various TEM_{mn} modes inside the microcavity, which are employed to stabilize the microcavity length. We demonstrate how the fiber mirror's finite dimension affects cavity measurements such as finesse and coupling efficiency for the single mode fiber (SMF).

4.2.1 Phase

In this section, we derive the phase shift introduced on the beam as it propagates in a flat-concave cavity with highly reflecting DBRs. Figure 4.2a, shows the schematic of an incoming continuous beam travelling along the cavity z-axis with amplitude E_0 and frequency ω_c as measured at the input mirror of the cavity (M_1). Assuming

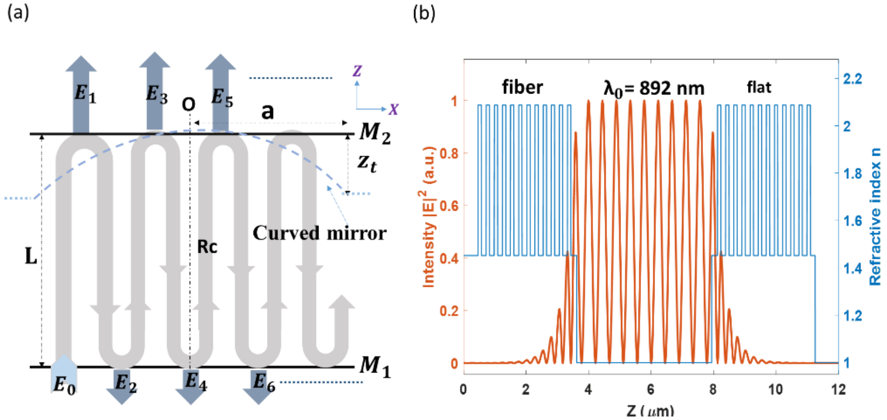

Figure 4.2: (a) Shows a continuous beam entering a cavity at M1. The beam's amplitudes are derived by summing components and considering phase shifts. If M_2 is replaced with a curved mirror, parameters R_c, a, and z_t represents the radius of curvature, the mirror cut-off radius, and the mirror depth, respectively. (b) The simulated distribution of refractive index and electric field intensity is shown, highlighting the field's penetration into the Bragg mirror using the transfer matrix method [62].

two parallel flat mirrors, on the transmission side (M_2), the incident beam makes N=1,3,5… passes corresponding to amplitudes E_1, E_3, E_5, etc. On the reflection side (M_1) the reflection amplitudes are given by E_2, E_4, E_6, etc. The transmitted and reflected beams are obtained by summing the amplitudes of all these beams, taking into account their phase shift. In the case where M_2 is a curved mirror, it is essential to consider new parameters for the mirror, especially R_c, a, and z_t which denote the radius of curvature, the cut−off radius, and the depth of the mirror, respectively.

Figure 4.2b shows the simulated refractive index and the electric field intensity distribution inside the FFPC structure with field penetration into the Bragg mirror. The cavity mirror coatings used in this thesis project are made of about 12 pair of layers of Ta_2O_5/SiO_2 (DBRs) designed for a wavelength of 892 nm, corresponding to the transition of the readout ion Nd^{3+}.

At resonance, the high intensity of $|E|^2$ indicates significant optical confinement along the cavity axis, with an anti-node near to the flat mirror front face, where the attainable RE ions samples are located. The top layer of both DBR mirrors was coated with a SiO_2 layer of about $\lambda/4$ thickness in order to bring the RE ions samples closer to the field maximum and maximize their interaction with the cavity field. Consequently, there is a phase shift of $\varphi_{1,2}$ =+40°. This phase shift is provided by the manufacturer and is also simulated using the transfer matrix method, as explained in Section 6.1. When evaluating the round-trip conditions, it is essential to include the phase shift introduced by the additional layer on both mirrors in the round-trip phase delay as, $2kL + \varphi_1 + \varphi_2$, where k is the wave number and L is the cavity length.

The spatial transverse electromagnetic resonant modes (TEM_{mn}) in cavities with flat-concave mirrors have a flat wavefront at the flat mirror and curvature matching at the concave mirror. During single pass propagation, TEM_{mn} modes, with transversal mode orders m and n, experience a phase lag compared to a plane wave (the case of two flat cavity mirrors) proportional to $(m + n + 1)$ and can be given as,

$$\vartheta_{mn} = (m + n + 1)\ arccos\sqrt{1 - (L + 2L_\varphi)/R_c}\,. \tag{4.1}$$

The *arccos* term represents the Gouy phase, φ_{gouy}. The $2L_\varphi$ represents the phase penetration depth [63] to cavity mirrors and given as, $L_{\varphi_{1,2}} = \varphi_{1,2}/2k \approx 50$ nm. In Figure 4.2b the intensity decay into DBRs represents the frequency penetration depth, which has been calculated to be 1.1 μm for the coatings of our cavity mirrors [63].

To ensure the constructive interference between the transmitted field's amplitudes E_1, E_3, E_5, etc., as depicted in Fig. 4.2a, which leave the cavity from the partially transmitting mirror M_2, the phase should be a multiple of 2 π for each cavity round-trip. According to the previous discussion, the resonant TEM_{mn} optical modes must meet a round-trip phase constraint given by,

$$\varphi = 2kL + \varphi_1 + \varphi_2 - 2\vartheta_{mn} = q2\pi. \tag{4.2}$$

The parameter q is an integer and each value of q represents a different longitudinal mode of the microcavity. The separation between two consecutive longitudinal modes is known as the free spectral range (FSR), which is $\Delta L_{FSR} = \lambda/2$ in terms of cavity length or $\Delta\nu_{FSR} = c/2L$ in frequency. The full-width at half-maximum (FWHM) of the cavity signal on resonance $\delta\nu$, is defined by the cavity decay rate [18],

$$\kappa/2\pi = \delta\nu = \frac{c}{2\,\mathcal{F}\,L_{eff}}. \tag{4.3}$$

Here, $L_{eff} = L + 2L_{\varphi}$, is the effective cavity length including the separation between the cavity mirrors, L, and the DBRs phase penetration depth L_{φ}. The finesse $\mathcal{F}$ is approximately inversely proportional to $\mathcal{L}_{tot}$ as [18],

$$\mathcal{F} \approx \frac{2\,\pi}{\mathcal{L}_{tot}}. \tag{4.4}$$

Where $\mathcal{L}_{tot}$ is the round-trip loss including all the loss channels within the cavity. It is worth noting that the total cavity loss includes, the loss from mirrors like transmission, absorption and scattering loss due to mirror roughness. In addition to the loss from samples and the clipping loss caused by the fiber mirror's finite diameter, which varies with cavity length, as discussed below. The quality factor is another important aspect of the cavity, and is given as [18],

$$Q = \frac{\nu}{\delta\nu} = \frac{q\,(\lambda/2)}{\delta d} = q\,\mathcal{F}. \tag{4.5}$$

Where δd represents the cavity length resonance linewidth as FWHM. The term $q\,(\lambda/2)$ is equal to the cavity length L.

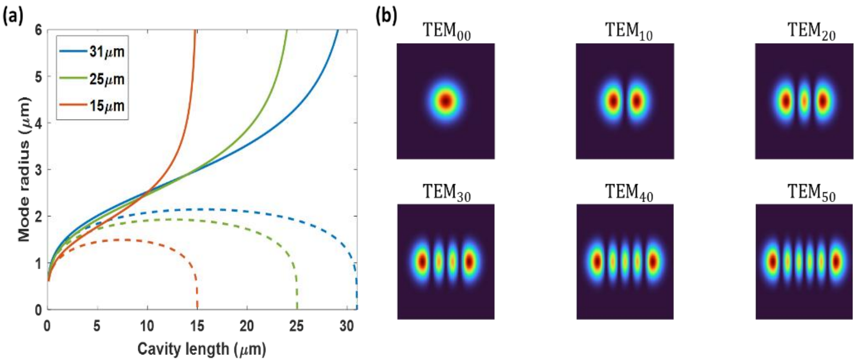

Figure 4.3: (a) Mode radii on the flat mirror w_0 (dashed lines) and on the curved $w(z)$ (solid lines) for different radii of curvature as a function of cavity length. (b) An example of Gaussian beam transverse mode profiles up to the 5th order.

4.2.2 Cavity TEM modes

Eq. (4.2) states that for a given cavity geometry, a family of TEM_{mn} modes that meet the round-trip phase condition are resonant with the cavity. The TEM_{mn} modes are in orthogonal coordinates, and the beam's transverse profile is the product of x and y components that have the same function. The derivations of the cavity beam transverse profile are well known and can be found in standard textbooks (for example, [64]). The transverse profile along x can be rewritten as,

$$E_{x,m} = A_m\, H_m\left(\frac{\sqrt{2}\,x}{w(z)}\right) \times exp\left[-\frac{x^2}{w^2(z)} - \frac{i}{2}\left(kz + \frac{k\,x^2}{R(z)} - (2m+1)\varphi_{Gouy}\right)\right]. \quad (4.6)$$

With a field amplitude, $A_m = \sqrt[4]{2/\pi}\,\sqrt{w_0/(2^m m!\; w(z))}$. H_m, are Hermite polynomials of degree m. The functions w_0, $w(z)$, $R(z)$ represents, respectively, the cavity mode waist located at the flat mirror for our microcavity geometry, the transverse beam size at the fiber mirror, the wavefront curvature radius, and they are given as [18,64],

$$\mathrm{w_0} = \sqrt{\lambda/\pi}\,\sqrt[4]{\mathrm{L(R_c - L)}} \quad (4.7a)$$

$$\mathrm{w(z)} = \mathrm{w_0}\sqrt{1 + (\mathrm{z/z_R})^2} \quad (4.7b)$$

$$\mathrm{R(z)} = \mathrm{z}\,(1 + (\mathrm{z_R/z})^2) \quad (4.7c)$$

Where $z_R = \pi\, {w_0}^2/\lambda$ is the Rayleigh length, which determines the distance at which the beam size is near to its minimum (to within $\sqrt{2}w_0$). As can be seen in Fig. 4.3a, the minimal mode waist radius is located at the flat mirror, where the rare-earth ion sample is placed. For rare-earth ion samples with 80-100 nm radius as used in our measurements, the beam waist may limit the resolution for microscopy [65]. As the cavity length approaches the radius of curvature of the fiber mirror, the mode size on the curved mirror diverges and the cavity becomes unstable. It is obvious from Fig. 4.3b that the higher order modes spread out further in diameter as the mode index m increases. The numerical calculations derived in [65, 66], shows that the mode patterns of the higher-order modes (HOMs) spread out considerably farther than the lowest order Gaussian mode ($m = 0$) by a factor approximately given by $\sqrt{m+1}$. As a result, the edges of the curved mirror may truncate the mode sizes of HOMs, causing a quick increase in energy losses for all modes with higher indices and this is elaborated next in Section 4.4.

4.2.3 ABCD matrix and stability condition

According to geometrical optics and paraxial-ray approximations, the propagating beam between two planes can be represented by an ABCD matrix that characterizes all optical elements between the two planes [64]. For the microcavity shown in Fig. 4.2a, constituted by a flat mirror and curved mirror separated by a distance L, the round-trip matrix starting from mirror M_1, is then given by,

$$\mathrm{M_{rt}}=\mathrm{M_{flat,refl}}\ \mathrm{M_p}\ \mathrm{M_{Fib,refl}}\ \mathrm{M_p} = \begin{pmatrix} \mathrm{A} & \mathrm{B} \\ \mathrm{C} & \mathrm{D} \end{pmatrix} \tag{4.8}$$

Where $\mathrm{M_{flat,refl}}$ represents the ABCD matrix of the flat mirror, M_p represents propagation in vacuum over a distance L, and $\mathrm{M_{Fib,refl}}$ is the ABCD matrix of the curved mirror given as [64],

$$\mathrm{M_{flat,refl}} = \begin{pmatrix} 1 & 0 \\ 0 & 1 \end{pmatrix}, \mathrm{M_{Fib,refl}} = \begin{pmatrix} 1 & 0 \\ -2/\mathrm{R_c} & 1 \end{pmatrix}, \mathrm{M_p} = \begin{pmatrix} 1 & \mathrm{L} \\ 0 & 1 \end{pmatrix}, \tag{4.9}$$

Where $\mathrm{R_c}$ represents the radius of curvature of the fiber mirror. For the resonator to be stable, the beam after one round trip should not diverge. This means that the ABCD matrix given in Eq. (4.8) must not diverge as well. This implies that the trace (A+D) of the round-trip matrix is of modulus $|A + D| < 2$ [64]. By using Eq (4.9) and performing the matrix multiplication in Eq. (4.8), we obtain,

$$-2 < \left[A + D = 4\ \left(1 - \frac{L}{\mathrm{R_c}}\right) - 2\right] < 2 \tag{4.10}$$

$$0 < \left(1 - \frac{L}{\mathrm{R_c}}\right) < 1 \tag{4.11}$$

Eq. (4.11) gives the stability condition of the flat-curved microcavity discussed in this thesis. This condition corresponds to a cavity length L larger than zero and less than the radius of curvature of the curved mirror $\mathrm{R_c}$. In practice, the shortest cavity length possible between the two cavity mirrors is limited by the mirror depth $\mathrm{z_t}$, as illustrated in Fig. 4.4. The mirror depth is given as, $z_t = a^2/2R_c$ and it depends on curved mirror geometry such as cut-off diameter (D = 2a) and radius of curvature R_c [18].

4.3 Transverse modes excitations

In this section, we examine the parameters that influence the effective coupling of higher-order spatial modes to the microcavity, with the goal of utilizing them for stabilization. As elaborated in Section 4.5, higher-order modes, particularly those with odd indices, exhibit reduced overlap with single-mode fibers. Consequently, employing these higher-order modes as a stabilization beam can minimize the leakage of photons to the fluorescence detector during measurements. This method reduces reliance on wavelength filters and allows the stabilization beam to function in continuous mode. This improvement increases the efficiency of cavity length stabilization by minimizing cavity length jitter during fluorescence collection, which is essential for achieving high effective Purcell enhancement (see Section 3.3.1).

Equations (4.6) and (4.7) can be utilized to characterize a resonant mode, such as the well-known fundamental Gaussian beam TEM_{00}. In a perfectly aligned and mode matched cavity, only the fundamental mode can resonate in the cavity. However, maladjustments in the input beam alignment and mode matching give rise to off-axis mode couplings [67], and modes of different orders, i.e., having different transverse profiles, can resonate simultaneously. Indeed, the cavity field distribution on the Hermite-Gauss basis should be expanded, and the Gouy phase shift for each basis mode can be taken into account.

Furthermore, in order to efficiently evaluate the cavity response over the excited transverse modes, the incoming beam's projection with respect to the cavity reference coordinates is required. Figure 4.4 illustrates the necessary transformations to convert the incident beam coordinates (x′,y′,z′) with angle θ to the reference coordinates (x,y,z). The fraction of the incoming beam that is coupled to a particular TEM_{mn} mode is given by the overlap between the amplitude of the cavity field and the incoming beam,

$$C_{x,m} = \int F_x(x,z)\, E^*_{x,m}(x,z)\; dx \qquad (4.12)$$

Where the $E^*_{x,m}(\mathrm{x,z})$ is the complex conjugate of the spatial field amplitude given by Eq. (4.6) and the function $F_x(x,z)$ represents the incoming beam amplitude defined as,

$$F_x(x,z) = \tilde{A}_0 exp\left[- K_x\, x'^2 - \frac{i}{2}\left(kz' - \varphi_{Gouy}\right)\right] \qquad (4.13)$$

with $\tilde{A}_0 = \sqrt[4]{2/\pi}\, \sqrt{\mathrm{w}_0/w(z')}$, x′ and z′ are the incident coordinates given as in Fig. 4.4. The factor $K_x = [(ik/2R(z')) + 1/\mathrm{w}(z')^2]$, with $R(z')$, and $\mathrm{w}(z')$ given similarly to Eqs. (4.7) as a function of z'. w_0 represents the incoming beam waist at the flat mirror and is given by Eq (4.7 a).

The whole intracavity field describes the complete set of cavity modes excited by an input paraxial field that may enter the cavity from the flat mirror side of the cavity and is given as,

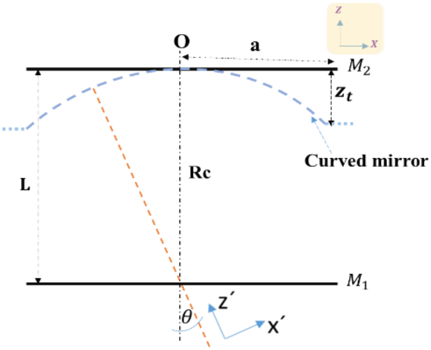

$$\begin{cases} \acute{x} \cong x\cos(\theta) - z\sin(\theta) - x_0 \\ \acute{y} \cong y - y_0 \\ \acute{z} \cong x\sin(\theta) + z\cos(\theta) \end{cases}$$

Figure 4.4.: shows the coordinates for an incident beam with tilt angle θ to excite HOMs. The included transformation is used to convert the incident coordinate (x´,y´,z´) to the reference coordinate (x,y,z) with axis offsets x_0 and y_0.

$$E_x^{IC}(x,z,\varphi) = \frac{1}{t_2}\sum_{\mathrm{m}=0}^{\mathrm{M}} C_{x,m}\, E_{x,m}\, \frac{t_1 t_2}{1 - r_1 r_2 exp[i\varphi]} \tag{4.14}$$

Here *M* is the maximum index value to be kept in a finite expansion. Odd-indexed HOMs are especially useful because, unlike even HOMs, they have a lower coupling to the single-mode fiber (SMF) mirror.

As will be shown later, this minimizes the number of stray photons that reach the fluorescence detector when they are used to stabilize the cavity length. E_x^{IC} given by Eq. (4.14) is equivalent to the cavity transmission, times a factor of $1/t_2$ because we are taking this field before the output mirror transmission. φ is the round-trip phase given by Eq. (4.2). The expression $\frac{t_1 t_2}{1 - r_1 r_2 \exp[i\varphi]}$ identifies longitudinal cavity resonances. The resonance condition for different HOMs with longitudinal mode order q and transverse mode order (*m*, *n*) can be defined as,

$$L_{qmn} = \frac{\lambda}{2}\left(q + \frac{\vartheta_{m,x}}{\pi} + \frac{\vartheta_{n,y}}{\pi}\right) \tag{4.15}$$

Where $\vartheta_{m(n),x(y)} = [m\ (n) + 1/2]\varphi_{gouy}$ is given by Eq. (4.1). Notably, the higher order transverse modes resonate at longer cavity lengths than the fundamental mode of a longitudinal mode order q, as indicated by Eq. (4.15). Additionally, the separation between these modes increases with an increase in mirror separation (large mode order q).

Figure 4.5 shows the results obtained by Eq. (4.14). In a perfectly aligned and mode matched cavity, only the fundamental mode resonates in the cavity (blue line), but if the incident beam is misaligned relative to the cavity axis, HOMs also resonate. Figure 4.5 illustrates that tilting the incoming beam at an angle $\theta = 6°$ while examining a 1 μm axis offset relative to the cavity axis z can excite up to 5th order modes within narrow-band dielectric mirror coatings. The resonant modes shown in Fig. 4.5 corresponds to TEM_{00}, TEM_{10}, TEM_{30} and TEM_{50} (orange line). These modes occur at wavelengths that can be spectrally filtered in comparison to the fundamental mode at 892 nm, which is aligned with the RE ions under this study. The parameters used for calculations are optimized to have high coupling efficiency for TEM_{10} as shown in Fig. 4.5 while the other HOMs exhibit different coupling efficiencies within the cavity. This variation arises because the coupling efficiency of each TEM_{mn} mode is primarily influenced by factors such as cavity length, incidence tilt angle, and axis offset, which will be further detailed in Fig. 4.7a. On resonance, the intracavity power of each HOMs can be derived from Eq. (4.14) in terms of the finesse which include all loss channels as given by Eq. (4.4). The maximum intracavity power can be derived as $P_{IC} = T_1(\mathcal{F}/\pi)^2 P_{in}$, here both the transmission and reflectivity are assumed to be independent with regard to which transverse mode is used.

The calculations performed in this section assume a perfect sphere of the micromirror. Due to manufacturing imperfections the profile shape of the machined mirror deviates from a perfect sphere leading to ellipticity of the mirror profile [68,69].

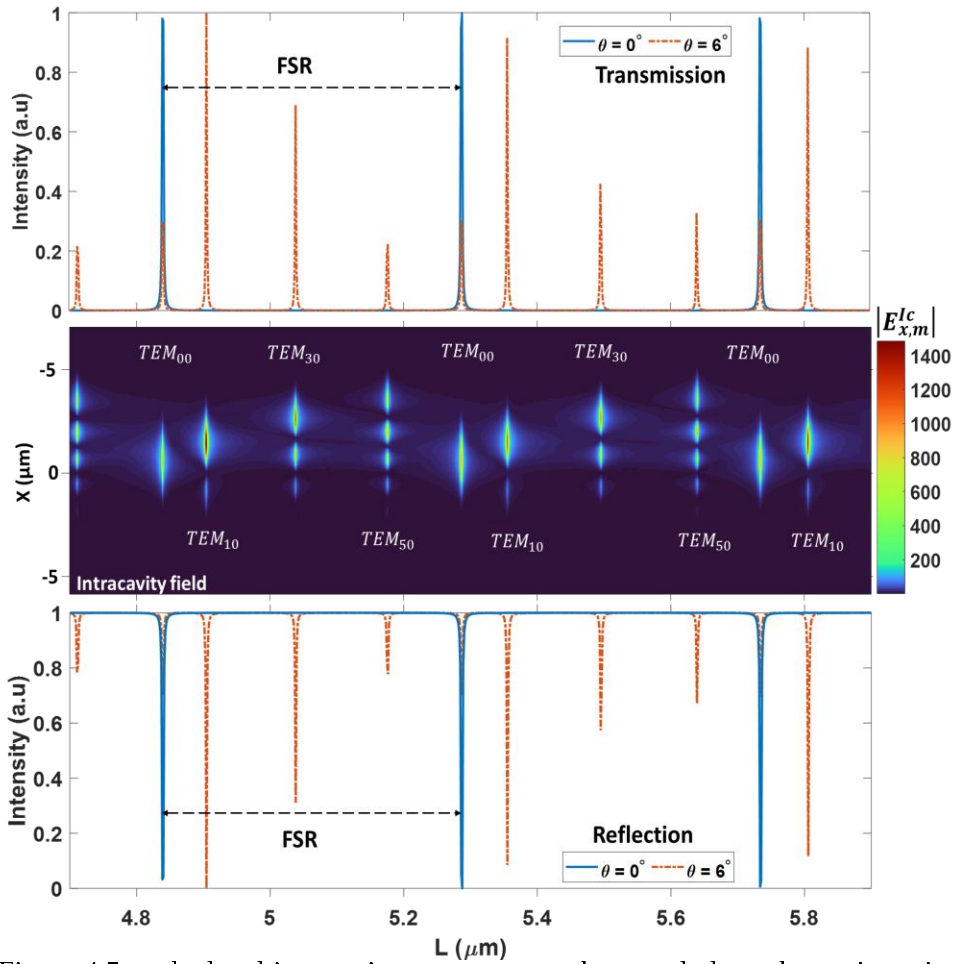

Figure 4.5.: calculated intracavity transverse modes travel along the cavity axis z and the corresponding transmission and reflection resonances when the cavity length is scanned across two FSR. The color code corresponds to the intracavity field amplitude given by Eq. (4.14). The calculations are performed for an empty cavity with reflectivity of 99% and a curved mirror with radius of curvature of 31 μm and 935 nm wavelength. The normal and tilted incident field effect is included in the cavity transmission and reflection spectrum. The incident beam coupling with 6 ° angle results in an observable offset from the x-axis for various cavity modes.

In the case of elliptical mirror profiles, the resonances exhibit a splitting into doublets that correspond to orthogonal polarizations. For smaller fiber profiles, which generally have a low ellipticity, this splitting may be less than the linewidth [69]. In the experiments conducted in this study, the polarization of the incoming light was consistently selected to ensure that only one of the two lines was targeted.

4.4 Diffraction loss

Diffraction losses occur due to the limited dimensions of mirrors, which disturb the field at the edges, leading to beam truncation and a deviation from a pure Gaussian mode caused by the mirrors' finite size. This section discusses how diffraction loss affects TEM_{00} and higher-order modes as they propagate within the microcavity which consists of the flat mirror and curved mirror with a finite cut-off radius. An estimation of diffraction losses for various modes is required to evaluate cavity length stabilization using different modes. This is due to the feedback gain of the closed loop being determined by the slope of the error signal, which is in turn determined by the resonance's finesse as detailed in Chapter 6. Figure 4.6 shows that the higher-order modes exhibit different diffraction losses in relation to the cut-off radius (Fig. 4.6a) and cavity length (Fig. 4.6b). These variations significantly affect the finesse (shown in Fig. 4.6c) as a result of the diffraction loss.

For a given microcavity, the final field distribution on the flat mirror after one round trip must reproduce its shape. However, the transverse mode pattern will be reduced in amplitude and shifted in absolute phase by the complex eigenvalue γ_{mn}. The eigenvalues γ_{mn} after one round trip at the same input plane (in our case it is M_1) will satisfy the simplified round trip propagation expression [64]:

$$\gamma_{mn}\, E_{mn}(x,y,0) = \int_{-\infty}^{\infty}\int_{-\infty}^{\infty} \mathbb{K}(\bar{x}_1,\bar{y}_1;x_1,y_1)\, E(x_1,y_1,0)\, dx_1\, dy_1. \quad (4.16)$$

Where the double integral is taken over the infinite diameter of the flat mirror M_1, with the overall kernel $\mathbb{K}$ given as,

$$\mathbb{K}(\bar{x}_1,\bar{y}_1;x_1,y_1) =$$

$$\int_{-a}^{a}\int_{-a}^{a} \underset{M2\to M1}{\mathrm{K}}(\bar{x}_1,\bar{y}_1;x_2,y_2)\ \underset{M1\to M2}{\mathrm{K}}(x_2,y_2;x_1,y_1)\ dx_2\, dy_2. \quad (4.17)$$

where $\underset{M1\to M2}{\mathrm{K}}(x_2,y_2;x_1,y_1)$ represents the propagation kernel from the flat mirror M_1 at $z = 0$ to $z = L$, where the curved mirror M_2 is lying. $\underset{M2\to M1}{\mathrm{K}}(\bar{x}_1,\bar{y}_1;x_2,y_2)$ represents the propagation kernel from $z = L$ going back to $z = 0$, but the total length traveled is 2L and the double integral in Eq. (4.17) is taken over the curved mirror cut-off radius a.

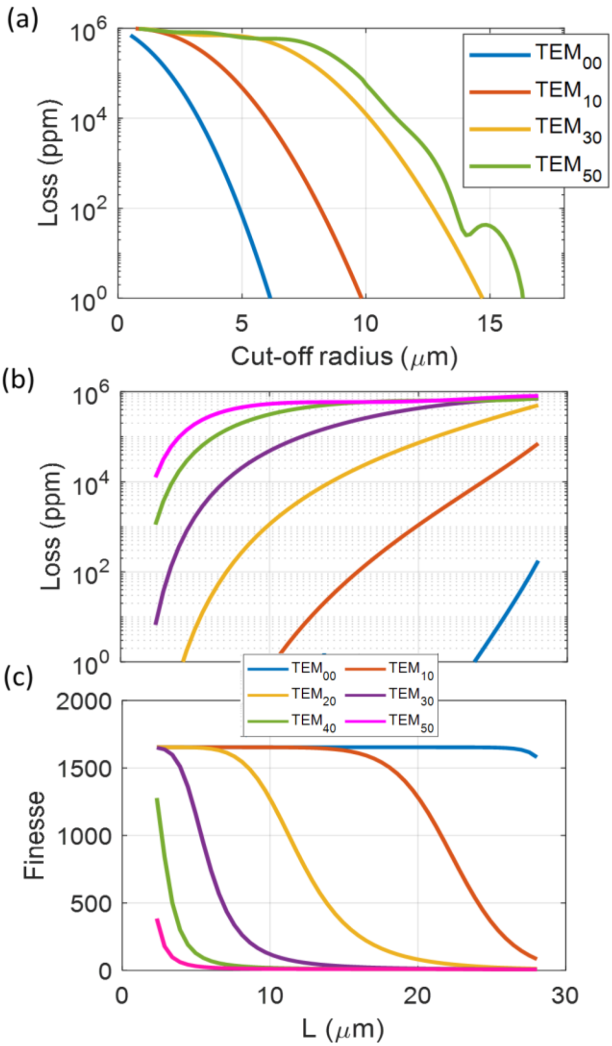

Figure 4.6: The round-trip diffraction loss experienced by the curved fiber mirror with finite cut-off radius. (a) Diffraction loss introduced from the fiber mirror with different cut-off radius and for different higher order modes excited in a cavity. (b) The diffraction loss up to 5th modes within the microcavity as a function of the cavity length. The calculations are performed at $R_c = 31\ \mu m$ and a mirror cut-off radius $a = 10\ \mu m$, which are typical values for our setup. (b) The variation in the finesse of such a cavity, resulting from diffraction loss, is calculated at up to 5th order modes.

The magnitude $|\gamma_{mn}|^2$ of the eigenvalues due to the round-trip losses gives the remaining intensity after one round trip and the yield losses introduced to the cavity mode due to the diffraction losses from the finite radius of the curved mirror is given as,

$$Power\ loss\ per\ round\ trip\ = 1 - |\gamma_{mn}|^2. \tag{4.18}$$

Figure 4.6 gives a typical example of losses introduced to various HOMs coupled separately to the cavity mode with a mode radius w_m impinging on a fiber mirror of finite cut-off radius a. The larger spatial distributions of HOMs may give greater diffraction loss compared to the fundamental mode. Figure 4.6a, shows the diffraction loss of the cavity modes at different cut-off sizes. As shown in Fig. 4.6a, lower index modes, such as $m + n = 0$ and $m + n = 1$, can reach performance that is not limited by clipping loss, whereas higher-order modes are significantly affected by diffraction loss. For a fiber mirror with a cut-off radius of 10 µm, the various cavity modes get altered significantly with the diffraction loss as the cavity length increases (see Fig. 4.6b). The reason for this is that the mode waist $w_m = \sqrt{m+1}\, w(z)$ is impacting the fiber mirror with a finite radius, which increases as the cavity length grows, leading to further truncation. In Fig. 4.6c, the diffraction loss contribution to the cavity finesse is calculated by using Eq. (4.4). The finesse of the higher order modes decreases significantly as the separation between the cavity mirror increases. To achieve performance that is not constrained by diffraction loss, a fiber mirror with a cut-off radius $a > 3w_m$ is required to couple up to 5th odd indexed HOMs to the cavity without further clipping loss. These investigations can provide insights into the performance of cavity length stabilization by utilizing various higher-order modes, as will be elaborated on later in Section 6.5.

4.5 Coupling efficiency

The coupling efficiency between different components of the microcavity, e.g., incident beam to cavity mode through the flat mirror and intracavity mode to single mode fiber SMF, can be computed as

$$\eta_{mn} = \frac{|\iint E_{mn}^*(x,y)\, F(x,y)\, dx\, dy|^2}{\iint |E_{mn}(x,y)|^2\, dx\, dy \iint |F(x,y)|^2\, dx\, dy} \tag{4.19}$$

Where the $E_{x,m}^*(x, y)$ is the complex conjugate of the spatial field amplitude inside the cavity given by Eq. (4.6). The function $F(x, y)$ represents the incoming beam amplitude defined by Eq. (4.13) or the near-field fundamental mode distribution of the single mode fiber, depending on the interface in question.

4.5.1 Coupling through flat mirror

Due to the small mode size at the flat mirror (see Fig. 4.3), spatial mode matching to the cavity mode is achieved with an aspheric lens that offers diffraction limited performance. This aspheric lens has a numerical aperture (NA) of 0.6, resulting in a spot size of approximately 1.5 µm at the flat mirror and a depth of field of 3 µm, thereby achieving optimal mode matching. Figure 4.7a shows that the coupling efficiency of odd indexed HOMs are mainly determined by the cavity length and incidence tilt angle, in addition to axis offset (not included in Fig. 4.7a).

4.5.2 Coupling through fiber mirror

The fraction of the intracavity mode TEM_{mn} coupled to TEM_{00} mode of the single mode fiber SMF is given by the overlap integral given by Eq. (4.19). The function $F(x, y)$ represents the fundamental mode distribution of the single mode fiber and can be well approximated by a Gaussian function of the form,

$$F(x,y) = F_0 \exp\left[-4\frac{(x^2+y^2)}{\mathrm{MFD}^2}\right] \tag{4.20}$$

Where F_0 is a constant and MFD represents the Gaussian mode field diameter of the fiber at the operating wavelength.

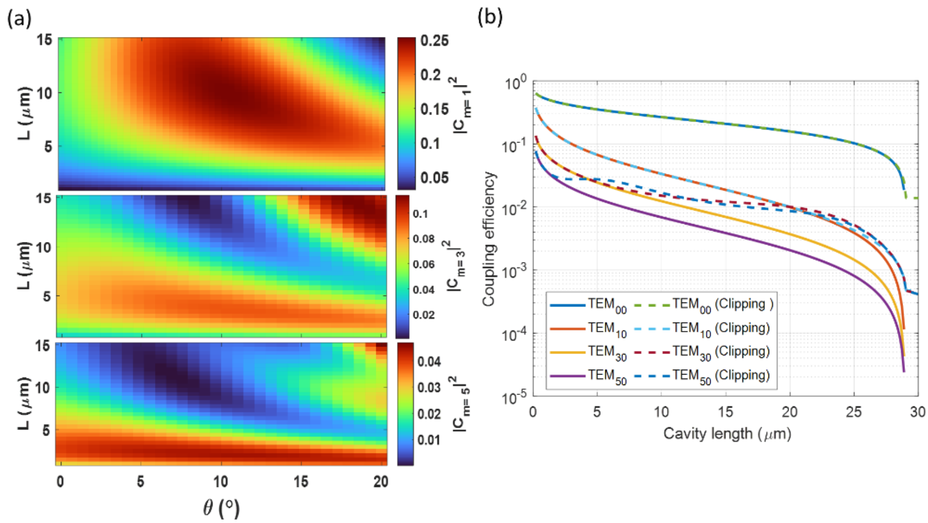

Figure 4.7: (a) The coupling efficiency of the odd indexed TEM_{mn} modes to the cavity modes as a function of tilt angle of the incident beam and the cavity length. (b) The coupling efficiency between the cavity mode and the single mode fiber, both with and without considering diffraction loss due to the limited size of the mirror.

For a step-index single-mode fiber, the following empirical expression may be used to determine MFD [70]:

$$\mathrm{MFD} = 2w_{\mathrm{core}} \times \left(0.65 + \frac{1.619}{\mathrm{V}^{1/2}} + \frac{2.879}{\mathrm{V}^{6}}\right), \tag{4.21}$$

$$\mathrm{V} = \frac{2\pi\, w_{\mathrm{core}}}{\lambda} \sqrt{\mathrm{n}_{\mathrm{core}}^{2} - \mathrm{n}_{\mathrm{clad}}^{2}}, \tag{4.22}$$

Where w_{core} is the core size, n_{core} and n_{clad} are the fiber core and cladding refractive indices. V is the well-known fiber dimensionless parameter, and for SMF, it should be less than 2.4 [70]. We take the double integral over the infinite mirror diameter to calculate the maximum coupling efficiency between the cavity mode and the single mode fiber, and then compare it with the results over the finite diameter of the fiber mirror. Figure 4.7b indicates that the overlap between odd indexed HOMs and SMF with MFD of about 5 µm results in mode suppression by 10-100 folds dependent on the cavity length. However, the finite diameter of the fiber mirror may lower this suppression, particularly for TEM_{30} and TEM_{50} at long cavity length.

4.6 Evaluation of HOMs as a Stabilizing Beam

According to previous discussions, higher-order spatial modes can assist in addressing the challenge of integrating the stability beam working in continuous mode with fluorescence detection. This can be achieved by detecting fluorescence through single mode fibers, which inherently suppress higher-order modes needed for stabilization by more than 100 times when compared to the fundamental mode, reducing the need for wavelength filters but can also work in combination with such filters. One issue associated with higher order modes is the clipping loss that arises from the cut-off radius of the micromirror, which leads to a decrease in finesse. This factor plays a crucial role when utilizing higher order modes for stabilization, as the effectiveness of cavity length stabilization is highly reliant on the slope of the fringe side employed for this purpose. Future setups can mitigate this issue by producing micromirrors with a larger cut-off radius that aligns with the desired modes. This approach not only reduces clipping loss but also allows for the excitation of modes up to TEM_{90}, resulting in a suppression of 10^4 in error photons from the locking beam.

5 Mechanical Modeling and Assembly Design

The aim for this project has been building a setup to detect single rare-earth ions, which places challenging requirements on the microcavity assembly in terms of robust mechanical stability, low temperature operation and optical access. Previously, a first attempt to make such an assembly was made and although some early fluorescence measurements were realized, the assembly never reached the required stability or operation performance. In this chapter, I go through the process of designing the second generation of an assembly that meets all the requirements. Solidworks simulation tools are utilized to model the assembly performance at low temperature and investigate the mechanical responses. The upcoming chapters will detail the experiments conducted on the new design.

5.1 The challenge

Designing a customized cavity assembly capable of fitting any material is interesting for quantum computing applications. Such applications require the selection of materials with high coherence properties. One challenge of such a cavity is the mechanical stability which is needed to maintain the cavity on resonance with the narrow transition of the emitter for long time periods. This necessitates that the relative positions between the cavity mirrors remain constant. Mechanical disturbances from the surroundings, along with electronic noise from the nanopositioning controllers, may counteract this goal. The cavity assembly is embedded at cryogenic temperatures of about 1 K. This requires a more rigid assembly in order to minimize excessive strain while allowing the stable and fast transverse scan of one of the cavity mirrors. To fulfill these needs, a more integrated mechanical model is developed here.

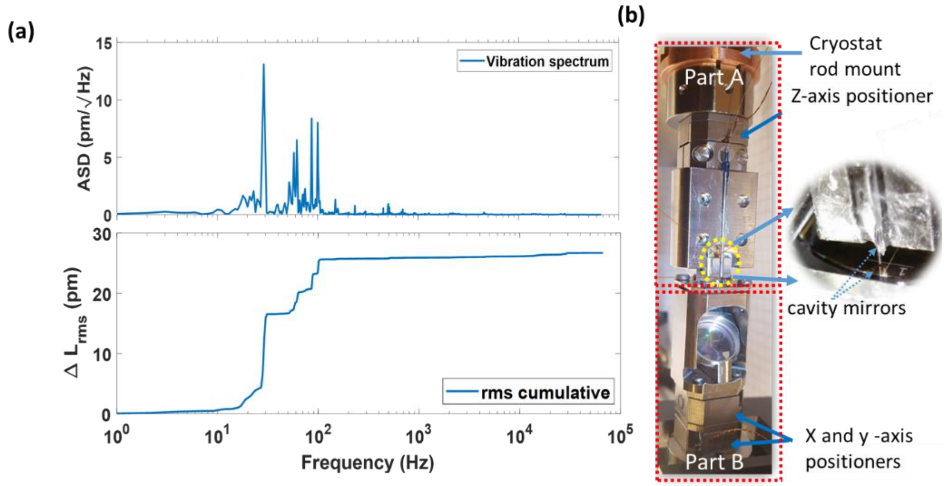

Figure 5.1: Old cavity setup stability performance at room temperature. The spectral analysis of the cavity length fluctuations obtained by side of fringe locking technique. The cavity resonance frequencies (top) and cumulative rms noise (below). (b) a photograph of the old cavity setup with the main components [15, 71].

5.2 Performance of the first-generation setup

Before my PhD, the first assembly prototype was developed and is described in Ref [15,71]. The first cavity setup (see Fig. 5.1b) used commercial ANPx51 and ANPz51 slip-stick positioners from Attocube to control the cavity length and the transverse scanning of the mirror. With this, long scan range translations of about 2.5 mm on all cavity axes are possible with nanometer resolution. Long scanning ranges along the cavity axis and throughout the sample are required to counteract contraction during cooldown to low temperatures and to resolve the structures of interest. However, the design of the first prototype resulted in lower mechanical resonance frequencies, leading to further instability. Another problem of the positioners is that their operation is dependent on the friction between its parts [15]. This causes the assembly to shake when driving, and makes it difficult to reliably scan an area on the mirror. The other challenge was related to the rigidity of the cavity parts assembly. The previous design was constrained by the geometry of an older cryostat with only 25 mm diameter space, barely accommodating the positioning stages, leaving no room for a rigid design. The cavity components (part A and part B in Fig. 5.1b) were attached together by a cylinder, fixed by screws, and mounted vertically along the cavity axis to the end of the cryostat rod, making it highly susceptible to low frequencies and relative drifts between the cavity parts.

This added some difficulty to be actively stabilized at low temperature even with a low finesse cavity. The performance of the cavity operation can be determined by measuring the fluctuations in cavity length (see Fig. 5.1a). We measured the transmission fringes of the cavity after the outcoupling mirror by using a photodiode (PD). The slope of the side of fringe was employed to convert the voltage level to positional readout. The amplitude spectrum density (ASD) and the cumulative root mean square (rms) length fluctuations of the setup were obtained by using the Fast Fourier Transform of the cavity transmission. As shown in Fig. 5.1a, the cavity setup exhibited high susceptibility to low frequencies, with the maximum resonance peaks occurring between 30 Hz and up to 500 Hz. A 30 pm rms cavity length jitter was demonstrated when active stabilizing a cavity with a finesse of 700. These fluctuations make it challenging to actively stabilize a high finesse cavity (less than 15 pm rms length stability is needed for 3000 finesse), which is required for sufficient Purcell enhancement of the readout RE ions.

During working on the first cavity assembly, I gained initial knowledge into the impact of assembly parts, proportional-integral (PI) controllers, cavity translation stages, electrical noise, and noise suppression. The next step was to employ this knowledge to develop a rigid and high passive stability mechanical model and determine if these improvements, in addition to active stabilization, could reach a stability of less than 15 pm rms on the length scale with an acceptable transverse scan range of one of the cavity mirrors.

5.3 Requirements for improving stability

In our case a cavity of 3000 finesse is used for Purcell enhancement of rare earth ions as stated in Section 3.3. To not destroy this enhancement, the fluctuations in the cavity length during the measurements should be at least one order of magnitude less than the full width at half maximum (FWHM) of the cavity resonance of 145 pm. Achieving this level of stability depends on improving both rigidity and passive stability, alongside active stabilization. Additional requirements for the cavity design are detailed below:

- The cavity length coarse scan range should be large enough to access different longitudinal mode orders, each separated by $\lambda/2$. For example, to allow for the simultaneous cavity resonance of different laser wavelengths of the stabilized beam and the sample probe beam.
- To compensate for large length drifts due to the temperature changes as well as the surrounding noise sources at cold temperatures, few microns continuous longitudinal scanning ranges are required.

- The setup should be compatible with mounting into our new cryostat chamber (diameter approximately 48 mm).
- The movement along all axes, including the cavity length and transversal scan axes, should be repeatable.
- To enhance usability, the cavity should feature quicker scannable cavities and improved data acquisition speeds.

During the design phase, many suggestions for potential improvements were considered, as detailed below.

5.4 Implementations to the new design

5.4.1 Enhancing rigidity.

To reduce susceptibility to low frequencies and minimize the strain at low temperature, the assembly should be as stiff as possible. This could be improved by

- Building all the assembly parts in the same base housing block.
- Titanium is used to manufacture assembly parts and nanopositioners due to its low thermal expansion coefficient and excellent mechanical rigidity, which reduces relative thermal contraction during cooling.

5.4.2 Stable moving components

This could be achieved by,

- Minimize moving parts to avoid low resonance and build-up frequencies.
- Increasing the mechanical bandwidth along the cavity axis by using a low load.
- Thicker walls (rigidity).
- Improving the contact between the assembly parts, particularly the fiber mirror and the flat mirror holders.
- Separating the cavity axis from the movement in X and Y might help in lowering coupling frequencies and ensuring beam alignment.
- Using low load, precise and low noise nanopositioning for the transversal scanning of the cavity mirror and the cavity axis control.

- Using suitable springs to decouple frequencies which could couple to the cavity from the surroundings.

5.5 New mechanical modelling

Figure 5.2 illustrates the second-generation assembly design with its main components (see Paper I for more details). It utilizes an integrated passively damped base housing block to improve stiffness and rigidity while reducing impact on the environment coupling. The cavity length and the transversal scan of the mirror with samples is controlled by fine and coarse tuning translation stages with complete access in XYZ directions and two degrees of angular alignment in the YZ plane (where Z refers to the cavity length). In addition, a fully adjustable aspheric lens is included for cavity mode matching using the flat mirror.

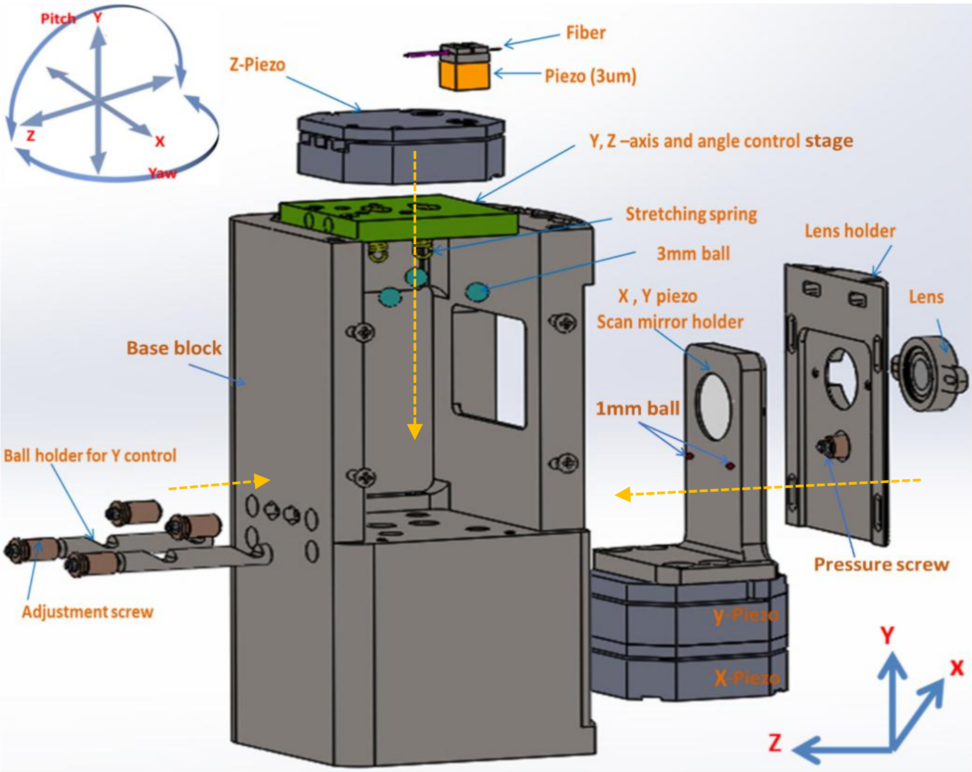

Figure 5.2: The second-generation assembly of the microcavity with the main components. The yellow arrows indicate the direction in which the various components should be assembled.

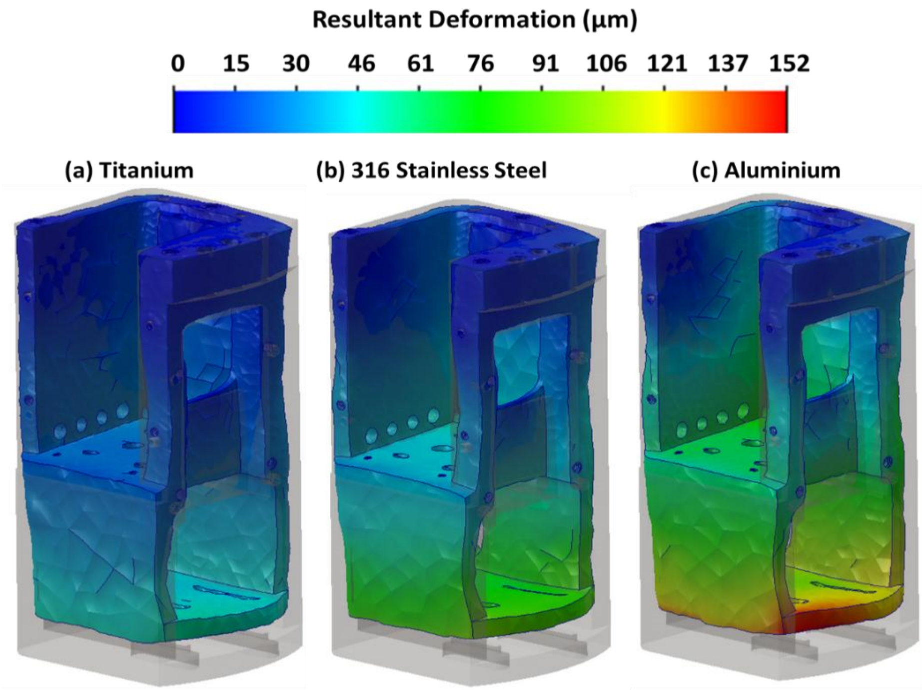

Figure 5.3: Simulated exaggerated thermal deformation of the assembly base block made of Titanium, stainless steel and Aluminum when cooled down from room temperature to1 K. The block with transparent side showcases the structure at room temperature.

5.5.1 Material choices

Choosing materials with high resonance frequencies and low thermal drifts are required to improve the mechanical stability with noisy and low temperature surroundings. Solidworks simulations are performed for Titanium, stainless steel and Aluminum. Due to their similar density to elastic module ratio, the same natural resonance frequencies are obtained. However, an assembly setup made of Titanium has lower thermal deformations at 1 K compared to stainless steel and Aluminum (see Fig. 5.3) due to the smaller thermal expansion coefficients (Titanium: 9 ppm/K, 316 steel: 17.2 ppm/K, Aluminum: 23 ppm/K). In addition, Titanium is the same material as the nanopositioners that are used to control the transversal position of the cavity mirror and the cavity length, which minimizes the relative thermal drift of different components.

The fine adjustments screws and threaded Bushing (Thorlabs F2ES6 Adjuster and F2ESN1P Threaded Bushing) are made of stainless steel and Phosphor Bronze, respectively. The compression and extension springs used to clamp the assembly parts to the base block and hold the assembly in the cryostat are made of stainless steel, which is nickel plated to reduce the magnetism in stainless steel. The balls of 1 mm and 3 mm diameters are also made of stainless steel, and are used for contact between the mirror holder and the base block with the fiber mirror so that the top stage (angle control stage, Fig. 5.2) can still slide for coarse alignment.

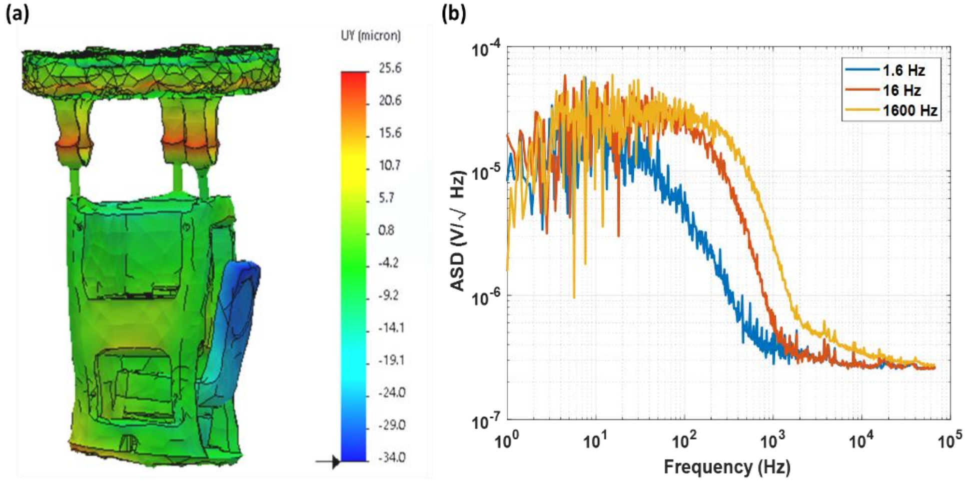

Figure 5.4: (a) Exaggerated thermal deformation simulation of the cavity assembly hanging from the roof of a cryostat cold plate at 1 K. The deformation is displayed in vertical axis. (b) The spectral noise density output of ANC300/ANM200 controller for nanopositioners at different internal setting filters.

5.5.2 Positioners

The slip-stick-based positioners employed in the previous assembly induced vibrations during the transverse scan and the cavity length control, resulting in reduced mechanical stability. To avoid that in the new assembly the all-piezo-based low noise nanopositioners ANSx150 and ANSz100 from attocube are used. A transversal scan range of 80 × 50 µm at room temperature and 125 × 30 µm at low temperature with high precision in X/Y axes can be achieved. With the combination ANSx150 + ANC300/ANM200 drivers only half of the full scanning range of 125 µm is available at low temperature. The reason is that the ANSx150 is bidirectional, i.e., negative voltages can also be applied here, but the ANM200 module can only output positive voltages. With the scanners and the ANM200 module it is able to scan or fine positioning the sample by applying a DC voltage through the ANM200. The ANM200 controller is equipped with output filters at 1.6, 160, and 1600 Hz. For fast transversal scan, X and Y positioners use a 1600 Hz filter, whereas the cavity length controller uses 1.6 Hz, since this directly impacts the cavity stability. Figure 5.4b depicts the controller output noise as amplitude spectral density (ASD)

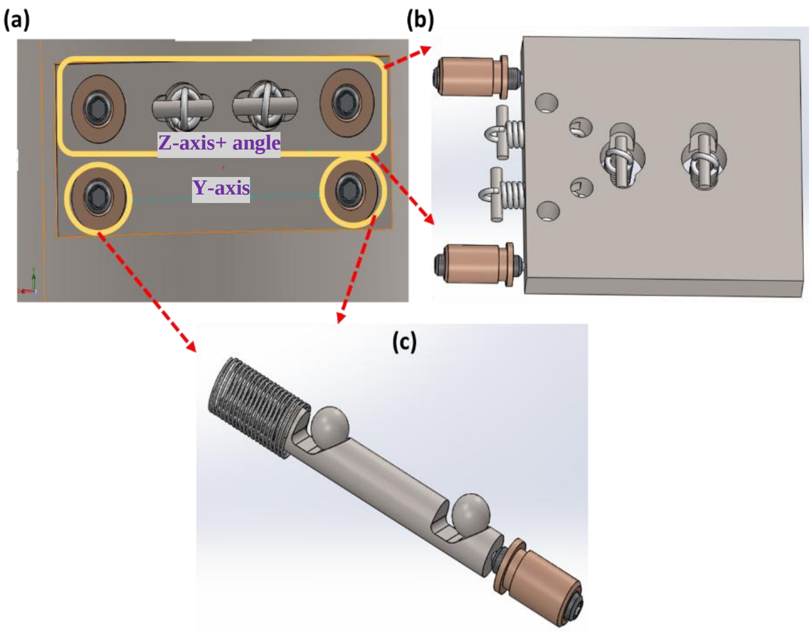

Figure 5.5: (a) The rear of the base block with actuators used to control the cavity Z axis for coarse scan and the Y axis to overcome the limited scan range of the fine nanopositioners. (b) Angle control stage clamped to the base block by four extension springs and pins. (c) The F2ES6 micro screws adjuster and the F2ESN1P threaded bushing are in contact with a titanium rod that holds two 3 mm balls for Y-axis control, and they are connected to a compression spring at the end.

for different filters. The only drawback of these positioners is their limited tuning range, particularly at low temperatures. Therefore, if we use coarse tuning to identify a good sample at room temperature and then put it in the cryostat and cool down, there is a risk that the scan range may be insufficient to compensate the drift due to thermal contraction. Therefore, choosing the nanopositioners are based on a few requirements. A small relative drift between the fiber tip and the center of mirror at low temperature is required. This can be checked by simulating the assembly's thermal contraction from room temperature to 1 K and estimating the relative drift between the fiber tip and the mirror, as illustrated in Fig. 5.4a. The results show a relative drift of 12 µm in the X and Z axes and 16 µm in the Y axis compared to room temperature, which are within the positioners scan range. Additional micro-adjustment screws can be used to control the position of the sample at room temperature by using an angle control stage (see Fig 5.5b).

This control stage can be adjusted using four adjusters (Thorlabs F2ES6 Adjuster and F2ESN1P Threaded Bushing). The stage provides 200 µm/rev of fine adjustment over 2.5 mm of travel in the Y and Z axes with pitch and yaw angles of

0.6°/rev (see Fig. 5.5). In addition, it is essential to bring sufficiently large ensembles of nanoparticles onto the flat mirror with high homogeneity and avoiding agglomerations. This ensures that, even if the thermal drift caused by thermal contraction surpasses the capabilities of the piezo, there is a high chance to still find a single nanocrystal.

5.5.3 Spring systems

The angle control stage (Fig 5.2 and Fig 5.5b) is mounted to the base block by using four extension springs with a force of 10 N each, calibrated so that the stage moves smoothly on the four stainless steel spheres with a diameter of 3 mm. The specifications of the extension springs are presented in Table 5.1

D_m (mm)	D_t (mm)	n_t	L_0 (mm)	L_n (mm)	Type
3.75	0.35	12	15	4.5	compression
2.8	0.5	12	13.5	18	extension

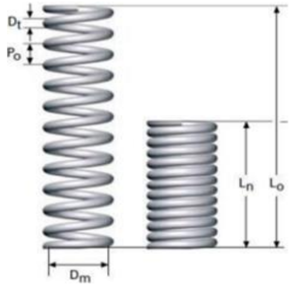

Table 5.1: Compression and extension springs specifications used in the new assembly. D_m = outer diameter. D_t = wire diameter. n_t = total number of coils. L_0 = unloaded length L_n = loaded length.

Compression springs are designed to decouple the assembly from the higher vibration frequencies coming from e.g., the cryostat. This can be achieved by hanging the cavity assembly from the roof of the inner cell of the cryostat (see Section 2.2 in Chapter 2 for details on the construction of the cryostat) by three identical parallel compression springs, resulting in an effective spring constant of $K_{eff} = K_1+K_2+K_3=3K$. The spring constant can be given by, $K = GD_t^{\ 4}/8D_m^{\ 3}n_t$, where G is the shear modulus of the stainless-steel material, and the other coefficients are given in Table 5.1. The resonance frequency of the assembly, hung by the three springs, is dependent on the total number of active coils n_t, and it can be given by $f = \sqrt{K_{eff}/m} = 28$ Hz ($for\ n_t = 12, m = 0.8$ kg). If the driving force F_0, representing the vibrations, has a low frequency in comparison to the system's frequency f, we can anticipate the assembly to move in lockstep with it. This is similar to saying that the term $m\frac{d^2x}{dt^2}$ plays a small role compared to the term K_{eff}x in the motion equation, $\left[m\frac{d^2x}{dt^2} + K_{eff}\,x = F_0 cos(\omega t)\right]$. Therefore, the amplitude is controlled by the spring constant K. On the other hand, at frequencies very large compared to the frequency f, the opposite situation holds. The K_{eff}x term

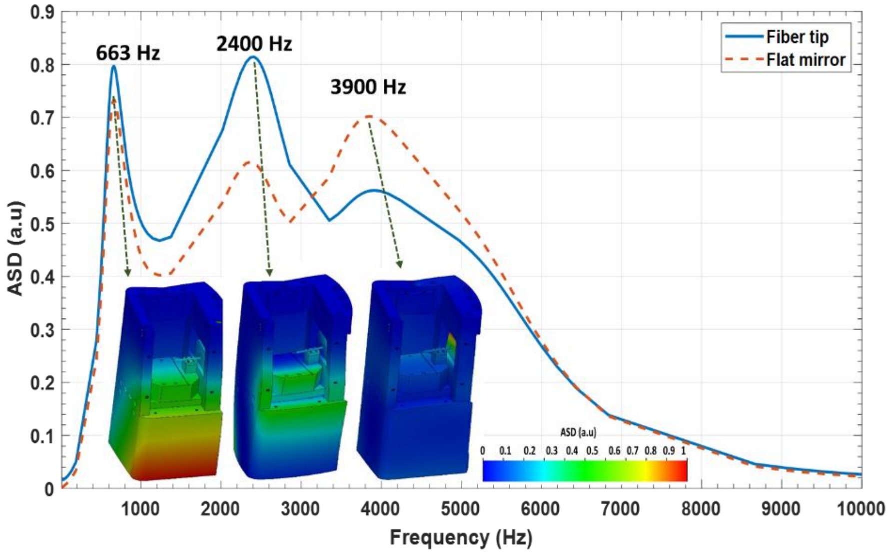

Figure 5.6: Simulation of the assembly frequency response at the fiber mirror tip and the flat mirror. The insets show the ASD of the assembly response at different resonant frequencies. The simulation is performed by linear dynamic simulation tool in Solidworks.

becomes small compared to $m\frac{d^2x}{dt^2}$. In this case, we expect a relatively smaller amplitude of oscillation than for the above case. A problem that occurred in the lab was that the compressor that pumps helium into the cold head generated a roughly 47 Hz vibration of the 1.5 K cell, and we could use this principle to suppress noise at that frequency.

5.6 Assembly frequency response

When we measure the total vibrations on our assembly later, the peaks will come from different sources. Here, we simulate the mechanical response from the assembly alone, which will help us distinguish this from external sources of vibration later. The cavity frequency response is estimated using Solidworks linear dynamic analyses. The program determines the model's response by adding up the contributions of each mode to the loading environment. In this study, the load is applied to the top of the assembly with constant amplitude and a frequency range between 0 and 10 kHz. In most cases, only the lower modes have a substantial role in the response as shown in Fig. 5.6.

A mode's contribution is determined by the load's frequency, size, direction, duration, and position. In Fig. 5.6, the frequency response amplitudes on the fiber tip and the mirror show resonant frequencies at 663 Hz, 2400 Hz, and 3900 Hz, reflecting high rigidity with less susceptibility to low frequencies. The first two resonance frequencies are within the range of the closed-loop circuit bandwidth used for active stabilization; therefore, it is suppressed by about two orders of magnitudes, as shown in the next chapter. The component at 3900 Hz is not so far from the closed-loop bandwidth, so it could be suppressed by using components with a higher stabilization bandwidth. These high frequencies are also expected to be decoupled by hanging the assembly by compression springs as discussed in previous section. The next chapter will detail the experiments conducted with this new assembly setup, focusing on performance at both room temperature and cryogenic conditions. It will also explore various stabilization techniques necessary to attain the high level of stability required for the detection of single rare-earth ion.

6 Micro-cavity length stabilization

This chapter covers the experimental findings obtained from the microcavity assembly described in the previous chapter. It includes the construction of the cavity and the modeling of the mirror coatings. We outline the operational principles of the doubly resonant microcavity and how we utilized it to measure the quality factor, finesse and the cavity length. Furthermore, we analyze the stability of the cavity based on a closed-loop circuit model, presenting data on cavity length fluctuations across various higher-order modes, which is also the topic of Paper I. In this chapter we experimentally demonstrate the capacity of using higher order modes as locking beam to mitigates the impact on fluorescence detection setup. We address the design's performance limitations and propose suggestions for improvement. In addition, this chapter focuses on measurements conducted within a closed-cycle cryostat, discussing the noise generated by the pulse tube cryocooler, its interaction with the microcavity, and measurements taken at a temperature of 10 K. The final section evaluates the stability performance we achieved in comparison to other open access microcavity configurations.

6.1 Cavity Assembly setup

6.1.1 Cavity building

A photograph of the open microcavity is shown in Fig. 6.1a. It includes a flat mirror and a fiber-based concave mirror for the resonator. Three Attocube piezos are used for fine tuning: two ANSx150 piezos for Z and X control, and one ANSz100 for Y control. Coarse tuning is done with translation stages and micro-adjustment screws (see Section 5.5.2 for more details). A fully tunable lens with a numerical aperture (NA) of 0.6 is used for collimation and matching cavity modes, while a shear piezo is used for scanning and stabilization. At room temperature, the shear piezo has a scan range of 3 μm. At 1 K, the scan range is reduced by approximately a factor of 3.

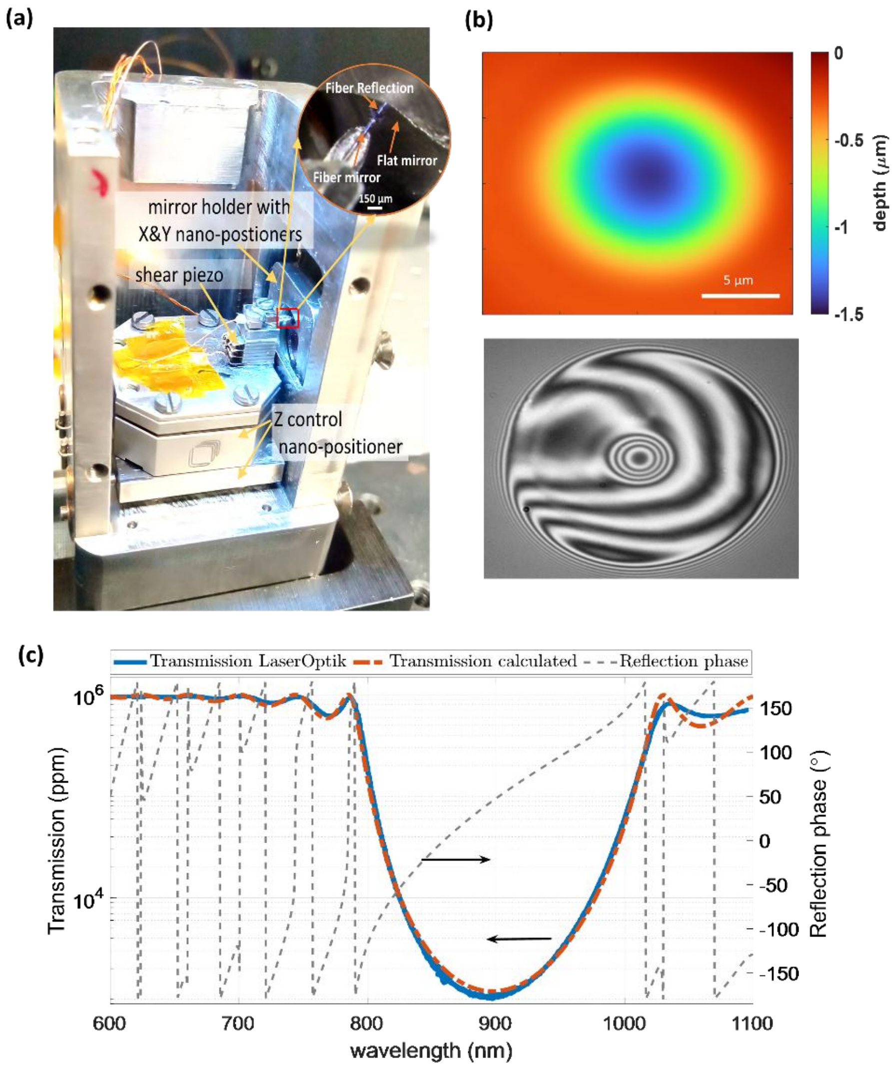

Figure 6.1: (a) A photograph of the constructed cavity assembly and (b) Profile of the fiber mirror end facet surface, measured using a white light interferometer giving a fiber mirror depth of about 1.5 µm. (c) Mirrors transmission measured by LaserOptik (blue line) and simulated (red dash) using the transfer matrix method (described in Section 4.2.1), and the simulated reflection phase of the cavity mirrors (gray dash). The cavity mirrors have 1×10^3 ppm transmission at 892 nm (probe beam) with a reflection phase of +40° and 2×10^3 ppm transmission at 935 nm (lock beam) with a reflection phase of + 80°. The phase undergoes a significant change at the edges of the stop band due to the transmissivity of the stack.

6.1.2 Cavity mirrors and coatings

Figure 6.1b shows the profile of the fiber mirror end facet surface produced by CO_2 laser machining [18], and measured using a white light interferometer. The profile's parabolic fit results in a radius of curvature, ROC = 31 μm, and a mirror depth of about $z_t = 1.6$ μm. The mirror parameters yield a cut-off radius of 10 μm resulting in a cavity mode truncation at the edge of the curvature (see Section 4.4) and to ensure resonator stability, the physical cavity length L should be between 2 and 30 μm.

In this thesis project co-dopants of Nd and Pr impeded in nanoparticles are used as a redout ion and qubit ions, respectively (see Section 7.1). Since Nd is the main candidate for the readout ion, Purcell enhancement should be optimized for its transition wavelength of 892 nm. For qubit ions (Pr), no enhancement is needed as long as a single pass of the beam provides an adequate Rabi frequency for rapid gate operations. Any resonant effect on the qubit wavelength would require a doubly resonant cavity which has no guaranteed alignment. Thus, the high-reflective coatings were engineered to be entirely transmissive at the qubit wavelength of 619 nm. For 892 nm, two different reflectivity levels were selected, R=99.5% and R=99.9%, which correspond to a cavity finesse of approximately 600 and 3000, respectively. The measurements discussed in this thesis are based on using a mirror reflectivity of R=99.9%. The mirror coatings have 12 layers of Ta_2O_5 and SiO_2, with refractive indices of 1.46 and 2.09. They feature a stopband at 892 nm and an AR coating at 619 nm. As discussed in Section 4.2.1, a top layer of SiO_2 was made roughly ~ $\lambda/4$ thick to assure that the samples are placed at the field maximum, thus increasing the sample interaction with the cavity field.

The mirror parameters are utilized to model the transmission characteristics of the coatings and the reflection phase through the transfer matrix method, as shown in Fig. 6.1c. The reflection phase of the cavity mirrors defines the position of the cavity node relative to the nanoparticle for increasing the light matter interaction. A reflection phase of +40° at 892 nm and +80° at 935 nm gives a phase penetration depth of 50 nm and 105 nm, respectively (see Section 4.2.1 for more details). The diode laser operates at a wavelength of 935 nm is employed to maintain the stability of the cavity length throughout the experiments.

6.1.3 Optical setup

Figure 6.2 shows the basic optical setup and a schematic of the electronics used to perform the cavity length stabilization and fluorescence collection experiments. Paper I discusses the setup in detail, but I'll provide an overview below.

The microcavity uses two laser beams, an 892 nm Ti:sapphire laser and a 935 nm diode laser, to probe the spin coated samples on the flat mirror and stabilize the cavity length, respectively. The diode laser beam is coupled to the cavity using a

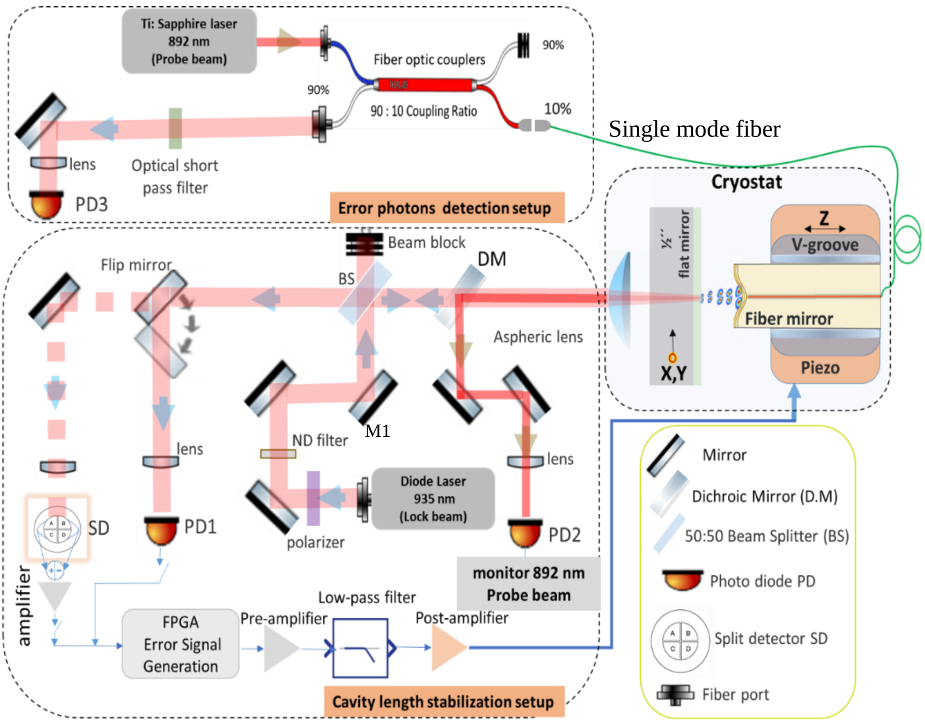

Figure 6.2: The experimental setup includes optical and electrical components, different optical schemes for cavity length stabilization using higher order modes, and error photons detection in a fluorescence setup. This is the same figure as in Paper I, but reproduced here for convenience.

mode-matching lens, while the Ti:sapphire laser probe beam is coupled to the fiber side through a fiber optic coupler's input port (10%). The other fiber port (90%) is used to quantify leak photons transmitted from the single mode fiber (SMF) during stabilization, with measurements recorded on PD3.

A variable neutral density filter (ND) is used to vary the laser power entering the cavity. A dichroic mirror separates the two wavelengths from the cavity, directing the reflected light to photodetectors PD1 and PD2 (DHPCA-100) for analysis. This project implements two cavity length stabilization methods: the tilt locking scheme, which uses a split detector for the locking signal, and the side of fringe scheme, which employs PD1 to generate the locking signal.

6.1.4 Data acquisition

Performing fast measurements is essential for efficient data acquisition, either by averaging the data or by compensating drifts and fluctuations with a quick response.

This is also essential for the scanning cavity microscopy to allow for faster sample imaging and the collection of many rapid measurements. In this respect, a fast field programmable gate array (FPGA) offered by RedPitaya[5] is used for sweeping the cavity length, and as a lockbox for cavity length stabilization. A fast digital oscilloscope[6] is used to acquire cavity signals, and MATLAB is employed to transfer them to the computer and perform data analysis.

6.2 Experimental methods

6.2.1 Using higher order modes for cavity length stabilization

Chapter 4.3simulations reveal that the narrow-band coatings on cavity mirrors enable higher order modes (HOMs) near the fundamental TEM00 mode, which can be used to stabilize the cavity length. Using a fiber for fluorescence detection reduces odd-indexed HOM output coupling by over 100-fold due to the small overlap between the cavity mode and SMF, making HOMs with different wavelengths from the probe beam excellent candidates for cavity length stabilization.

The coupling of HOMs to the cavity involves using the angle of one of the coupling mirrors, M1 in Fig. 6.2, to create misalignment between the lock beam and the cavity axis, enabling higher-order mode coupling. The efficiency of coupling for each higher-order mode is influenced by factors like cavity length, tilt angle, off-axis displacement, and mode-matching aspheric lens alignment, as detailed in the calculations presented in Section 4.5.

Figure 6.3a shows the cavity reflection at 935 nm on detector PD1 and the transmission at 892 nm on detector PD2 when the cavity length is scanned across two free spectral ranges (FSR) and when the lock beam is optimized for a first order mode TEM_{10}. Up to 5 HOMs can be excited in one FSR with different reflection dips due to different coupling efficiencies. A good spatial overlap between the atomic transition at 892 nm and the lock beam at 935 nm is required for cavity length stabilization (see Fig. 6.3). The next section will discuss the conditions and parameters that control the longitudinal overlap between the two wavelengths.

[5] STEMlab 122-16. The device features two 16-bit 50-ohm inputs and 14-bit outputs, and an ultra-low phase noise of 122.88MHz.
[6] LeCroy HDO 6104A,12-bit, 10 GS/s, 1GHz bandwidth.

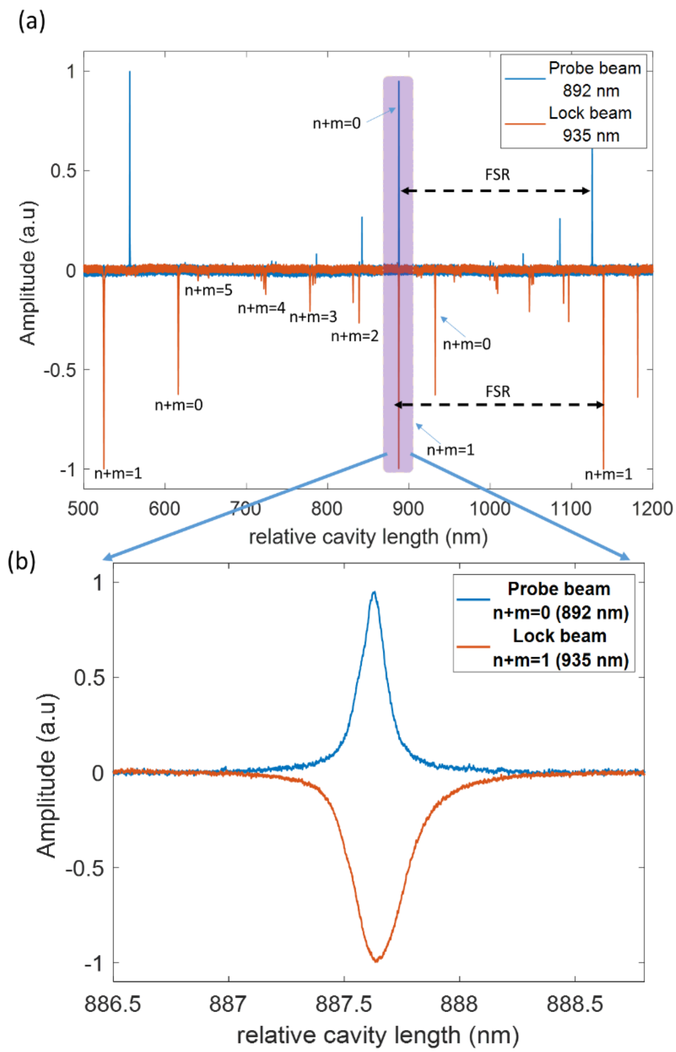

Figure 6.3: (a) Cavity reflection spectrum of the lock beam from the flat mirror side (orange) and probe beam transmission (blue), see Fig. 6.2. The expression (n+m) denotes a collection of resonant modes. (b) The overlap between the transmitted probe beam and the reflected lock beam is shown together.

6.2.2 Doubly-resonant cavity

Equation (4.2) states that a doubly resonant cavity must have a phase shift of 2π for both wavelengths during a single round trip. This can be achieved by considering the fundamental TEM_{00} mode (probe beam) with longitudinal index q_1 for $\nu_1 =$

c/λ_1 and TEM_{mn} mode (lock beam) with q_2 for ν_2. The frequency $\nu_2 = c/\lambda_2$ of the lock beam should satisfy the condition,

$$\nu_2 = \nu_1 + \frac{c}{2\pi L}\left[\pi(q_2 - q_1) - \Delta\varphi + (n+m)\varphi_{Gouy}\right], \qquad (6.1)$$

This equation represents the condition for the overlap between the two standing waves inside the cavity. $\Delta\varphi$ represents the relative phase shifts at the reflection on the cavity mirrors for both wavelengths λ_1 and λ_2. φ_{Gouy} is the Gouy phase shift.

For our experiment, λ_1 is the wavelength of the probe, which is fixed by the atomic transition to 892 nm. The relative reflection phase shift between the two wavelengths can be obtained by the reflection phase simulated by the transfer matrix method (see Fig. 6.1c) giving, $\Delta\varphi = 80° - 40° = 40°$. By applying the values of λ_1 and $\Delta\varphi$ to Eq. (6.1), it becomes possible to derive the optimal conditions. Figure 6.4(a) shows the resonant wavelength λ_2 of the locking beam, corresponding to the condition where the cavity is simultaneously resonant at λ_1= 892 nm and expressed as a function of the cavity length L for different resonant cavity TEM_{mn} modes. The optimal condition for achieving double resonances, is constrained by the tunability range of the diode laser employed as a locking beam, giving $q_1 = q_2 + 1$ in our case. The tunability range of the lock beam is plotted in the inset of Fig. 6.4a as a green rectangle. The wavelength of the diode laser is controlled by adjusting the current or the temperature. To observe the cavity resonances, we measure the cavity transmission and reflection signals while scanning the cavity length with a shear piezo (P-121.03T).

Starting with a long cavity length of approximately 15 µm between the fiber mirror and the flat mirror, the cavity length is progressively moved closer to the flat mirror using the ANSx150 piezo. At every step, λ_2 is tuned so that both wavelengths are resonant with the cavity length. In order to know λ_2, we measure the transmission from the fiber using a spectrometer. We repeat this procedure for different HOMs at various cavity lengths. An example of a doubly resonant cavity is shown in Fig.6.3, when the cavity is turned to be resonant with both the TEM_{10} lock beam and the TEM_{00} probe beam. The inset of Fig.6.4a compare the calculated and the measured overlap for different HOMs and the measured values are plotted as blue circles.

6.2.3 Measuring cavity parameters

Different methods can be employed to assess cavity parameters. One approach to determine finesse involves sweeping the cavity length using the shear piezo element over one free spectral range (FSR). Finesse is defined as the ratio of the FSR to the full width at half maximum (FWHM) linewidth, making this a straightforward technique. However, this method has limitations regarding precision, primarily due to mechanical fluctuations and the non-linear behavior of piezo elements. Additionally, it enables the measurement of finesse without requiring knowledge of the cavity length.

Another method is to use an electro-optic modulator (EOM) to add sidebands at a specific frequency separation with respect to the laser, which subsequently serves as frequency markers. Given the cavity parameters we are considering, the cavity demonstrates a linewidth of $\kappa/2\pi = 17$ GHz ($\kappa/2\pi = \frac{c}{2L\mathcal{F}}$) for L = 3 μm and $\mathcal{F}$ = 3000. Therefore, a modulation frequency exceeding 20 GHz is necessary, otherwise the sidebands will overlap with the carrier, rendering the extraction of the linewidth impossible. For a common modulation of 2 GHz at a wavelength of 780 nm, the measurable finesse is consequently restricted to >10,000 [65].

In this section, we present an alternative approach for assessing cavity parameters through the use of a doubly resonant cavity. This method serves as a tool for the simultaneous measurement of various cavity parameters, such as the quality factor, cavity finesse, mode order, and cavity length. The cavity parameters can be determined by measuring transmission and reflection signals at two resonant wavelengths under length change for calibrations, as illustrated in Figs. 6.4b and 6.4c. Each wavelength can serve as a reference for the other, provided that the previously established condition for overlap is met. The Lorentzian fitting method allows for the determination of FWHM linewidth of a mode in relation to changes in cavity length δd and wavelength $\delta\lambda$. By incorporating the known wavelengths $\lambda_{1,2}$ of the resonant modes, it is possible to estimate the cavity quality factor Q utilizing Eq. (4.2.2).

The mode order of a specific resonant wavelength can be determined by utilizing the fact that the ratio of the measured δd to $\delta\lambda$ linewidths is $q/2$. Additionally, the overlap condition $q_1 = q_2 + 1$ can assist in estimating the mode order of the corresponding mode. The finesse of a mode can therefore be determined by dividing the quality factor by the mode order q, while the cavity length is determined by multiplying the free spectral range of a mode by its corresponding mode order, $L_{1,2} = q_{1,2}\,(\lambda_{1,2}/2)$.

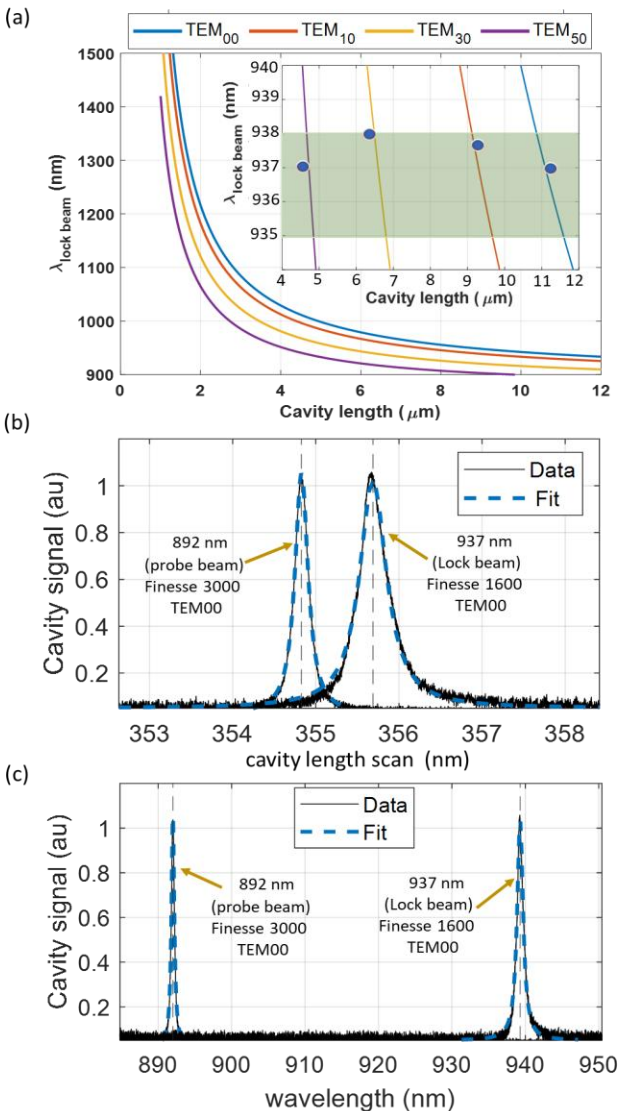

Figure 6.4: (a) Illustrates the theoretical curves given by Eq. (6.1) for different resonant cavity modes. The inset highlights the tunable range of the locking diode laser (indicated by the rectangle) alongside the measured cavity length (represented by the blue circles). The signals from the probe and lock beams with Lorentzian fittings are illustrated in parts (b) and (c), with the x-axis calibrated in terms of cavity length change units and wavelength, respectively, for measuring of both cavity length and finesse.

In Figs. 6.4b and 6.4c, the fitting results indicate $\delta d_{1,2} = 0.15$ nm, and 0.26 nm, along with $\delta\lambda_{1,2} = 0.012$ nm, and 0.021 nm for the probe beam at 892 nm and the lock beam[7] at 935 nm, respectively. The calculated quality factors are $Q_{1,2} = 7.4 \times 10^4$ and 3.5×10^4, while the mode orders are $q_{1,2} = 25$, and 24. The finesse values, $\mathcal{F}_{1,2} \approx 3 \times 10^3$, and 1.6×10^3 can be obtained by dividing the quality factor by the respective mode order. The final parameter is the cavity length, $L_{1,2} = L$ approximately equal to 11.25 µm regardless of if the 892 nm or 935 nm data is used. It is important to note that the precision of these values is determined by the accuracy of the wavelength measurements, which is generally very high. For the different HOMs these measurements are repeated and for the lock beam we observed a maximum finesse of 1600 for TEM_{00} and TEM_{10}, 800 for TEM_{30}, and 400 for TEM_{50} at cavity lengths shown in the inset of Fig. 6.4a. The discussion regarding finesse-dependent HOMs is presented in Section 4.4. As outlined in that section, the finite dimensions of the fiber-based mirror introduce clipping losses to the higher order cavity mode, limiting the finesse. The precision of these measurements is contingent upon the correct values of wavelengths, mechanical fluctuations and the hysteresis associated with the sweeping shear piezo.

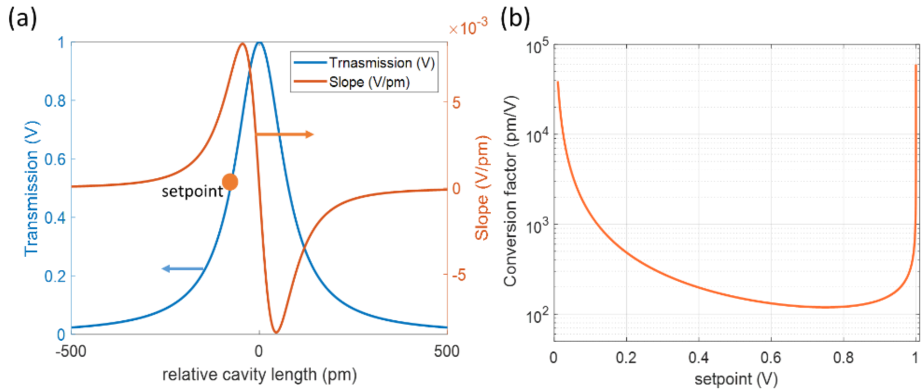

Figure 6.5: (a) The cavity transmission (blue line) under cavity length variation for a finesse of 3000 at 892 nm, and a peak photodiode signal of 1 V. The set point (bright orange) corresponds to the locking point on the transmission side of the fringe where the locking can be performed. The slope given by the derivative of the transmission signal (dark orange). (b) The conversion factor across different voltage levels. It is determined by inverting the slope (dark orange (a)) and interpolating the relevant values at distinct setpoints (bright orange point).

[7] The signal reflected at 935 nm is inverted to allow for a direct comparison of FWHM linewidths of two different wavelengths.

6.2.4 Conversion factor

To ensure optimal mechanical stability during operation, it is essential that the variations in cavity length are significantly smaller than the linewidth of the cavity resonances, expressed as $\delta d = \frac{\lambda/2}{\mathcal{F}}$ [65]. Here, δd is the FWHM linewidth under length change measured via the finesse. In Fig. 6.5a, a transmission signal measured in volts on the oscilloscope, corresponding to variations in cavity length, is shown. The FWHM linewidth of the transmission signal at 3000 Finesse is δd = 148 pm. Figure 6.5b illustrates a derived conversion factor in units of pm/V, as a function of the setpoint (lock point) on the flank. The conversion factor is utilized for converting the measured voltage fluctuations into position fluctuations.

6.3 Locking schemes

It is essential to maintain a constant cavity length, since this determines the resonance frequencies of the cavity, thereby influencing spectral characteristics, such as the transmission spectrum and the lifetime of the emitters contained within. For a given cavity, this can be improved by implementing active stabilization, which effectively suppress any vibrations that could disrupt the system. The first step of the locking procedure involves creating an electronic error signal, which can be used for the locking of the cavity. In this research project, both side-of-fringe locking and tilt locking techniques have been utilized to produce the error signal necessary for actively preserving the stability of the cavity, while assessing their performance across various parameters.

The following sections will outline the methods employed for generating the error signal, which can then be corrected for by the piezo positioners.

6.3.1 Pound-Drever-Hall (PDH)

The PDH scheme [72, 73] employs frequency-modulated light that interacts with the incoming light within the cavity, leading to the production of an error signal. This method relies on breaking the symmetry of the fringe around resonance, which causes the error signal to exhibit odd symmetry about the line center, thereby facilitating locking to the peak of a cavity fringe. The short cavity length leads to a broad spectral width, despite the high finesse, requiring high modulation frequencies to effectively modulate error signals (see section 6.2.3). For the sake of simplicity and to avoid increased expenses, which would arise from the need for high-frequency electronics and electronic optical modulators (EOMs), PDH cavity locking has not been implemented.

6.3.2 Side-of-fringe

The side-of-fringe locking technique employs the slope on either side of the cavity resonance, whether in transmission or reflection, to transform fluctuations in cavity length into corresponding amplitude changes. Locking to the peak of the transmitted signal, as shown in Fig. 6.5a, does not yield any information regarding the sign of the cavity length deviation, which is why side of the fringe locking must be used. A similar argument is true if the reflected signal is used instead. As shown in Fig. 6.5a, the reference lock point is given by a set voltage which defines a specific cavity length compared to the photodetector voltage in reflection. This method has the immediate advantages of great simplicity and even versatility, as a lock point can be chosen at an arbitrary cavity length along the flank. Despite its advantages, side-of-fringe locking has considerable downsides.

The main concerns include the slope of the error signal, which itself depends on the finesse and contrast of the cavity signal near resonance. In addition, side-of-fringe is susceptible to fluctuations in laser power, which can directly introduce noise into the piezo elements used for length fluctuations compensations.

6.3.3 Tilt locking

The tilt locking scheme shown in Fig. 6.6, utilizes the phase of an off-resonant mode as a stable reference beam [74, 75]. This reference can be used to compare with the phase of a beam resonant with the cavity, to extract the length fluctuations. In this research project, we suggest the first-order mode as the cavity resonance mode, which ensures minimal coupling with the single-mode fiber (SMF) (see Chapter 4), while the locking laser's TEM_{00} mode serves as the off-resonant phase reference.

The study uses a split detector (First Sensor QP5.6-TO5) to break the symmetry of the fringe around the line center, resulting in a nearly linear phase response. The tilt error signal is derived from a difference between the two halves. A silicon quadrant photodiode is used for tilt locking analysis, connected to a micrometre stage for adjustable xyz axes. The mathematical derivations of the tilt error signal are presented in [76].

The problem with the tilt locking scheme is the high sensitivity of the lock signal to the beam positioning on the split photodiodes, so secure photodiode mounting and avoiding optical components before the split photodiode are crucial to avoid beam displacement.

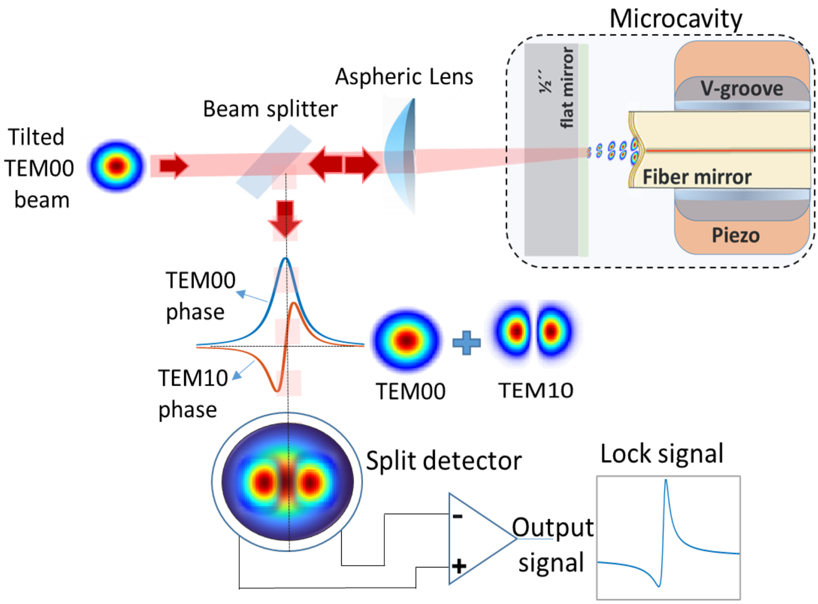

Figure 6.6: Tilt locking detection scheme. When a tilted beam is coupled into the cavity from the flat mirror side, it excites the TEM_{10} mode, whereas the symmetric TEM_{00} mode is directly reflected because it resonates at a different cavity length. A vertically split detector can be utilized to measure the spatial phase gradient that arises from the interference of the two modes. By subtracting the signals from the two halves, a lock signal is generated.

6.4 Feedback locking circuit analysis

When the cavity length is stabilized at a lock point, even minor fluctuations of the cavity length can lead to an error signal, which is measured by photo detector PD2 or split detector SD in Fig. 6.2. To maintain the system's output at the lock point, a feedback control loop is required. This control loop consists of several components, such as a FPGA for proportional-integral (PI) controller, a low-noise pre-amplifier (SRS, Model SR 560), a first-order RC low-pass filter, a post-amplifier (TD250), and finally the shear piezo (P-121.03T) to actuate the compensation. The feedback/control design to make a stabilization cavity is illustrated in Fig. (6.7).

The system's closed-loop transfer function, where $s = 2i\pi f$, is denoted as [77],

$$\mathrm{H(s)} = \frac{C_S(s)\, H_A(s)\, H_{PI}(s)}{1+C_S(s)\, H_A(s)\, H_{PI}(s)} \qquad (6.2)$$

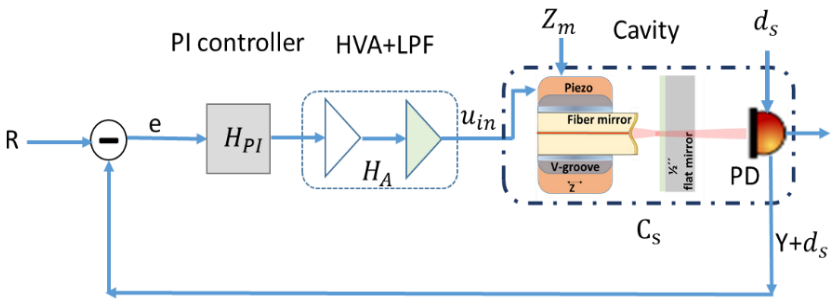

Figure 6.7: Block diagram of the feedback control system showing the control input R, Z_m perturbations, and photo diode noise d_s. The physical system is represented by C_s , the amplifier with low-pass filter LPF by H_A, the control algorithm by H_{PI}, and photo detector PD (which measures the cavity's output).

The forward gain (open-loop gain) from setpoint R(s) to detector output Y(s) is represented by the numerator $C_s(s)\ H_A(s)\ H_{PI}(s)$, whereas the denominator is one plus the gain, referred to as loop gain. The transfer function $H_A(s)$ of the amplifier with LPF is given as $H_A(s) = A_u/(1 + \tau\ s)$, A_u is the gain of the amplifier and $\tau = 0.6436/2\pi BW$ is the low pass filter time constant and BW represents its bandwidth. The transfer function of the PI controller is defined as, $H_{PI}(s) = K_p + K_I/s$, where K_p is the proportional gain and K_I is the integration gain. The function $C_s(s)$ determines the combined gain of the cavity and photodiode and can be given as,

$$C_s(s) = K\ G_s(s), \tag{6.3}$$

The transfer function $G_s(s)$ represents the perturbation in the intracavity field due to the cavity length fluctuation [78-80]. On the reflection side and for a symmetric cavity, $G_s(s)$ can be rewritten as [80],

$$G_s(s) = -\mathrm{ik}\left(\frac{\lambda}{2\mathcal{F}}\right)\frac{\mathcal{R}\, e^{-i\beta}}{(1-\mathcal{R}\, e^{-i2\beta})};\ \beta = \mathrm{s} \times \frac{\mathrm{L}}{\mathrm{c}}. \tag{6.4}$$

Here, $\mathrm{k} = 2\pi/\lambda$ is the wavenumber, λ is locking wavelength, $\mathcal{F}$ is the cavity finesse, $\mathcal{R}$ is the cavity mirrors reflectivity, L is the cavity length, and c is the speed of light. The parameter K in Eq. (6.3) specifies the gain factor of the photodetector for the signal reflected from the cavity and is given by [77],

$$\mathrm{K} = \eta\ P_{\mathrm{r}} G\ \Re\, r_{piezo}/\delta d\ , \tag{6.5}$$

where η is the coupling efficiency to the cavity mode, P_r is the reflected power from the cavity on the detector with transimpedance gain of G (V/A), $\Re$ (A/W) is the photodiode responsivity, $r_{piezo}/\delta d$ is the ratio between the piezoelectric coefficient r_{piezo}(nm/V) and the cavity resonance linewidth $\delta d = (\lambda/2\mathcal{F})$.

6.4.1 Circuit performance

The closed loop transfer function given by Eq. (6.2) shows that the performance of the feedback circuit depends on the circuit gain, closed-loop circuit bandwidth, and the slope of the cavity signal, which is a function of the cavity finesse. In addition, the electronic noise from the amplifiers, drivers and the shot noise of the detector can limit the performance. One of the key parameters is the closed loop bandwidth, which evaluates the efficiency of a locking circuit by defining the frequency range in which the condition $C_s H_A\, H_{PI} > 1$, and thus the extent to which the environmental noise can be effectively suppressed.

6.4.2 Noise suppression using feedback circuit

The output Y(s) of the feedback circuit can be expressed, as derived in the supplementary material of paper I, by taking into account a potential disturbance of the cavity (see Fig. 6.7) caused by Z_m, along with the photodiode noise d_s,

$$Y(s) = \mathrm{H(s)}\,[R(s) - d_s(s)] + \frac{1}{1+C_s(s)\,H_A(s)\,H_{PI}(s)}\,Z_m. \qquad (6.6)$$

This demonstrates that, if the open loop gain is large enough, perturbations Z_m impacting the system may be effectively minimized. In contrast, noise that enters through the PI controller from the photo detector cannot be suppressed as discussed later. The error signal of the feedback loop is given as,

$$\mathrm{e(s)} = \mathrm{R(s)} - Y(s). \qquad (6.7)$$

Using Eq. (6.6), the error signal, when affected by Z_m and d_s, can be given by,

$$\mathrm{e(s)} = \left[\frac{\mathrm{R(s)} - Z_m}{1+C_s(s)\,H_A(s)\,H_{PI}(s)}\right] + \mathrm{H(s)}d_s(s). \qquad (6.8)$$

When $C_s(s)\,H_A(s)\,H_{PI}(s)$, is significantly greater than 1, the first term of Eq. (6.8) diminishes considerably and $\mathrm{H(s)} \approx 1$. Consequently, the error signal is primarily influenced by the detector noise and additional electronic noise introduced into the closed loop by the amplifiers and the PI controller, allowing for an approximation as follows,

$$\mathrm{e(s)} \approx d_s(s). \qquad (6.9)$$

As a result, the photo detector PD should have a low noise level compared to the cavity perturbations to allow them to dominate the signal.

In the side-of-fringe locking measurements the cavity signals are focused on a photodiode (Hamamatsu, S5973) connected to a transimpedance FEMTO amplifier (DHPCA-100). With no light incident, the integrated output peak-to-peak detector noise V_{pp} is 36 mV at 10^8 V/A transimpedance gain (G) and 220 kHz bandwidth (BW). We can then calculate the limit where the shot noise from the useful signal is dominating over the detector noise as [81],

$$\mathrm{P_r} = \frac{{V_{pp}}^2}{2\, G^2\, \Re\, q\, BW}, \tag{6.10}$$

where q is the electronic charge. For the photodiode detector with responsivity $\Re$ = 0.26 A/W at the 935 nm lock beam wavelength, and 220 kHz bandwidth, the power P_r that would be necessary for the shot noise of the beam to exceed the detector noise is 7 µW. This power P_0 is equivalent to 4 mW intracavity power at 1600 finesse. The quadrant split detector for tilt locking error signal generation has a minimum detectable power of 12 pW per element, but noise from the reverse-biased circuit and operational amplifier increases this power limit.

6.4.3 Noise amplitude analysis

The noise amplitude spectral density (ASD) can be given as,

$$S\left(\frac{pm}{\sqrt{Hz}}\right) = \frac{|e(s)|}{\sqrt{2\Delta f ENBW}}. \tag{6.11}$$

ENBW=1.5 indicates the equivalent noise power bandwidth, while Δf denotes the frequency interval. The root mean square (rms) length fluctuation, measured in picometers (pm), can be determined by integrating the amplitude spectral density across the frequency bandwidth as follows:

$$\Delta L_{rms}(pm) = \left(\int \left[S\left(\frac{pm}{\sqrt{Hz}}\right)\right]^2 df\right)^{0.5} \tag{6.12}$$

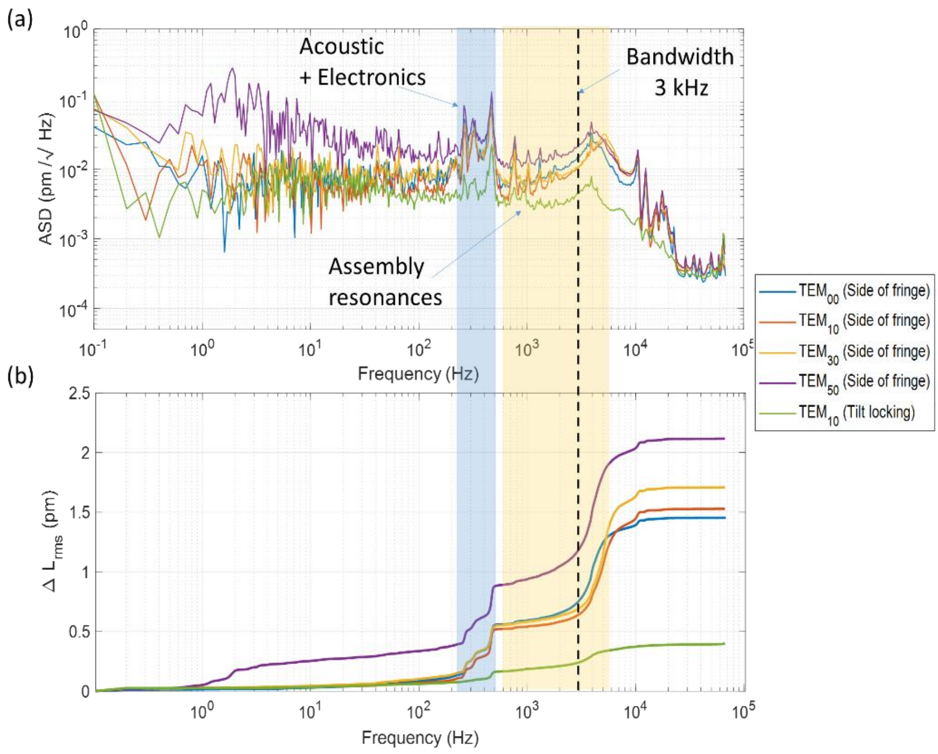

Figure 6.8: Room temperature stability measurements. (a) Shows the amplitude spectral density (ASD) at different TEM_{mn} modes. (b) The cumulated rms length fluctuation obtained by using the analysis performed in Section 6.4.3 at 32 mW intracavity locking power and 237 μW intracavity power for probing beam.

The rms amplitude is used for evaluating the performance of the cavity setup under various perturbations, as well as assist in further improvements during cavity building and operation in noisy environments.

6.5 Evaluating circuit performance at room temperature

This section aims to characterize the cavity assembly's locking performance, using side-of-fringe and tilt locking schemes. We present our results for the closed-loop measurements, where we investigate the stability across multiple higher-order modes and intracavity locking powers to attain an optimal balance between high mechanical stability and low photon leakage in fluorescence detection via the single-mode fiber (SMF).

Figure 6.8 illustrates the stability measurements of the cavity at room temperature while it is positioned on the air dumper optical table. The locking circuit bandwidth is 3 kHz, limited by the post amplifier. Measurements are done using a 892 nm probe beam with a cavity finesse of 3000, allowing comparisons of different modes and input powers. Peaks around 260-500 Hz are due to acoustic and electronic noises. Assembly resonances range from 0.6 kHz to 5 kHz as described in Section 5.6. Higher-order modes have worse locking due to the reduced finesse and therefore have larger length fluctuations, but that the locking can be improved by using fiber mirrors with a larger cut-off radius in future setups. Breaking the symmetry of the cavity fringe is a significant distinction between tilt locking methods and the side of the fringe, resulting in a steeper slope around the line center. This adjustment facilitates locking at the peak of a cavity fringe when using the tilt locking method. A threefold increase in stability is demonstrated in Fig. 6.8b, reaching around 0.5 pm rms, while maintaining the same intracavity power when contrasted with the TEM_{10} side of fringe result of about 1.5 pm rms. This improvement can be attributed to the steeper slope observed.

6.5.1 Noise analysis

In our locking circuit, the minimum length fluctuations achieved with a feedback loop operating at a 3 kHz bandwidth are 0.5 pm, as determined by the tilt locking method. This performance is constrained by the closed-loop bandwidth. To enhance technical performance, we can transition to a high-voltage amplifier, such as the ADHV4702-1, which is designed to operate over a wide bandwidth while ensuring a low noise profile. By utilizing this amplifier, approximately 150 fm rms can be attained when the closed-loop bandwidth is increased to 80 kHz as given in Paper I, which is nearly aligned with the fast-lock shear piezo bandwidth of 84 kHz.

Thermal fluctuations represent a significant factor that may restrict overall performance. Figure 6.9 illustrates the thermal noise generated by light absorption in mirror coatings and substrates, which leads to variations in the refractive index of the coating layers and substrate linked to both cavity length (thickness-related) and beam size (area-related) elastic deformations [82]. These fluctuations subsequently initiate photothermal phenomena [82, 83], including photo-thermal elasticity (PTE) and photo-thermal refraction (PTR). Furthermore, Brownian noise is associated with the random motion in the coating materials and substrate. The total amplitude spectral density (ASD) of the thermal length fluctuations S can then be written as [82],

$$S\ (\frac{m^2}{Hz}) = s_{PTR}^{coa} + s_{PTE}^{coa} + s_{Brown}^{coa} + s_{PTE}^{sub} + s_{Brown}^{sub}. \tag{6.13}$$

The integrated noise over all frequency range gives about 115 fm rms at 1 W intracavity power. The calculated shift in cavity resonance for our specific cavity

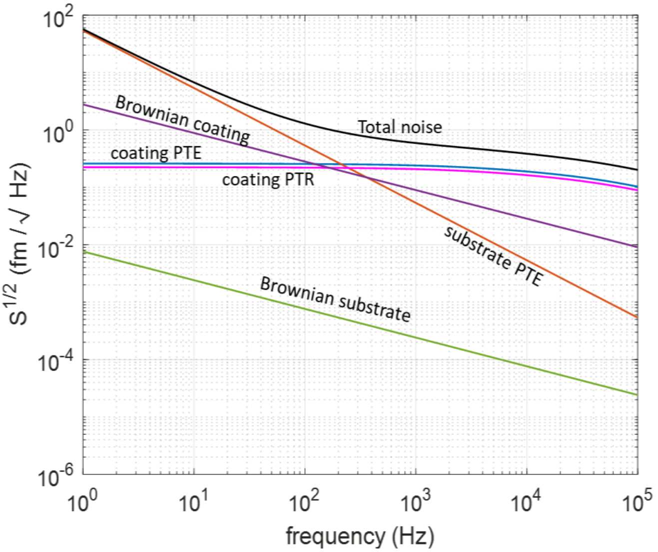

Figure 6.9: Thermal length fluctuation within the microcavity mirrors of coatings Ta_2O_5/SiO_2 as a function of frequency, including photo-thermal elasticity (PTE), photo-thermal refraction (PTR), and Brownian thermal noise. The calculation is performed at 1 W intracavity power, 3µm cavity length, 100 ppm mirror coating absorption, and 20 ppm substrate absorption at 935 nm.

parameters and mirror coating material (Ta_2O_5/SiO_2) is 0.22 linewidths per watt of intracavity power, as determined by Eq. (28) in [18]. The thermal noise predictably diminishes as the intracavity power decreases, ultimately nearing the Brownian noise threshold of 15 fm rms at an intracavity power of 32 mW in our setup.

6.6 Error photon suppression

In addition to the stability performance, using higher order modes also brings a benefit to fluorescence measurements conducted in the stabilized cavity, which we now discuss. Figure 6.10 shows the measured error photons that are coupled to the single-mode fiber from the odd-indexed higher order modes locking beam, across different intracavity power levels.

The light transmitted through the single-mode fiber during cavity length stabilization is captured by the transimpedance photodetector PD3 (see error photon detection configuration in Fig. 6.2), which generates an output signal measured in volts from which the photon count per second can be calculated. The fundamental mode, TEM_{00}, exhibits a significantly higher error photon rate compared to the higher-order modes, due to overlap between the cavity mode and the single mode fiber. When intracavity power decreases, the error photons approach the noise threshold of the detector, rendering them undetectable by the standard detector. A fitting procedure has been applied to the data presented in Fig. 6.10, where the photon rate transmitted from the fiber mirror through the cavity to the detector is described by the equation,

$$J_{out} = T\frac{P_c\eta}{E}. \tag{6.14}$$

where $P_c = P_{in}T(\mathcal{F}/\pi)^2$ is the intracavity power, P_{in} is the incident power, $\mathcal{F}$ is the cavity mode finesse, E is the energy of the single photon, η is the total probability to detect each emitted photon, and T is the transmission through the symmetric cavity mirrors.

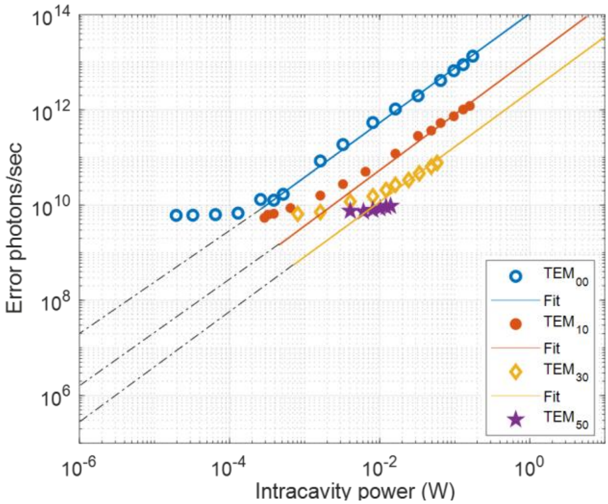

Figure 6.10.: Shows the leakage of error photons through the single-mode fiber mirror when the cavity is stabilized at various higher-order modes (HOMs). The error photon rate is recorded by PD3 (see to Fig 6.2) across different HOMs, with power levels normalized to intracavity power for each mode. The lower plateau indicates the detection limit of the photodiode; however, the results demonstrate that employing locking powers down to 10^{-4} W, which facilitate effective stabilization (as described in Paper I), results in a suppression of error photons by approximately two orders of magnitude when higher-order modes are utilized.

The mode coupling to the fiber is a component of the total probability $\eta = \eta_c\, \eta_{setup}\, \eta_{SMF}\, \eta_d$, where η_c is the mode coupling to the cavity, $\eta_d = 0.26$, is the detector quantum efficiency, $\eta_{setup} = 0.22$ is the optical setup detection efficiency. The fitting yields the values of η_{SMF} for TEM_{00}, TEM_{10}, and TEM_{30} as 0.24, 0.03, and 0.012, respectively. Using larger cut-off radius mirrors could lead to even greater suppression of error photons since it allows for coupling higher odd order modes.

6.7 Stability in a closed-cycle cryostat

The stabilization measurements discussed in the previous sections are performed at room temperature when the cavity assembly is clamped to an optical table resting on air dampers. However, the cavity assembly is required to attain a base temperature of less than 2 K while providing a cooling power of no less than 10 mW [15] to maintain the long coherence times of the rare-earth ions. To accomplish this, the closed-cycle cryostat described in Section 2.2 is employed. Figure 6.11a shows the inner gas cell with the top flange used to hang the cavity assembly described in Fig. 6.11b.

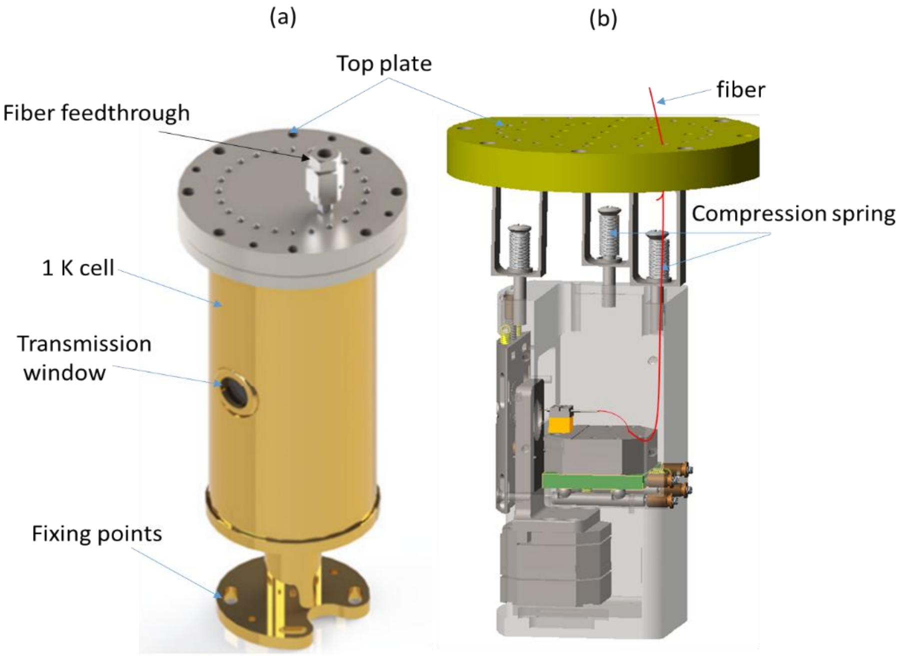

Figure 6.11: (a) The inner gas cell with the top flange on which the cavity assembly is mounted. (b) Finished cavity assembly hanging from the top plate of the inner 1K cell of the cryostat, where one side has been rendered to be transparent.

6.7.1 Pulse tube cryocooler noises

Pulse tube (PT) cryocoolers work by using the principle of compressing and expanding a gas in a sealed space to remove the heat from the working gas [84]. Because of the oscillatory response, which is required for cooling down the gas cell, mechanical noises can be induced by the high-pressure signal from the compressor and the cooling cycle. Thus, the operation of stable open-access microcavities presents a significant challenge due to vibrations induced by PT cryocoolers, which can impact the functionality of these cavities.

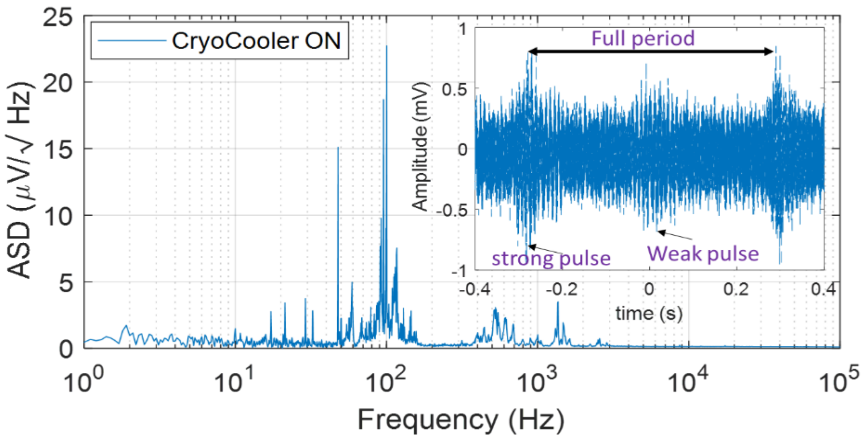

Figure 6.12: Amplitude spectral density of the signal from the time trace (inset) obtained by an accelerometer mounted on the gas cell when the cryocooler is operated at room temperature.

To initiate our investigation into operations within such noisy environments, we conducted measurements and analyses of the vibration noise produced by the pulse tube (PT) cryocooler, utilizing an amplified accelerometer. The fast Fourier transform of the time trace recorded by the accelerometer while it is attached to the gas cell with the PT cryocooler ON, is illustrated in Fig. 6.12. The time traces (inset) show a strong and a weak pulse, both with a period of 0.6 s (1.7 Hz) separated by 0.26 s. A variety of resonance peaks appears between 10 Hz-2500 Hz, with a maximum peak at 47.6 Hz and 100 Hz. The peak at 47.6 Hz corresponds to an oscillatory high-pressure signal from the compressor and the peak at 100 Hz is probably from the pulse tube cryocooler cycle [85].

6.7.2 Microcavity performance in closed-cycle cryostat

The assembly hangs by three compression springs (see Fig. 6.11b), each with a spring constant of 220 N/m, designed to suppress the resonance frequency of the assembly at 47.6 Hz coming from the compressor that pumps the helium gas into

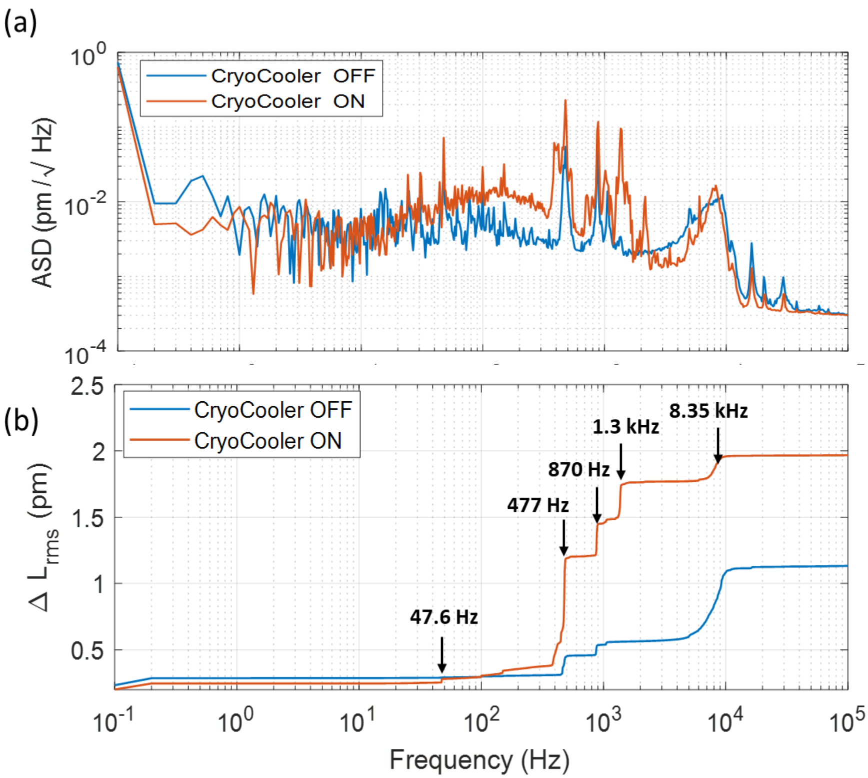

Figure 6.13: Room temperature stability measurements of the microcavity hanging from the ceiling of a cryostat inner cell top plate using side of fringe locking scheme. This includes (a) the vibration spectrum recorded with the cryocooler both activated and deactivated, and (b) the cumulative root mean square length fluctuations associated with the corresponding resonance frequency.

the cold head. As discussed in Section 5.5.3, the assembly noise suppression is dependent on the total number of active turns of the springs. The springs are adjusted to reduce 47.6 Hz because the microcavity was less affected by other higher frequency components, as measured by the accelerometer in the previous section.

Figure 6.13 shows measurements performed with the optical setup described in Section 6.2, when the microcavity assembly was operated in the cryostat under vacuum at room temperature with both cryocooler off (blue curve) and cryocooler on (red curve).

The cumulative length fluctuations in Fig 6.13b indicates that the microcavity was slightly more stable at higher frequencies when the assembly was hanging in the cryostat with the cryocooler turned off, compared to when the microcavity assembly was placed on the optical table, as illustrated in Fig.6.8. As previously mentioned in Section 6.5, the mechanical noise of the cavity length fluctuations is dominated by

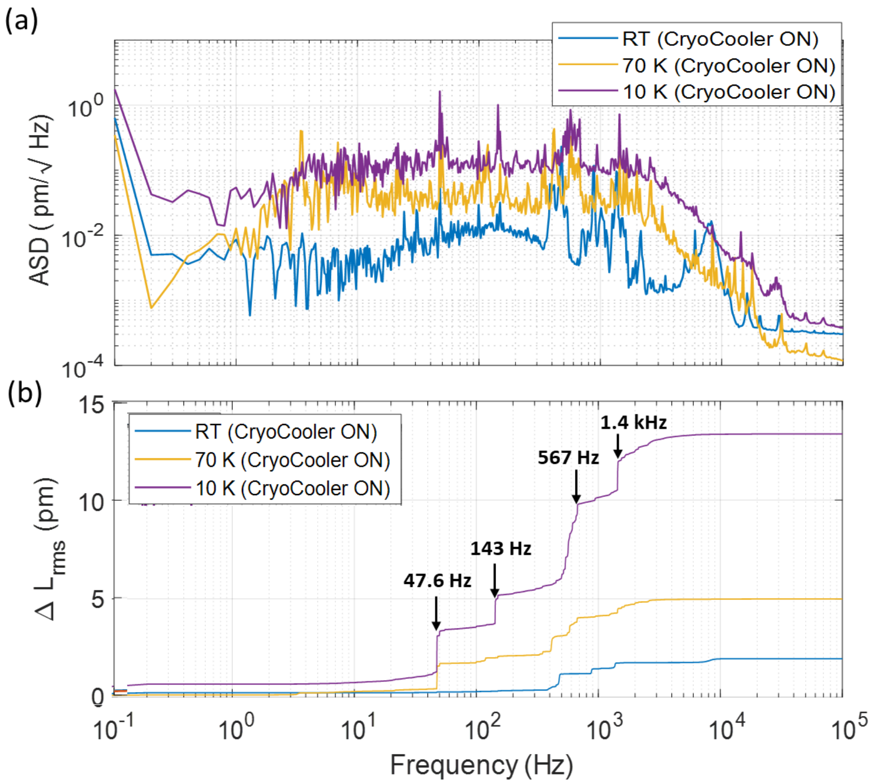

Figure 6.14: Stability measurements of a microcavity hanging from the ceiling of a cryostat cell top plate recorded with the cryocooler activated using side of fringe locking scheme. This includes (a) the vibration spectrum at room temperature and 70 K and 10 K, and (b) the cumulative root mean square (RMS) length fluctuations associated with the corresponding resonance frequency at the same temperatures.

acoustic noise, along with electronic noise that is coupled into the positioning piezo elements. When the assembly is suspended from the 1.5 K gas cell, it functions as an acoustic isolator, significantly reducing the amount of acoustic noise picked up by the cavity assembly. The cryocooler leads to noise excitation, particularly at the natural frequencies of the assembly between 0.6 kHz to 3 kHz. Figure 6.13 shows that the peaks at 477 Hz, 870 Hz, 1.3 kHz, and 8.35 kHz are present even when the cryocooler is off, indicating these frequencies are not generated by the cryocooler but are enhanced by its activation.

Figure 6.14 illustrates the performance of the cavity at cryogenic temperatures alongside its performance at room temperature for comparison. At 10 K, we observe increased rms fluctuations by about an order of magnitude compared to the room temperature measurements. A shift and change in the resonance frequencies while cooling down was observed at 567 Hz and 1.4 kHz and this might be due to the system being stiffer at cold temperatures. Strong peaks were observed at 47.65 Hz and 143 Hz, which originates from the compressor and the pulse tube cryocooler cycle as defined by the manufacture at low temperatures. The presence of three degrees of freedom in the spring systems allows for various tuning options to suppress multiple frequency components. This capability can be utilized to mitigate the peaks at 47.6 Hz and 143 Hz, thereby enhancing the overall stability of the system at 10 K.

At 10 K, the root mean square fluctuations could also be reduced to around 2 pm if the fiber tip is in direct contact with a flat mirror. However, this setup might limit the range of cavity length adjustments, which is necessary for using higher orders for stabilization. Moreover, direct contact risks scratching the fiber coatings, and nanoparticles may adhere to the fiber tip, leading to a loss of finesse, as seen in our experiments.

In conclusion, a root mean square length fluctuation of 15 pm has been attained at a finesse of 3000 and a temperature of 10 K through the implementation of side fringe locking. It is anticipated that a stability of approximately 5 pm rms can be realized by employing a tilt locking scheme. These measurements indicate that single ion detection is feasible with the existing cavity.

6.8 How does the stability compare to other fiber cavity setups?

The old slipstick attocube positioner-based setup achieved passive stability of about 500 picometers (pm) rms at low temperatures, improving to around 300 pm with a fast lock obtained at room temperature. High stability configurations have been reported in helium bath [25, 86] and closed-cycle cryostats [87, 88], demonstrating their effectiveness for precise measurements. Recent developments have led to systems with spatial tunability and passive stability of tens of picometers in closed-cycle cryostats, achieving 2 to 20 pm rms through active stabilization [25, 56, 77, 86-89].

The stability can be improved further in systems with limited scanning capabilities, particularly those that can only be adjusted along the cavity length. Gallego et al. achieved a stability of 0.24 pm in a piezo-actuated fiber-fiber cavity using a 3 kHz Pound-Drever-Hall (PDH) locking method [90]. Brachmann et al. attained a remarkable stability of 110 femtometers (fm) with a fiber linked to a shear piezo and a gimbal-mounted mirror, employing a 1.1 kHz PDH lock and photothermal stabilization at 500 kHz [83], effectively combining various stabilization techniques for ultra-high precision.

The conclusion is that the proposed configuration demonstrates comparable or better stability compared to systems with the same scanning capabilities. In addition, the assembly design with a high number of degrees of freedom ensures stability if the mechanical and electronic components are well optimized while simultaneously allowing flexibility for sample materials and wavelengths.

7 Neodymium as a readout ion

The main scheme for realizing a rare-earth quantum computer uses a dedicated readout ion that can sense the state of nearby qubit ions via e.g., dipole interactions as discussed in Section 2.1.5. This means that a state-selective excitation of the qubit can cause the fluorescence of the readout ion to be switched off or remain, allowing the qubit state to be readout [91–95].

In this chapter we examine the desired properties of materials that can be good readout ions, and present experimental results. Section 7.2 details the spectroscopic characteristics of Nd^{3+} co-doped Pr^{3+} in Y_2O_3 crystal, as analyzed in Paper II. Section 7.3 discuss the Nd^{3+} as a potential redout ion. Section 7.4 details the experiments performed with the microcavity under both room temperature and cryogenic conditions of 2.1 K. It covers the application of scanning cavity microscopy for identifying nanoparticles, presents fluorescence measurements, and includes a discussion on estimating the number of excited ions as well as the effects of power broadening.

7.1 Single-readout ion and qubit ion requirements

For the readout scheme outlined in Section 2.1.5 to function effectively, specific criteria must be satisfied by both the readout ion and the qubit ion. Long optical and hyperfine coherence periods are essential for the qubit ion in order to preserve the quantum state. In this context, Eu^{3+} is a highly interesting choice with an optical coherence time of 2.6 ms [97] and a ground hyperfine coherence time that, in a Y_2SiO_5 host, can reach several hours [46]. Another interesting possibility that has been the focus of a lot of study (also this study) is Pr^{3+}, which was used in the first spin qubit gate demonstration [11]. Pr^{3+} exhibits a hyperfine coherence time of 42 s [98] and an optical coherence time of 152 μs [99] within the Y_2SiO_5 host. Eu and Pr are potential qubit ions but not readout ions due to their weak fluorescence and low branching ratio to the ground state. Despite potential use of cavity enhancement, the readout photon rate is still somewhat limited.

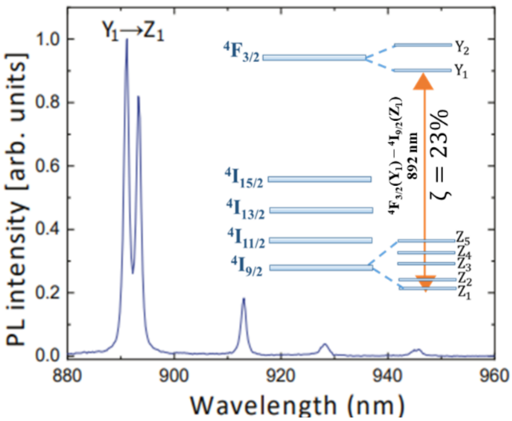

Figure 7.1.: The photoluminescence (PL) spectrum of co-doped Nd^{3+} nanoparticles in Y_2O_3 at 10 K was recorded using 813 nm excitation. The inset illustrates the energy level diagram featuring the relevant transition $^4F_{3/2}(Y_1)$ to $^4I_{9/2}(Z_1)$ at a wavelength of 892 nm, which has a branching ratio of 23% utilized in these experiments. The five peaks shown in the figure correspond to decays to the five possible Kramers doublets (Z_1-Z_5) of the $^4I_{9/2}$. These results are discussed further in Paper II.

The readout ion requires a short-excited state lifetime and high fluorescence yield to achieve efficient readout of the qubit state. A narrow homogeneous linewidth is essential; the narrower the linewidth, the smaller the interaction shift caused by dipole-dipole interactions needed for the qubit ion to effectively impact the readout. This allows the interaction to shift the resonance frequency of the readout ion by a few homogeneous linewidths, off-resonance with the driving field. One of the primary advantages of utilizing Nd as a readout ion is its notable branching ratio to the ground state. The transition of the readout ion must be cycled to yield high fluorescence, avoiding long-lived trapping energy levels [96]. Spectral overlaps between the qubit ion and the readout ion must also be avoided to prevent fluorescence yield reduction and perturb the qubit state if the emission of the readout ion is absorbed [15].

This study examines Nd^{3+} ions in Y_2O_3 nanocrystals, which are integrated with a microcavity to shorten the excited state lifetime, positioning them as a potential readout ion. Nd is particularly noteworthy due to its significant transition dipole moment associated with 4f transitions. Furthermore, it exhibits a high branching ratio to the ground state, approximately 23%, and a favorable long wavelength at 892 nm. The next section will address the Nd^{3+} spectroscopic properties.

7.2 Spectroscopic properties of Nd^{3+} doped Y_2O_3

The purpose of these early measurements was to determine if Nd had sufficiently favorable properties in terms of lifetime, coherence time and branching ratio. Two samples of Nd^{3+}: Y_2O_3 were examined in this study, which were prepared by Professor Philippe Goldner at CNRS in Paris. The first sample consisted of Y_2O_3 ceramic infused with Nd^{3+} ions at a concentration of 100 ppm. The second sample comprised Y_2O_3 nanocrystals with an average diameter of 380 nm that were co-doped with Nd^{3+} and Pr^{3+} ions at concentrations of 100 ppm and 500 ppm, respectively. Nd was co-doped with a high concentration Pr to allow strong coupling strengths between the inter-species. Additionally, a third nanocrystal sample, featuring an average diameter of 180 nm at concentrations of 100 ppm, was analyzed in cavity experiments (Section 7.4.2).

Figure 7.1 shows the fluorescence spectrum of the $^4F_{3/2}(Y_1) - {}^4I_{9/2}(Z_1)$ transition, with five peaks corresponding to possible Kramers doublets (Z_1-Z_5) of the $^4I_{9/2}$. The ratio of emission into the transition $^4F_{3/2}(Y_1) - {}^4I_{9/2}(Z_1)$ was measured to be about 23% compared to the emission into all other transitions, including the other 4I Stark levels. This is one of the highest branching ratios of rare-earths and it allows a higher likelihood of photon emission into the cavity mode.

The spectroscopic characterization of Nd^{3+}: Y_2O_3 was carried out using a CW Ti:sapphire laser at 892.16 nm, a double pass AOM for pulse shaping, and a copper holder with a pinhole for sample fixation inside a bath cryostat at 2.15 K. The nanocrystal powder was contained in a custom-made holder where the thickness of the powder layer was ~500 μm. A lens was mounted to collimate the fluorescence signal, which was focused onto an APD. A 900 nm long-pass filter was inserted to filter out excitation light, allowing detection of emission to the higher I-states. Further information about the experimental setup is available in Paper II.

7.2.1 A non-transparent ceramic

The sample was a non-transparent ceramic of micron-sized Y_2O_3 crystallites, pressed and doped with 100 ppm of Nd for characterization. The fluorescence signal revealed an excited state lifetime of about 350 μs measured by a pulse excitation of the transition $^4I_{9/2}(Z_1) - {}^4F_{3/2}(Y_1)$ followed by detection time, and an inhomogeneous line of about 5 GHz was obtained by scanning the excitation wavelength while detecting fluorescence at $\lambda > 900\ nm$.

7.2.2 Nanocrystals in powder

The fluorescence lifetime of Nd nanocrystal powder with an average diameter of 380 nm was measured in a similar way as follows ceramic, and found to be about

540 μs, i.e., significantly longer than for the ceramics. This can be explained by the fact that the loose powder has plenty of empty space around emitting ions, which leads to lower effective refractive index and to weaker emission modes. Previous studies indicate that Y_2O_3 nanocrystals in a PMMA layer (refractive index ~1.5) reduced the lifetime of Eu^{3+} ions [100, 101]. This might explain why the ceramic sample has a shorter lifetime than nanocrystals, as the change in refractive index around the ions in the ceramic is smaller than that in nanocrystals.

An inhomogeneous line of about 8.2 GHz was obtained. The broadening in the line compared to ceramic can be attributed to the high content of Pr^{3+}which was doped at concentration of 500 ppm [13,102,103].

To assess the coherence time, a photon echo sequence was utilized [15]. The pulse sequence for measuring homogeneous linewidths begins with a $\pi/2$ pulse that excites ions into a superposition state. Due to the inhomogeneous broadening among the ions, they start to dephase. After a time, interval τ, a second π pulse is applied, which reverses the dephasing, enabling the ions to re-establish their phase after an additional time τ following the second pulse. The in-phase atoms then emit a coherent photon echo, which has a quadratic relationship with the number of atoms. A coherence time of 5.14 μs was measured at a temperature of 1.6 K, corresponding to a homogeneous linewidth of 62 kHz using Eq. (2.3).

7.3 Readout fidelity estimations

The readout scheme outlined in Section 2.1.5 necessitates a high detection rate (decay rate of the readout ion × optical collection efficiency) for effective differentiation between the qubit states. For the Nd readout ion, which has a lifetime of 540 μs, a Purcell factor of approximately 5000 is necessary to reduce the readout ion's lifetime by approximately 100 ns. This reduction enables multiple cycles during the Pr qubit excitation period, considering $T_{1,Pr} = 140\,\mu\text{s}$ [104]. The decreased lifetime of the readout ion results in a detection rate of 1 MHz, calculated from a decay rate of 10 MHz (1/100 ns) multiplied by an optical efficiency of 10%. This is based on a fiber-based microcavity that achieves an overall optical efficiency of 10%, which encompasses an 80% detector efficiency, a 25% coupling efficiency from the cavity mode to the fiber, and about 50% optics efficiency. Notably, this detection rate is an order of magnitude lower than the estimated frequency shift[8] of approximately 10 MHz between a Nd^{3+} ion and a Pr^{3+} ion when they are separated by roughly 5 nm [105]. This difference between the frequency shift (10 MHz) and

[8] For two Pr^{3+} ions 5 nm apart, a frequency shift of about 10 MHz is expected, which roughly estimates the shift between a Nd^{3+} ion and a Pr^{3+} ion.

the detection rate of the readout ion (~1 MHz) is essential for effectively distinguishing between qubit states.

When employing Pr^{3+} as the qubit ion, which has an excited state lifetime of 140 µs [104], the readout fidelity reaches 94% after 10 µs (see Paper II), as determined by Bayesian analysis [92] that utilizes photons detected from the readout ion to infer the state of the qubit ion. Conversely, using Eu^{3+} with a 2 ms lifetime [46] improve the fidelity to approximately 99% over the same time of 10 µs. This fidelity is limited by the finite lifetime of the qubit ion, which may result in a loss of state information due to spontaneous decay during the detection process. Buffer ion can improve Eu^{3+} fidelity to 99.9% [9], but increases detection time to 40 µs. This fidelity is primarily limited by decay during the transfer pulse between the qubit and the buffer ion.

7.4 Scanning Cavity Microscopy

Scanning Cavity Microscopy uses optical cavities to improve imaging of nanoscale objects enabling light to interact multiple times, which in turn enables high-resolution images [22,106]. In this thesis work, this is accomplished by systematically scanning a plane mirror that holds the samples relative to a fiber mirror. By assessing the power levels both in the presence and absence of the particle, one can infer the extinction cross section, which represents the quantity of light removed from a beam due to the particle's scattering and absorption effects.

7.4.1 Sample preparations

The particles used here are Y_2O_3 nanocrystal samples co-doped with 100-ppm of Nd^{3+} and Pr^{3+}, with a mean diameter of 180 nm. To bring the sample to the mirror surface without contamination or aggregation, a pipette is utilized to prepare a mixture of a very low concentration of nanoparticles and a high-purity ethanol solution (99.9%). The sample within the pipette is then subjected to ultrasonic treatment for three hours to disintegrate any aggregates. Following this, approximately 100 µl of the processed solution is drawn into a clean syringe and deposited onto the slowly rotating mirror of the spin coater. After 30 seconds, allowing sufficient particles to settle on the mirror surface, the rotation speed is increased to 2500 rpm. The spin coating process may need to be repeated multiple times to achieve the desired particle density.

The nanocrystals should be small to avoid high scattering loss in the cavity, but still large enough to preserve desirable coherence characteristics. Additionally, they should form sufficiently large ensembles to facilitate identification with the scattering loss microscopy method mention above, and to address the limitations associated with the scanning range of positioners.

7.4.2 Identification of Nd^{3+} nanoparticles

The cavity is used to identify nanocrystals for fluorescence measurements by scanning the flat mirror relative to the fiber mirror, as illustrated in Fig. 7. 2a. The extra loss caused by particles (B) is connected to the cavity's peak transmission (T_p), providing valuable insights into particle distribution through the relation [106],

$$T_p = \epsilon \frac{4T_1\, T_2}{(L_c+2B)^2} \tag{7.1}$$

The equation relates the peak transmission of the cavity T_p, with the coupling efficiency between cavity and fiber modes ϵ, and cavity mirror transmissions $T_{1,2}$. The parameter $L_c = T_1 + T_2 + 2(A + S)$, defines the total loss from the empty cavity mirrors. This loss is due to the mirror transmission, which is equal for both mirrors at $T = 10^3$ppm, along with absorption around A=40 ppm and the mirror roughness (0.2 nm rms) which induces scattering loss of about S=8 ppm. The loss from particles can also influence the finesse of the cavity by relation,

$$\mathcal{F} \approx \frac{2\pi}{(L_c+2B)} \tag{7.2}$$

Equation (7.1) simplifies the process of finding the absolute value of extinction from a nanocrystal by normalizing it to the transmission of an empty cavity ($B=0$), $T_{c,0} = \epsilon\, 4\mathrm{T}_1\, \mathrm{T}_2/L_c^2$. The normalized peak transmission amplitude of the cavity relates directly to the loss B by the nanoparticles inside the cavity through the relation [106],

$$B = \frac{L_c}{2}\left(\sqrt{\frac{T_{c,0}}{T_p}} - 1\right) \tag{7.3}$$

The extinction C_{ext} can be expressed in relation to the measured losses B and the cavity mode waist w_0 by the relation [106],

$$C_{ext} = \frac{\pi\, w_0^2}{4} B, \tag{7.4}$$

Assuming very small absorption form the particle, the volume of the nanocrystal (V) is related to the scattering extinction coefficient C_{ext} through the crystal's polarizability (α) by the following equation [106]:

$$C_{ext} = \left(\frac{2\pi}{\lambda}\right)^4 \frac{\alpha^2}{6\pi\epsilon_0^2}, \tag{7.5}$$

where ϵ_0 is the dielectric constant of vacuum. The polarizability can be expressed in terms of the refractive indices of the nanoparticle n_p and the surrounding medium n_m by relation [106],

$$\alpha = 3\epsilon_0 V \frac{n_c^2 - n_m^2}{n_c^2 + 2n_m^2}, \tag{7.6}$$

Notably, the scattering loss introduced by a spherical nanoparticle, scale with its radius to the sixth power as, $C_{ext} \propto |\alpha|^2 \propto V^2 \propto r^6$.

7.5 Room temperature measurements

As measurements inside a cooled cryostat may present its own challenges, we started testing the scattering imaging technique and fluorescence measurements in a room temperature setting.

7.5.1 Extinction measurements

Figure 7.2 presents experimental data on nanoparticles obtained through cavity transmission within a scanning area of roughly 25 µm × 25 µm. Cavity losses from particle scattering provide insights into nanoparticle distribution and size, as indicated by changes in cavity peak transmission (Eqs. 7.2 - 7.6). The resolution limit of the cavity setup is determined by analyzing the transmission loss in relation to the identical scan size of the empty mirror. In our case, the resolution is limited to a particle radius of

73 nm with a standard deviation of 6 nm, which is lower than the mean radius of 90 nm, reported by the crystal growers.

Figure 7.2d presents a density histogram illustrating the distribution of particles. The distribution function, derived from a Gaussian size distribution, shows a particle radius of 95 nm with a standard deviation of 5 nm, which aligns with the expected value, indicating that the scattering formalism effectively accounts for observed losses. From a quantum computing perspective, accurately measuring the diameter of each particle based on the observed scattering losses, $(C_{ext})_{NP} \alpha\, r^6$ in a scanning cavity image, enables the precise spatial identification of high-quality samples exhibiting a small scattering which is one component that is needed to have a high enhancement. This approach also facilitates the accurate calculation of the number of excited ions. Limiting factors include scattering loss and absorption from the mirror, which constrain the resolution of the smallest detectable particles. In this instance, the mirror roughness (~8ppm) imposes a limitation of approximately 73 nm in radius, as previously discussed.

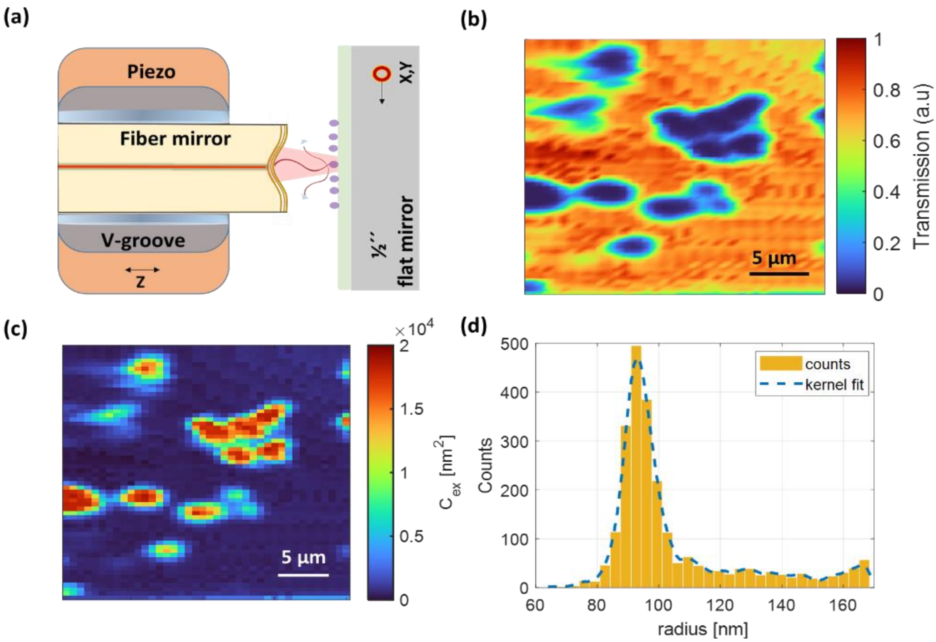

Figure 7.2: Scanning cavity microscopy. (a) illustration of the cavity used for sample identification using the scattering loss from the particles spin coated on the flat mirror. Arrows denote the light scattering from the nanoparticle. The V-groove is a titanium component utilized for fixing the fiber mirror. (b) shows map of an area with size of about 25 µm× 25 µm of the normalized cavity transmission in the presence of the particles. (c) the extinction cross section of the nanoparticles obtained by Eq. (7.2) for a 1.4 µm beam waist. Note that the visible sizes of the particles are in some cases limited by this beam waist. (d) histogram of the particle size with fitting to extract the radius.

It is important to highlight nanoparticles possess a high surface area, resulting in a significantly greater number of surface atoms compared to their bulk. Small particles tend to cluster or agglomerate due to Van der Waals force attraction. Consequently, careful sample preparation is crucial, and extended ultrasonic treatment can help reduce agglomeration.

7.5.2 Fluorescence detection

Once the nanocrystals have been identified, a pulse sequence is initiated with the active locking on. The fluorescence detection experiments outlined in this section employ an experimental configuration that uses higher-order modes for stabilizing cavity length, as detailed in Chapter 6. A diode laser at 935 nm serves as a continuous locking beam, while a 892 nm laser is used for excitation in pulse mode. The detection scheme uses three acousto-optic modulators (AOMs) controlled by an arbitrary wave generator[9] (AWG) and a digital delay generator[10] to effectively shape and manage pulses, preventing excitation light from reaching and saturating the single-photon avalanche detector (SPAD). The photon counting SPAD is gated such that it only detects photons while the excitation light is off. For additional information on the detection scheme, see [15]. Furthermore, prior to the SPAD, three short pass filters are employed to mitigate the error photons from the stabilizing beam at 935 nm during the detection period. These filters exhibit an optical density of 4 each at 935 nm locking beam, while maintaining a transmission rate greater than 95% at the detection wavelength.

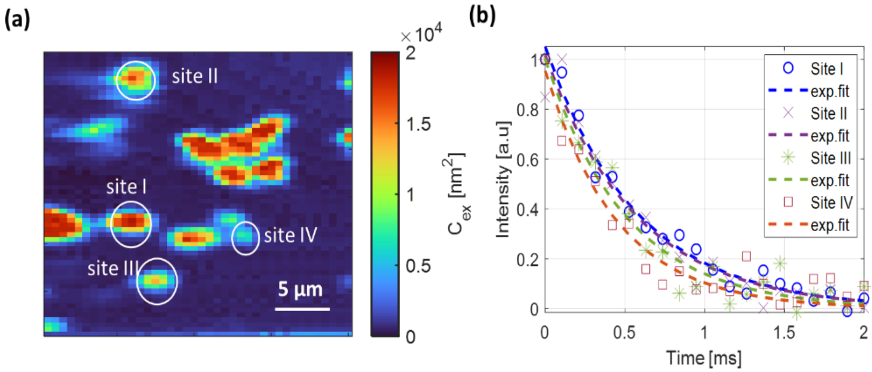

Figure 7.3.: Room temperature fluorescence measurements. (a) shows a scanning cavity microscopy image of the same 25 µm × 25 µm area as Fig 7.2. The scan shows different particles (whites circles) with different extinction losses. (b) shows the binned fluorescence counts at the different sites identified in (a), captured over a duration of 2 ms following 100 µs excitation, from a total of 30,000 individual shots. The lifetime measurements recorded are 571 µs for site I, 570 µs for site II, 507 µs for site III, and 450 µs for site IV.

Figure 7.3 shows the room temperature fluorescence measurements of the $^4I_{9/4}$ − $^4F_{3/2}$ transition line of Nd^{3+} conducted at various nanoparticle locations, exhibiting different extinction losses. Ions are excited using a 100 µs pulse, while the cavity is continuously stabilized to the TEM_{30} mode, giving a low coupling to the single mode fiber of $\eta_{30} \approx 0.01$. Before bringing the samples onto the mirror, a finesse of 3000 is measured at 892 nm for an empty cavity. For the measurements shown in Fig. 7.3, the cavity length was adjusted to 3.5 µm across all measurement locations, tuned to allow a double resonance of the locking and probing beam, as explained in Section 6.2.2. The transmission loss due to particle size cause the observed finesse values to vary by site (white circles): 1100 at site I, 1400 at site II, 1800 at site III, and 2200 at site IV. Accurately assessing nanocrystal size is crucial for calculating

[9] Agilent N8241A.

[10] Stanford Research DG535

excited ions as discussed later. Estimated radii at site I, II, III, and IV are 119, 111, 100, and 92 nm, derived from observed finesse using Eqs. (7.2 - 7.5). Together with the doping concentration, this allows us to estimate the number of ions contained in each single crystal. With 100 ppm Nd^{3+} doping concentrations, the estimated number of Nd^{3+} ions in a single crystal are 1.8×10^4, 1.5×10^4, 1.1×10^4, and 8.5×10^3 ions, respectively.

Figure 7.3b shows fluorescence decay detected on the SPAD over a period of 2 ms after excitation and accumulated from 3×10^4 shots. The obtained traces were well fitted by an exponential decay and the resulting decay constants equal to the lifetime, 571 μs for site I, 570 μs for site II, 507 μs for site III, and 450 μs for site IV.

These results show lifetime shortening to some extent due to Purcell enhancement, especially at higher finesse. Theoretically, with a finesse of 3000 the maximum Purcell enhancement is $F_{\mathrm{eff}} = \zeta \times 65 = 15$, considering transition branching ratio of 23% using Eq. (3.22). However, this is limited by the ion linewidths at room temperature. The cavity exhibits a narrow linewidth $\kappa = 17$ GHz ($\kappa = \frac{c}{2L} \times \frac{1}{\mathcal{F}}$). On the other hand, at room temperature, the 892 nm transition has a broad homogeneous linewidth[11] of $\Gamma_h = 452$ GHz, which leads to the bad emitter regime [106]. In this regime the effective Purcell factor reduces according to $PF_{\mathrm{eff}} \propto \kappa/\Gamma_h = 0.04$, resulting in the enhancement of only a limited portion of the ion's emission width. In contrast, at lower temperatures, the linewidth of the ions narrows to ~100 kHz, which is considerably less than that of the cavity. This allows us to effectively amplify the entire spectrum of the ions.

7.6 Cryogenic measurements

This section provides a detailed discussion of the spectroscopy measurements conducted on the Nd^{3+} nanoparticle at 2.1 K. In this section, we conducted cryogenic measurements utilizing the first-generation assembly microcavity described in Section 5.1. A beam of 892 nm served as an excitation beam. Although the stability of the fringe at low temperatures was suboptimal, it was enhanced by carefully pressing the fiber against the flat mirror once a good nanocrystal was identified. Additionally, the z-attocube was employed to compensate for drift during the measurements (see Section 5.2). Cavity mirrors with transmissions of 1000 ppm and 60 ppm are utilized for these measurements, resulting in a finesse of 6000 at the empty areas of the cavity mirror.

[11] The transition linewidth is $\Delta\lambda = 1.2$ nm which is converted to frequency units by relation: $\Gamma_h = \Delta\lambda \times c / \lambda^2$.

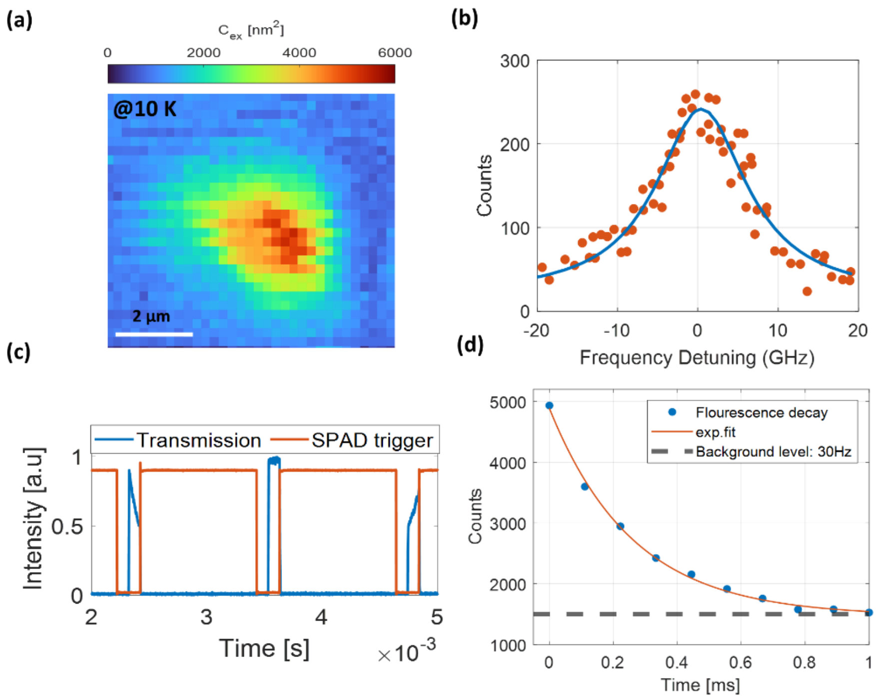

Figure 7.4.: cryogenic measurements. (a) scanning cavity microscopy shows the extinction loss of an isolated nanocrystal with a 105 nm radius with measured at 10 K. (b) measurement of the inhomogeneous line of the $^4F_{3/2}$–$^4I_{9/2}$ transition at 2.17 K. The solid line is a Lorentzian fit, yielding a fullwidth-half-maximum linewidth of 14 GHz. (c) pulse sequence employed for measuring fluorescence, consisting of a 100 µs excitation pulse and a 1 ms detection period. The input signals employed are uniform square pulses; however, the blue trace is not uniform as a result of rms cavity length jitter. (d) binned fluorescence counts (blue) detected during 1 ms after excitation and accumulated from 10^5 shots, and a single exponential fit (red) with a lifetime of 260 µs. The background dark-count level is plotted as dashed grey corresponding to 30 Hz.

In Figure 7.4b, the inhomogeneous linewidth of the transition was measured by collecting the signal for the first 200 µs after the excitation pulse, and accumulating the fluorescence counts from 2×10^4 shots while adjusting the laser wavelength across the inhomogeneous line for the transition.

A Lorentzian fit is applied to the data, revealing a FWHM linewidth of approximately 14 GHz, which is consistent with the linewidth measured in nanocrystals with a diameter of 380 nm, as discussed in Section (7.2.2). The pulse sequence used for excitation and fluorescence collection at cold temperature is shown in Fig.7.4c. A 100 µs pulse is used for excitation $^4I_{9/2}$–$^4F_{3/2}$ transition followed by 1 ms collection time, repeated 5×10^5 times.

Figure 7.4d shows fluorescence decay measurements of Nd^{3+} at 2.1 K with the background level included. The data were fitted with a single exponential, giving a lifetime of 260 µs ± 15 µs. showing a small amount of Purcell enhancement.

7.6.1 Purcell enhancement

The effective Purcell factor (F_{eff}) can be evaluated experimentally by comparing the excited state lifetime within the cavity ($T_{1,c}$) to the lifetime (T_1) without cavity enhancement at room temperature as given by Eq. (3.21). For this measurement, we utilized T_1=570 µs, which represents the maximum lifetime measured at room temperature, suggesting the absence of cavity enhancement (see Section 7.5.2). We measured 260 µs lifetime at 2.1 K for the 892 nm Nd transition. This gives an estimate of a twofold Purcell enhancement, 570 µs /260 µs ~ 2.2.

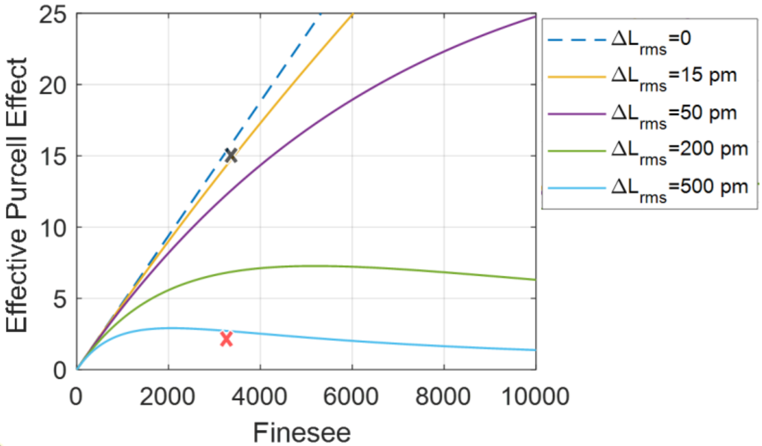

Figure 7.5: The effective Purcell factor F_{eff} in dependence of the cavity finesse. The dashed blue curve is without noise and marks the upper limit [ΔL_{rms}= 0, full term in Eq. (3.19)] whereas the other curves correspond to $\Delta L_{rms} = 15\ pm\ to\ 500\ pm$. Additionally, the result from Fig 7.4(d) is displayed as red cross, and the expected result from the new design is displayed as a black crosse, corresponding to F_{eff}=15).

We can compare the observed value with an estimate of the theoretically effective Purcell factor by utilizing Eq. (3.22), under the assumption of optimal alignment between the dipole and electric field vectors, along with placement at the maximum cavity field. At the transition wavelength of 892 nm, the cavity finesse is measured to be $\mathcal{F}$ = 3400 at the nanoparticle, using a mode volume of $5\lambda^3$. Consequently, the effective Purcell effect is determined to be $F_{eff} = \zeta \times 73 \approx 17$, where ζ represents a branching ratio of 23% for this transition. This is ~ 8 times greater than the measured value of 2.2. This discrepancy can be ascribed to several factors that are not accounted for in the theoretical calculations. The primary reason is the rms cavity length jitter due to the mechanical vibrations, which causes a lower time-averaged Purcell-factor of the system [56, 57]. When the cavity length jitter of 500 pm rms was taken into account using the formula given in [56], the resulting effective Purcell factor became 2.6 (see Fig.7.5), which is in excellent agreement with the measured value.

7.6.2 Excited ions estimations

Nanocrystals with a limited number of ions allow for easier spectral selection of individual ions, which are essential for quantum computing applications. In this section we will estimate the number of excited ions based on the total photon counts number obtained from the fluorescence decay measurements as shown in Fig.7.4d. The number of excited ions can be estimated by [15],

$$No.of\ excited\ ions = \frac{(Counts/No.of\ shots)}{\zeta \times \eta}, \tag{7.7}$$

In this context, ζ indicates the branching ratio, which is measured as 23% for $^4F_{3/2}(Y_1) - {}^4I_{9/2}(Z_1)$ transition at 892 nm, as detailed in Section 7.2. The detection efficiency (η) is calculated to be 1.2%. This accounts for a combination of factors, including 20% optical setup, 40% quantum efficiency of the SPAD, and 15% out-coupling efficiency. The sum of the binned counts shown in Fig. 7.4 (d), after subtracting the dark count, was 9415, based on 5×10^5 shots. If we assume half of the excited ions decayed during the 1 ms detection period, we can apply Eq. (7.7) to approximate the number of ions that contributed to the signal, yielding an estimate of ~ 7 ions. This value can be assessed in relation to the number of targeted ions by utilizing the laser power, as will be elaborated upon in the following section.

7.6.3 Power broadening and targeted ions estimations

In this section, we estimate the number of targeted ions during the measurements based on factors like particle size, doping concentration, and linewidths, along with excitation power.

For the average nanocrystal radius of 100 nm (see Fig. 7.4a), a total of $N\sim 1.1\times10^4$ Nd^{3+} ions are estimated within the crystal of 100 ppm concentration. With a homogeneous linewidth of about $\gamma_h = 62$ kHz spread over an inhomogeous linewidth of $\gamma_{inh} = 14$ GHz, this estimate leads to $n = N\frac{\gamma_h}{\gamma_{inh}} = 0.05$, i.e., the ion transitions are separated by about 21 linewidths (*1/n*), and low power spectroscopy would in most cases address at most a single ion. In this experiment, we use a high excitation power to improve the signal to noise ratio which leads to strong power broadening, and thus off resonant excitation of small ion ensembles (see Section 3.4).

In these experiments, the input to the cavity is approximately 37 nW, which is then amplified by a factor of about ~ $\mathcal{F}$ /π resulting in an intracavity power of 40 μW for $\mathcal{F}$ = 3400, as measured at the 100 nm particle. For the given transition dipole moment, $\mu = 5.48 \times 10^{-32}\mathrm{C.m}$ [15], a corresponding Rabi frequency of Ω_R = 25 MHz can be estimated. The power broadening can be calculated using Eq. (3.24), giving a FWHM broadening of ∼ 36 MHz. This value exceeds the 62 kHz homogeneous linewidth of 380 nm nanocrystals by over two orders of magnitude, as detailed in Section 7.2.2.

With ions spaced by approximately 21 linewidths and an ions density of about 8 × 10^{-4} ions per kHz (N/γ_{inh}), around 28 ions were influenced by the estimated 36 MHz power broadening. In a steady state excitation scenario, only half of the ions would be excited, resulting in approximately 14 ions contributing to the fluorescence measurements. Nevertheless, our focus is on single ion detection, which is essential for quantum computer applications (see Chapter 8). Given the uncertainties in the various estimates, this is in good agreement with the measured value (7 ions). This indicates that at this level of finesse, we are in the few-ions regime. By reducing the power broadening from 36 MHz to 1 MHz, it would be possible to target a single ion, on average. This can be done using < 100 nW intracavity power, provided that the signal to noise ratio can be improved accordingly.

Working with the first-generation cavity assembly at such low power levels, presents challenges due to poor mechanical stability of the earlier design. This instability is estimated to be approximately 500 pm rms length fluctuations at a finesse of 3400, which is about four times the cavity linewidth ($\delta d = \lambda/2\mathcal{F} = 131\ pm$). For a length fluctuation of 15 pm rms, observed at a finesse of 3000 and a temperature of 10 K, using the second generation microcavity assembly (see section 6.7), the effective Purcell factor can be improved by a factor of 7, up to 15, as illustrated in Fig. 7.5 (black cross). This improvement allows for excitation power levels below 100 nW, which minimizes power broadening effects while still achieving a satisfactory signal to noise ratio, thus enabling the detection of individual ions.

8 Quantum Computer requirements and Outlook

In this chapter, we will take a step back to get a broader view of the rare-earth quantum computing (REQC) proposal as we understand it at this point. This analysis is formed by feedback on the challenges encountered and proposed enhancements derived from measurements and calculations on our setup, as outlined in earlier chapters.

I will describe six key components required for REQC: selecting materials with optimal properties, readout mechanisms, single-qubit gates, two-qubit gates, forming a single processor node, and the interconnection of multiple nodes (refer to Fig. 8.1 and see Ref. [9] for more details).

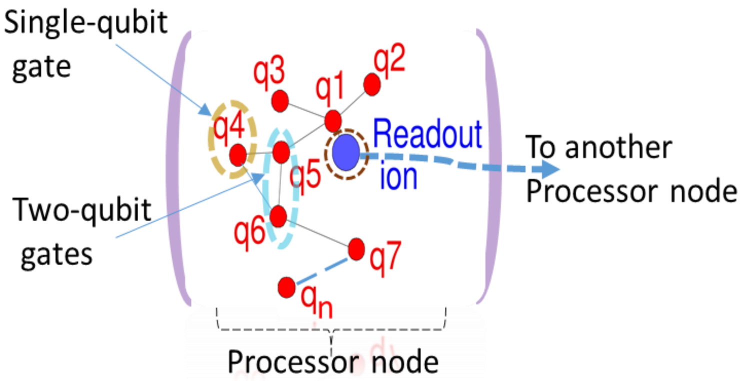

Figure 8.1: REQC building components (See Ref. [9] for more details). The most promising REQC uses single RE ions, with one as a qubit and another for readout. Ion-ion interactions enable two-qubit gates and connect qubits to the readout ion, see the text for more details.

8.1 Materials

The most promising approach to REQC involves using individual rare-earth (RE) ions, where one RE species functions as a qubit while another species enhances emission through a microcavity, facilitating qubit state readout, as outlined in Section 7.1.

For the qubit, europium (Eu) doped into Y_2SiO_5 is recommended due to its long coherence time in both optically excited and spin states, along with a significant separation between optical hyperfine levels, which contributes to improved gate operation performance as discussed later. However, the increased spacing of hyperfine levels may impose limitations on the number of qubits, because a larger frequency interval have to be reserved for each qubit to avoid overlap. Consequently, praseodymium (Pr) emerges as an alternative qubit option, characterized by smaller hyperfine level spacing. This could potentially lead to a substantial increase in the number of qubits within the node by reducing the bandwidth allocated per qubit, although at a cost of having less coherence time.

Neodymium (Nd) is identified as a promising material for the readout ion, as discussed in Chapter 7. It has a short lifetime and high emission rate, attributed to a relatively high oscillator strength. In addition, it has a high branching ratio to the ground state along with a long transition wavelength of 892 nm, giving a relatively low scattering loss when working with nanoparticles, positioning it as an ideal candidate for integration within the cavity.

A large addressable inhomogeneous width is necessary to have many qubits in one processor node (see Fig. 8.1). This can be achieved by high doping concentrations. Only a few readout ions are needed, so trace amounts can be used in a highly doped crystal with Eu. Another concern is the overlap of spectral lines between Stark levels of the readout and qubit ions, which can cause energy transfer. This may lead to loss of coherence in excited qubit ions. These issues mainly affect ions under ~1 nm apart. If too close, a qubit ion can be removed by optical pumping. Spectral overlap of excitation wavelengths can cause issues, such as a possible overlap between Eu's main line at 580 nm and Nd's excitation. In the Y_2SiO_5 host, there are two usable sites with typical wavelength differences in the nm range [108], likely ensuring at least one site will work. For Er or Pr, no overlap is expected, but further investigation on cross-species transfers would be useful for quantum information.

The qubit and readout species can be integrated into the microcavity using nanocrystals or thin films. Smaller nanoparticles maintain single qubit spectral selectivity while enabling numerous interacting qubits due to the high concentration of dopants. However, a significant challenge associated with nanoparticles is their susceptibility to considerable extra dephasing processes ($T_2/T_{2,\ \mathrm{bulk}} \approx 10^{-3}$). Conversely, a bulk crystal thinned down to about 10 µm, which has been realized in Ref [87], would contain about 10^4 more ions than a nanoparticle, thus providing more potential qubits but also making addressing single ions more difficult. This issue suggests that a polished down bulk YSO crystal can better meet the requirements of good optical T_2, since it appear to retain the coherence properties close to that of bulk crystals [87].

8.2 Readout

The fundamental aspect of the readout scheme involves multiple qubit ions being coupled through dipole interactions to a distinct readout ion as discussed in Section 2.1.5. The emission from this readout ion is enhanced by the Purcell effect through a cavity, which helps to address the issue of weak fluorescence.

To evaluate the readout impact on a quantum computer, it's essential to consider both readout fidelity and duration, ensuring the process doesn't degrade compared to standard gate operations. As discussed in Section 7.3, using Eu^{3+} with a 2 ms lifetime achieves about 99% readout fidelity over 10 μs as shown in Paper II, limited by spontaneous decay of the qubit ion during detection. Introducing a buffer ion [91] increases fidelity to 99.9%, but extends detection time to 40 μs, with fidelity primarily constrained by decay during the transfer pulse between the qubit and buffer ion.

To attain high readout fidelity, it is essential to have a well-isolated readout ion during excitation to accurately differentiate between qubit states, as well as a high detection rate through Bayesian analysis [92]. The first requirement can be addressed by optimizing the doping concentration of the qubit ion, ensuring that a sufficient number of qubit ions interact strongly with the readout ion. Additionally, the detection rate can be increased by leveraging high Purcell enhancement of the readout ion transition and improving the optical detection efficiency. Drawing from the insights obtained in the preceding chapters, I will address the challenges associated with the current setup and propose potential enhancements.

8.2.1 Purcell enhancement: challenges and improvements

- Challenges

A qubit state readout with high fidelity may optimally use a readout ion lifetime down to 100 ns, as outlined in Paper II. This lifetime corresponds to a maximum shifting bandwidth of 10 MHz, which is expected between two ions that are closely spaced ~5nm apart. A detection rate of 10^6 photons/second is expected, assuming a reasonable optical efficiency of 10%. This detection rate is high enough to differentiate between the qubit states. In our investigations involving Nd^{3+} ions, we observed a lifetime of roughly 540 μs in free space, absent of a cavity (see Paper

II). This suggests that a Purcell enhancement of about 5000 is necessary to attain this reduction in lifetime (100 ns). Based on Eq. (3.22), such an enhancement necessitates a cavity finesse of 3×10^5.

There are two main challenges to consider regarding this high finesse. The first challenge relates to cavity finesse, which is limited by the total losses from the cavity mirrors, including factors such as absorption and surface roughness, as well as scattering caused by nanoparticles. This scattering is proportional to the sixth power of the nanoparticle radius, as outlined in Eq. (7.5). The second challenge focuses on the mechanical stability required to realize a substantial effective Purcell effect with time averaging due to cavity length fluctuations. The situation is particularly challenging when the system is connected to the noisy closed-cycle cryostat described in Section 6.7.

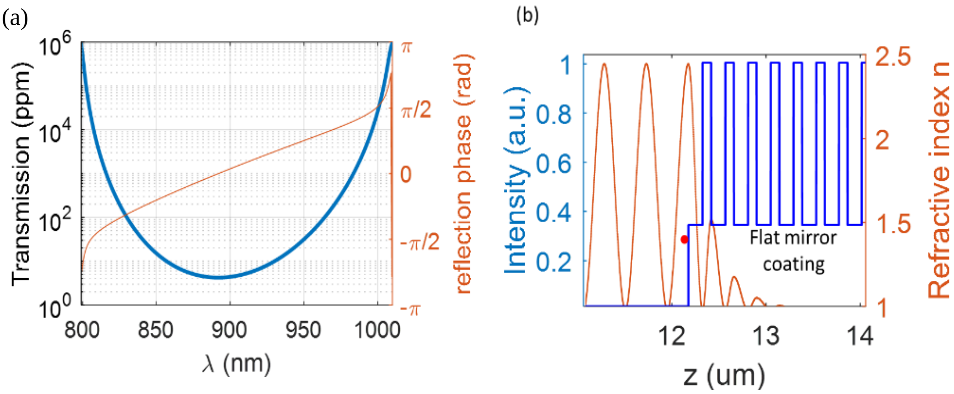

Figure 8.2: (a) The simulation of a λ/4 Bragg mirror with 23-layer pairs of Ta_2O_5 and SiO_2 demonstrates high reflectivity (4 ppm transmission) near the design wavelength of 892 nm, with a near linear phase (orange) at the surface across various wavelengths. (b) shows the refractive index profile (blue) and electric field intensity distribution (orange) inside the microcavity, with red dots indicating the nanocrystal's position and size.

- Improvements

Mirror coatings: Enhancing the parameters of the mirrors is essential for increasing the finesse of the cavity and improving the resolution of scanning cavity microscopy (SCM) utilized for identifying nanoparticles (see Section 7.4) allowing for using small nanoparticle sizes. In the measurements outlined in Section 7.5.1, the resolution of the SCM was constrained to approximately 70 nm in radius, which was associated with a scattering loss from the mirror's roughness of around 8 ppm. By employing a mirror that exhibits a scattering loss of under 2 ppm[12] (with

[12] Based on discussion with LaerOptik it is possible to have roughness <0.1nm, called super polished. Expected scattering losses is 2ppm for super-polished substrates.

roughness less than 0.1 nm), it becomes possible to detect nanoparticles with a radius of 38 nm. By applying Eq. (7.2), it is possible to attain a cavity finesse of 3×10^5 using 38 nm nanoparticles and a mirror scattering loss of 2 ppm. To achieve this, a mirror with T + A ≤ 8 ppm is necessary, where T represents the mirror transmission and A denotes the mirror absorption. Figure 8.2a illustrates a model for new mirror coatings designed to achieve a transmission of 4 ppm at 892 nm for the redout ion transition. This coating type demonstrates negligible absorption loss, with a practical value of A = 2 ppm. Additionally, the reflection phase can be optimized to create field maxima at the 38 nm nanoparticle radius spin-coated to the flat mirror (see Section 6.1.2), thereby improving interaction, as depicted in Fig. 8.2b. One challenge with nanoparticles is making them with such small radius, although down to 30 nm radius has been demonstrated [109]. Otherwise, thin films with small surface roughness will work.

Mechanical stability: The other challenge associated with utilizing such high finesse is ensuring the mechanical stability of the setup, which can lead to time averaging of the Purcell effect, thereby diminishing the effective enhancement. The resonance linewidth corresponding to the finesse of 3×10^5 is given by $\delta d = (\lambda/2\mathcal{F}) =$1.5 pm, so in order to be substantially below this we should aim for a root mean square (rms) of about 0.15 pm. This is two orders of magnitude smaller than the 15 pm rms used in the measurements presented in Chapter 6, which is challenging but possible.

Our cavity design may reach this degree of stability through enhancements in the feedback circuit bandwidth utilized for active stabilization, along with a novel method to mitigate noise from the closed-cycle cryostat. As outlined in Paper I, increasing the closed-circuit bandwidth from 3 kHz to 80 kHz can reduce the rms length fluctuation to 0.15 pm, which is essential for achieving a Purcell enhancement of 5000. This stability enhancement is anticipated in the absence of the closed-cycle cryostat. Operating in a noisy environment may increase the rms fluctuations by approximately one order of magnitude.

The spring system designed to mitigate noise transmitted to the cavity from the cryostat (refer to Section 5.5.3) can be adjusted to address multiple frequency components affecting the cavity. Additionally, a feedforward technique can effectively reduce the prominent peak associated with the cryocooler, which occurs at approximately 47.7 Hz. This method utilizes an accelerometer mounted on the 1K cell (see Section 2.2), with the resulting electronic signal directed to a larger scanner (z-attocube) that regulates the cavity length (see Section 5.5.2). By integrating the signal from the accelerometer with the PID controller and a bandpass filter, it appears from preliminary data that the 47.7 Hz noise from the cryocooler can be reduced by roughly an order of magnitude when combined with the aforementioned spring system.

In addition to the enhancement and the mechanical stability, the optical coupling efficiency can also be improved, which I will describe next.

8.2.2 Optical coupling efficiency

Our configuration encounters two challenges regarding coupling efficiency. The first challenge pertains to the coupling of higher order modes (HOMs), which serve as the stabilizing beam to the cavity mode via the flat mirror. The second challenge relates to the coupling between the cavity mode and the single-mode fiber, a critical component for fluorescence collection.

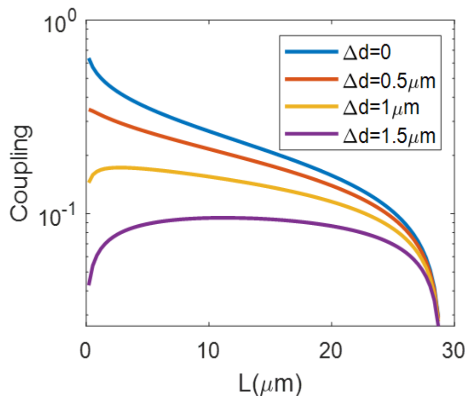

Figure 8.3: Coupling efficiency between cavity mode and the single mode fiber at different deviation distances between the center of the concave mirror and the fiber core.

Coupling of HOMs: The current challenge in utilizing higher-order modes to stabilize cavity length and reduce error photons is the clipping loss that occurs because the large beam size of HOMs is limited by the finite cut-off diameter of the fiber mirror (see Section 4.4). This aspect is essential when employing higher-order modes for stabilization, as the effectiveness of cavity length stabilization depends on the slope of the fringe side used for this purpose.

The maximum cut-off diameter of the fiber mirror may be constrained when employing single-laser pulses for end-face machining. However, this limitation can be addressed by adopting a multiple-pulse technique [110]. This method has successfully achieved a cut-off diameter of approximately 100 µm while maintaining minimal overall losses, leading to a finesse of 10^5. To efficiently couple higher-order modes to the TEM_{90} cavity mode without compromising finesse due to clipping loss, a minimum cut-off diameter of 30 µm is necessary. This improvement will reduce clipping losses, thereby maintaining finesse and enabling the suppression of error photons from the stabilization beam, by a factor of 10^4. Consequently, this reduces the dependence on optical filters, which can cause some loss in the detected fluorescence, while also increasing the fluorescence signal relative to the background, thereby facilitating the differentiation between qubit states.

Coupling to single mode fiber (SMF): Two parameters that need optimization govern the coupling to the single-mode fiber: the outcoupling efficiency and the overlap between the cavity mode and the SMF. Improving the mirror parameters discussed in the previous section, while making sure that the mirror transmission exceeds other losses (absorption and scattering), can result in a higher outcoupling efficiency. This enhancement optimizes the coupling to the single-mode fiber and the higher-order modes (HOMs) that are coupled through the flat mirror and utilized for stabilization. As a result, there is a significant reduction in locking power by several orders of magnitude. This advancement contributes to the reduction of error photons from the stabilizing beam while providing improved stability, as outlined in Paper I.

An additional critical parameter that requires improvement is the deviation distance between the center of the concave mirror and the fiber core (Δd). Minimizing this distance is essential to improve the high coupling efficiency between the cavity and the fiber, which is necessary for high-fidelity readout ions as discussed in Section 7.3. Currently, fibers with deviation distances Δd ranging from 0.2 to 1.5 µm are utilized. As illustrated in Fig. 8.3, a notable loss in coupling for the TEM_{00} mode was observed.

The last important parameter that requires improvement is the mode-matching efficiency between the cavity mode and the single mode fiber, which is influenced by the overlap between the cavity mode and the fiber transmission mode. As illustrated in Fig. 8.3, short cavities can achieve a high mode-matching efficiency compared to long cavities when utilizing standard single-mode fiber. For short cavity lengths, a maximum coupling efficiency of approximately 25% can be attained, indicating a need for improvement. This issue can be enhanced by specially designed integrated mode-matching optics. For instance, splicing graded-index (GRIN) fibers with multimode fibers [111] can significantly enhance mode-matching at longer cavity lengths, achieving up to 90% efficiency. This improvement can lead to better outcoupling efficiency between the cavity mode and the detectors, thereby improving the detection efficiency.

The integration of the previously suggested improvements to our system allows for the effective detection of single ions at the high detection rate required for quantum computing. Even before such a high rate is achieved, we can measure the dipole-dipole interaction between the Nd^{3+} and Pr^{3+} ions. This measurement will be crucial for assessing our advancement in obtaining a high-fidelity readout of the state of nearby qubit ions via the dipole-blockade mechanism described in Section 2.1.5.

8.3 Single-qubit gate operation

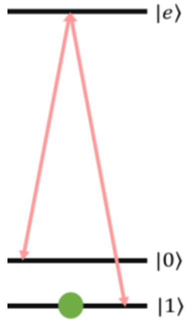

Figure 8.4: shows a lambda system where the qubit states are the two ground states.

Gate operations are carried out via an optically excited state. Single-qubit gate operations utilize a two-color pulse, which consists of a pair of frequencies resonant between the states |0⟩ and |e⟩, as well as |1⟩ and |e⟩ as shown in Fig. 8.4. This enables the excitation of any qubit superposition state to an optically excited state, followed by its de-excitation using a different phase state [112].

The fidelity of the gate decreases exponentially with the gate duration and can be approximated as $F \sim e^{-t_{dur}/T_{2,opt}}$. The primary requirement for high fidelity gates is a long optical T_2 together with high bandwidth ($\sim 1/t_{dur}$). The hyperfine T_2 needs to be sufficiently long, and since hyperfine dephasing affects the qubits at all times and not just during gates, the hyperfine T_2 should be much longer than the optical T_2. The reason for requiring a high gate fidelity is to ensure that quantum error correction, which used to mitigate the effects of errors (loss of fidelity) in quantum gates, can be used to recover all errors. The exact threshold for this depends on the error correction protocol but usually varies between 10^{-2}–10^{-4}. Using simulations of quantum error correction in a small REQC processor node it has been estimated that the hyperfine T_2 should be about a factor of 1000 longer than the optical T_2 for this to no longer be the main bottleneck during an algorithm [113].

Fast gates not only provide high fidelity but also ensure a reduced algorithm execution time. However, the speed of these gates is constrained by limitations on the available bandwidth, which can cause crosstalk errors. This phenomenon occurs when a light field is activated, potentially causing off-resonant transitions within the same ion, which can negatively impact qubit gate performance due to internal crosstalk. Furthermore, off-resonant excitation of ions that are not part of the qubit can lead to decoherence. Ions located near the qubit may undergo off-resonant excitation, which can affect the qubit through dipole interactions, resulting in rotations of the qubit Bloch vector and unintended entanglement, a process referred to as instantaneous spectral diffusion (ISD) or external crosstalk. Therefore, the gate bandwidth must be considerably lower than the frequency separation from other transitions, both within the ions and between different ions, as any overlap of the gate bandwidth with other transitions can lead to crosstalk. To mitigate these effects, qubit ions must be isolated in frequency space from non-qubit ions, limiting the number of addressable qubits and requiring longer pulse durations to avoid unwanted excitations, which slows down operations.

In summary, the reliability of single-qubit gates is influenced by both the characteristics of the materials used and various trade-offs, such as the impact of ISD and the number of qubits within a processor node. Given these limitations, simulations of the Lindblad master equation [114, 115] conducted on multi-level single ions predict a single-qubit gate fidelity error of approximately 3×10^{-4} for a realistic rare-earth-ion qubit. This level of gate error is within the threshold that necessary for error correction.

8.3.1 Integrated cavity with a thin film.

On the longer term, thin films are better candidates for quantum computing materials than nanocrystals, due to avoided difficulties of scattering from the particles and because much better coherence properties have been achieved in thin films. Thin films are therefore a superior option for achieving high gate fidelity. Recently, we obtained a single crystalline membrane of YSO, doped with 0.01% Nd^{3+}, that was attached to a mirror with a reflectivity of 99.9%, by the group of Roman Kolesov from Stuttgart, Germany. With a thickness of around 10 μm, the membrane is suitable for studies involving ion ensembles. The surface flatness is about 0.2 nm rms and it would thus be beneficial to examine this material using the previously mentioned cavity, which would not only evaluate this innovative sample preparation method but also allow for an assessment of the properties of Nd^{3+} within the YSO host membrane. Following a successful test of this, we envision an optimal material for high fidelity gates to be a thin film (as thin as possible) with only trace amounts of the readout ion, but with a high doping concentration of the qubit ion to achieve high qubit densities.

8.4 Two-qubit gate operation

The permanent dipole moment that previously contributed to the excitation-induced frequency shift discussed in Section 2.1.5 also plays a significant role in facilitating qubit-qubit interactions. In fact, Fig 2.3 that describes conditional readout, also describes conditional gates with the same mechanism. The concept involves finding a control qubit that shifts the target qubit's center frequency beyond the gate operation bandwidth, preventing laser pulse interactions with it and enabling conditional operations between the two qubits. Two-qubit gates using rare-earth ions can be executed with fidelity errors in the order of 10^{-3} [114], taking into account crosstalk and bandwidth limitations similar to single-qubit gates. The higher error is due to a longer total gate sequence duration.

To optimize gate fidelity, there are several steps to consider: i) perform optical pumping to minimize ISD. An optical pumping scheme can be used to selectively transfer ions into other hyperfine spin states that are further away in frequency from the gate transition, thereby minimizing crosstalk. ii) Limit the number of qubits in a node and their connectivity. This allows more bandwidth to be allocated to each gate operation and can thus reach a higher fidelity. iii) optimize pulse parameters to minimize decoherence and internal crosstalk. For instance, complex pulse schemes [116] can be used to minimize internal crosstalk errors.

8.5 Processor nodes

The dipole-blockade mechanism allows for the sequential identification of ions that influence the readout ion and other controlling ions, revealing a network of interconnected ions that can serve as a processor node (See Fig.8.1).

The number of qubits in such a local node is limited by material properties and laser technology. To achieve a large number of qubits in a single processor node, a large addressable inhomogeneous width is required. This width can be broadened through high doping concentration [13], co-doping with defect species [117], applying external fields with electrodes to the crystal, or by mechanical pressure. For example, using Eu^{3+} doped YSO with a concentration of 5%, a width of 100 GHz addressable inhomogeneous profile can be achieved. Simulations indicate that a local processor node could contain around 100 qubits with these conditions [28].

8.6 Many nodes

Processor nodes can scale by connecting readout ions in cavities to similar nodes, if they can be entangled with high fidelity, using e.g., entangling swapping techniques [9]. This scaling technique is similar to other quantum computing schemes, such as trapped ions [118] and other defect centers. This is advantageous because any techniques developed for these other platforms will be directly usable in the RE case. Although the REQC efforts are still far from reaching this step, entangling swapping techniques are also crucial for quantum repeater schemes, and here the rare-earth efforts have been very successful [119, 120]. If the improved readout parameters that I discussed in Sec. 8.2 are reached, then the entangling rate used to connect multiple nodes will also be correspondingly high, since it depends on these emitted photons. For a theoretical example of what can be achieved with a rare-earth entangling swapping scheme based on single ions, see [121].

Acknowledgments

I would like to sincerely thank my primary supervisor, Andreas Walther, for his steadfast support, encouragement, and patience, as well as for always being available for discussions. I am grateful for the freedom I was given to explore my interests. I also want to express my appreciation to my co-supervisor, Adam Kinos, for his willingness to help and engage in meaningful conversations during writing thesis. Additionally, I am thankful to Stefan Kröll for his support, for reviewing my thesis, and for creating a positive atmosphere within the group. My gratitude extends to Lars Rippe for his creative ideas and valuable discussions. I appreciate the members of the quantum information group—Mohammed Alqedra, Johan Renders, David Gustavsson, Marcus Linden, and Safi Rafie-Zinedine—for contributing to a collegial work environment, as well as for the enjoyable lunches, coffee breaks, and assistance in the lab.

I would like to take this opportunity to express my appreciation for the international collaborators with whom I have had the privilege to work, particularly David Hunger and his team. I extend my gratitude to Philipe Goldner and Diana Serrano for supplying the nanocrystals used in this research and for their initial characterizations. I also thank Hugues de Riedmatten and Chetan Deshmukh for their collaboration on the spectroscopy manuscript and for their insightful discussions regarding the cavity project. My thanks go to Michael Meyer and Håkan Ivansson for their assistance in machining various mechanical components utilized in this study. I am also grateful to my colleagues in the Atomic Physics Division for their support, including Nina Reistad and Anders Persson for lending their equipment, Anne Petersson Jungbeck for her help with administrative matters, Maria Algotsson for her assistance with financial issues, Åke Johansson for managing all computer-related tasks, and all division members for fostering a positive work environment. Lastly, I wish to convey my heartfelt gratitude to my parents, Sabah and Shehata, for their constant support and encouragement, and to my wife Salma and my children Yahia, Younis, and Laila for their unwavering support throughout my studies.

References

1. *Copenhagen Interpretation*, (1930).
2. D. P. DiVincenzo. *The Physical Implementation of Quantum Computation.* Fortschr. Phys. **48**, 771–783 (2000).
3. R. P. Feynman. *Simulating physics with computers.* Int. J. Theor. Phys. **21**, 467–488 (1982).
4. T. Manovitz, Y. Shapira, L. Gazit, N. Akerman, and R. Ozeri. *Trapped-Ion Quantum Computer with Robust Entangling Gates and Quantum Coherent Feedback*. PRX Quantum. **3**, 010347 (2022).
5. S. l Kwon, A. Tomonaga, G. L. Bhai, S. J. Devitt, J. S. Tsai. *Gate-based superconducting quantum computing*. J. Appl. Phys. **28** January 2021; 129 (4): 041102.
6. S. Pezzagna, J. Meijer. *Quantum computer based on color centers in diamond*. Appl. Phys. Rev. **8** (1): 011308, (2021).
7. Chien-An Wang et al. *Operating semiconductor quantum processors with hopping spins*. Science. **385**, 447-452 (2024).
8. M. Akhtar et al. *A high-fidelity quantum matter-link between ion-trap microchip modules*. Nat Commun. **14**, 531 (2023).
9. A. Kinos, D. Hunger, R. Kolesov, K. Mølmer, H. de Riedmatten, P. Goldner, A. Tallaire, L. Morvan, P. Berger, S. Welinski, K. Karrai, L. Rippe, S. Kröll and A. Walther. *Roadmap for Rare-earth Quantum Computing*. **arXiv** (2021).
10. N. Ohlsson, R K. Mohan, S. Kröl. *Quantum computer hardware based on rare-earth-ion-doped inorganic crystals*. Optics Communications, **201**:71–77, (2002).
11. L. Rippe, B. Julsgaard, A. Walther, Yan-Ping Ying, and S. Kröll. *Experimental quantum-state tomography of a solid-state qubit*. Physical Review A, **77**:022307, (2008).
12. M. K. Singh et al. *Rare earth based solid-state qubit platforms*. IEDM, San Francisco, CA, USA, 2022, pp. 14.2.1-14.2.4.
13. F. Könz, Y. Sun, C. W. Thiel, R. L. Cone, R. W. Equall, R. L. Hutcheson and R. M. Macfarlane. *Temperature and concentration dependence of optical dephasing, spectral-hole lifetime, and anisotropic absorption in* Eu^{3+}*:* Y_2SiO_5. Phys. Rev. B, **68**, 085109 (2003).
14. A. Walther. *Coherent Processes in Rare-Earth-Ion-Doped Solids.* PhD thesis Atomic Physics, LTH (2009).
15. M. Alqedra. *Towards Single-Ion Detection and Single Photon-Storage in Rare-Earth-Ion-Doped Crystals*, PhD thesis, Atomic Physics, LTH (2022).
16. E. M. Purcell. *Spontaneous emission probabilities at radio frequencies*. Phys. Rev.**69**: 681 (1946).
17. H. J. Kimble. *The quantum internet*, Nature **453**, 1023 (2008).

18. D. Hunger, T. Steinmetz, Y. Colombe, C. Deutsch, T. W. Hänsch, and J. Reichel. *Fiber Fabry-Perot cavity with high finesse*. New J. Phys. **12**, 065038 (2010).
19. J.M. Kindem, A. Ruskuc, J.G. Bartholomew, J. Rochman, Y.Q. Huan, A. Faraon. *Control and single-shot readout of an ion embedded in a nanophotonic cavity*. Nature, **580**, 201–204 (2020).
20. T. Asano, Y. Ochi, Y. Takahashi, K. Kishimoto, and S. Noda. *Photonic crystal nanocavity with a Q factor exceeding eleven million*. Opt. Express **25**, 1769-1777 (2017).
21. J. Sung, D. Shin, H. Cho, S. W. Lee, S. Park, Y. D. Kim, J. S. Moon, J. H. Kim, and S. H. Gong. *Room-temperature continuous-wave indirect-bandgap transition lasing in an ultra-thin WS2 disk*. Nat. Photonics **16**(11), 792 (2022).
22. M. Mader, J. Reichel, T. W. Hänsch, and D. Hunger. *A scanning cavity microscopy*. Nat. Commun. **6**, 7249 (2015).
23. S. Bogdanović, S. B. van Dam, C. Bonato, L. C. Coenen, A.-M. J. Zwerver, B. Hensen, M. S. Z.Liddy, T. Fink, A. Reiserer, M. Lončar, and R. Hanson. *Design and low-temperature characterization of a tunable microcavity for diamond-based quantum networks*. Appl. Phys. Lett. **110**, 171103 (2017).
24. S. Vadia, J. Scherzer, H. Thierschmann, C. Schäfermeier, C. Dal Savio, T. Taniguchi, K. Watanabe, D. Hunger, K. Karrai, and A. Högele. *Open-cavity in closed-cycle cryostat as a quantum optics platform*. PRX Quantum. **2**, 040318 (2021).
25. M. Pallmann, T. Eichhorn, J. Benedikter, B. Casabone, T. Hümmer, and D. Hunger. *A highly stable and fully tunable open microcavity platform at cryogenic temperatures*. APL Photonics. **8**, 046107 (2023).
26. P. R. Dolan, G. M. Hughes, F. Grazioso, B. R. Patton, and J. M. Smith. *Femtoliter tunable optical cavity arrays*. Opt. Lett. **35**, 3556 (2010).
27. L. Greuter, S. Starosielec, D. Najer, A. Ludwig, L. Duempelmann, D. Rohner, and R. J. Warburton. *A small volume tunable microcavity: Development and characterization*. Appl. Phys. Lett. **105**, 121105 (2014).
28. A. Kinos, L. Rippe, D. Serrano, A. Walther, and S. Kröll, *High-connectivity quantum processor nodes using single-ion qubits in rare-earth-ion-doped crystals*. Phys. Rev. A, **105**, 032603, (2022).
29. M. Gündoğan, P. M. Ledingham, K. Kutluer, M. Mazzera, and H. de Riedmatten, *Solid state spin-wave quantum memory for time-bin qubits*. Phys. Rev. Lett., **114**, 230501, (2015).
30. M. Afzelius, C. Simon, H. de Riedmatten, and N.Gisin, *Multimode quantum memory based on atomic frequency combs*. Phys. Rev. A **79**, 052329.
31. M. Zhong, R. L. Ahlefeldt and M. J. Sellars, *Quantum information processing using frozen core Y^{3+} spins in Eu^{3+}: Y_2SiO_5*. New Journal of Physics. **033019**, (2019).
32. Y. Li, H. Zhang, C. Kim, K. H. Wagner, P. Hemmer, and L. V. Wang, *Pulsed ultrasound-modulated optical tomography using spectral-hole burning as a narrowband spectral filter*. Appl. Phys. Lett., **93**, 011111, (2008).
33. H. Zhang, M. Sabooni, L. Rippe, C. Kim, S. Kröll, L. V. Wang, and P. R. Hemmer, *Slow light for deep tissue imaging with ultrasound modulation*. Appl. Phys. Lett., **100**, 131102, (2012).
34. Xiao Xu, Sri-Rajasekhar Kothapalli, Honglin Liu, and Lihong V. Wang, *Spectral hole burning for ultrasound-modulated optical tomography of thick tissue*. J. Biomed. Opt., **15**, 1–5, (2010).

35. C. Venet, M. Bocoum, J.-B. Laudereau, T. Chaneliere, F. Ramaz, and A. Louchet-Chauvet, *Ultrasound-modulated optical tomography in scattering media: flux filtering based on persistent spectral hole burning in the optical diagnosis window*. Opt. Lett., **43**, 3993, (2018).
36. D. Hill, A. Bengtsson, T. Erlöv, M. Cinthio, and S. Kröll, *Acousto-optic interaction strengths in optically scattering media using high pressure acoustic pulses*, Biomed. Opt. Express, **12**, 3196, (2021).
37. Q. Zhan, J. Qian, H. Liang, G. Somesfalean, D. Wang, S. He, Z. Zhang, and S. Andersson-Engels, *Using 915 nm Laser Excited Tm3+ /Er3+ /Ho3+ -Doped NaYbF4 Upconversion Nanoparticles for in Vitro and Deeper in Vivo Bioimaging without Overheating Irradiation*. ACS Nano, **5**, 3744– 3757, (2011).
38. P. B. Sellin, N. M. Strickland, J. L. Carlsten, and R. L. Cone, *Programmable frequency reference for subkilohertz laser stabilization by use of persistent spectral hole burning*. Opt. Lett., **24**, 1038, (1999).
39. T. Böttger, G. J. Pryde, and R. L. Cone, "*Programmable laser frequency stabilization at 1523 nm by use of persistent spectral hole burning*," Opt. Lett., vol. **28**, p. 200, (2003).
40. M. J. Thorpe, L. Rippe, T. M. Fortier, M. S. Kirchner, and T. Rosenband, "*Frequency stabilization to 6 × 10−16 via spectral-hole burning*. Nat. Photonics, **5**, pp. 688–693, (2011).
41. S. P. Horvath, C. Shi, D. Gustavsson, A. Walther, A. Kinos, S. Kröll, and L. Rippe, "*Slow light frequency reference cavities - proof of concept for reducing the frequency sensitivity due to length fluctuations*," New J. Phys., Feb. 2022.
42. O. Gobron, K. Jung, N. Galland, K. Predehl, R. Le Targat, A. Ferrier, P. Goldner, S. Seidelin, and Y. Le Coq, "*Dispersive heterodyne probing method for laser frequency stabilization based on spectral hole burning in rare-earth doped crystals*," Opt. Express, vol. **25**, p. 15539, June (2017).
43. D. Gustavsson. *Laser frequency stabilization using a slow light cavity*. *Atomic Physics*. PhD Thesis, Department of Physics, Lund University, (2024).
44. A. Kinos. *Light-matter interaction and quantum computing in rare-earth-ion-doped crystals*. PhD Thesis, Department of Physics, Lund University, (2018).
45. H. Syed. *Nuclear spin interactions and coherent control in rare-earth-ion-doped crystals for quantum computing*. PhD Thesis, Department of Physics, Lund University, (2022).
46. M. Zhong, M. P. Hedges, R. L. Ahlefeldt, J. G. BartholomewS. E. Beavan, S. M. Wittig, J. J. Longdell and M. J. Sellars. *Optically addressable nuclear spins in a solid with a six-hour coherence time*. Nature **517**, 177–180 (2015).
47. B. M. Walsh, J. M. McMahon, W. C. Edwards, N. P. Barnes, R. W. Equall and R. L. Hutcheson. *Spectroscopic characterization of Nd: Y2O3: application toward a differential absorption lidar system for remote sensing of ozone*. J. Opt. Soc. Am. B, JOSAB **19**, 2893–2903 (2002).
48. R. Macfarlane and R. Shelby,*Sub-kilohertz optical linewidths of the 7F0 - 5D0 transition in Y_2O_3:Eu^{3+}*. Optics Communications, **39**, 169–171, (1981).
49. T. Zhong, J. Kindem, J. G. Bartholomew, J. Rochman, I. e. a. Craiciu and A. Faraon, *Optically addressing Single Rare-Earth Ions in a Nanophotonic Cavity*," Phys. Rev. Lett, **121**, 183603, (2018).

50. C. Deshmukh, E. Beattie, B. Casabone, S. Grandi, D. Serrano, A. Ferrier, P. Goldner, D. Hunger, and H. de Riedmatten. *Detection of single ions in a nanoparticle coupled to a fiber cavity*. Optica **10**, 1339-1344 (2023).
51. E. T. Jaynes and F. W. Cummings. *Comparison of Quantum and Semiclassical Radiation Theories with Application to the Beam Maser*. In Proc. IEEE, **51**, no. 1, pp. 89–109, (963).
52. E. B. Davies. *Quantum Theory of Open Systems*. Academic Press, New York, (1976).
53. Pierre-Antoine Bourdel. *Atomic ensembles in a microcavity: from cavity protection to single atom control*. Ph.D. Thesis, Atomic Physics. Sorbonne Université, (2022).
54. G. Hechenblaikner, M. Gangl, P. Horak and H. Ritsch. *Cooling an atom in a weakly driven high-Q cavity*. Phys. Rev. A **58**, pp. 3030–3042 (1998).
55. C. J. Foot and D. Of Physics Christopher J. Foot. *Atomic Physics*. OUP Oxford, England, UK (2005). ISBN 978- 0-19850695-9.
56. Y. Fontana, R. Zifkin, E. Janitz, C. D. Rodríguez Rosenblueth, and L. Childress. *A mechanically stable and tunable cryogenic Fabry–Pérot microcavity*. Rev. Sci. Instrum. **92**, 053906 (2021).
57. M. Pallmann, T.Eichhorn, J. Casabone, T. Hümmer, D. Hunger. *A highly stable and fully tunable open microcavity platform at cryogenic temperatures*. APL Photonics, **8** (4): 046107 (2023).
58. T. Steinmetz, Y. Colombe, D. Hunger et al. *Stable fiber-based Fabry-Pérot cavity*. Appl. Phys. Lett. **89**, 111110 (2006).
59. D. Hunger, C. Deutsch, R.J. Barbour, R.J. Warburton, J. Reichel. *Laser micro-fabrication of concave, low-roughness features in silica*. AIP Adv. **2**, 012119 (2012).
60. S. Garcia, F. Ferri, K. Ott, J. Reichel, R. Long. *Dual-wavelength fiber Fabry–Perot cavities with engineered birefringence*. Opt. Express **26**, 22249 (2018).
61. J. Benedikter, H. Kaupp, T. Hümmer, Y. Liang, A. Bommer, C. Becher, A. Krueger, J. M. Smith, T. W. Hänsch, D. Hunger. *Cavity-Enhanced Single-Photon Source Based on the Silicon-Vacancy Center in Diamond*. Phys. Rev. Applied **7**, 024031 (2017)
62. H.V. Baghdasaryan, T.M. Knyazyan, T.H. Baghdasaryan, B. Witzigmann, F. Roemer. *Absorption loss influence on optical characteristics of multilayer distributed Bragg reflector: wavelength-scale analysis by the method of single expression*. Opto-Electron. Rev. **18**, 438–445 (2010).
63. C. Koks and M. P. van Exter. *Microcavity resonance condition, quality factor, and mode volume are determined by different penetration depths*. Opt. Express **29**, 6879-6889 (2021)
64. Svelto, O.: *Passive Optical Resonators. In: Principles of Lasers*. Springer, US, pp. 173–186, (2010).
65. T. Hümmer. *Cavity-enhanced hyperspectral Raman and Absorption Microscopy*. PhD thesis München (2019).
66. Siegman, Anthony E. *Lasers*. University Science Books, (1986).
67. Dana Z. Anderson. *Alignment of resonant optical cavities*. Appl. Opt. **23**, 2944-2949 (1984).
68. J. Benedikter, T. Hümmer, M. Mader, B. Schlederer, J. Reichel, T. W. Hänsch, and D. Hunger. *Transverse-mode coupling and diffraction loss in tunable fabry–pérot microcavities*. New J. Phys. **17**, 053051 (2015).
69. M. Uphoff, M. Brekenfeld, G. Rempe and S. Ritter. *Frequency splitting of polarization eigenmodes in microscopic Fabry–Perot cavities*. New J. Phys. **17**, 013053 (2015).

70. D. Marcuse. *Loss analysis of single-mode fiber splices*. Bell Sys. Tec. J. **56**(5): 703–18 (1977).
71. A. Nüßlein. *A Fabry–Pérot Cavity for Rare-Earth-Ion-Doped Nanocrystals*. M.Sc. Thesis, (2018).
72. E. D. Black. *An introduction to Pound–Drever–Hall laser frequency stabilization*. Am. J. Phys. **69** (1): 79–87 (2001).
73. R. W. P. Drever, J. L. Hall, F. V. Kowalski, J. Hough, G. M. Ford, A. J. Munley, and H. Ward. *Laser phase and frequency stabilization using an optical resonator*. Appl. Phys. B, **31**(2):97–105, (1983).
74. B.J.J. Slagmolen, D.A. Shaddock, M.B. Gray, and D.E. McClelland. *Frequency stability of spatial mode interference (tilt) locking*. in IEEE Journal of Quantum Electronics, **38**, 1521-1528, (2002).
75. N. Chabbra, A. R. Wade, E.R. Rees, A. J. Sutton, A. Stochino, R. L. Ward, D. A. Shaddock, and K. McKenzie. *High stability laser locking to an optical cavity using tilt locking*. Opt. Lett. **46**, 3199-3202 (2021).
76. J. Hansen. *Active stabilization of a micro-sized fibre cavity using tilt locking to enable quantum operations on single ions*. M.Sc. Thesis, (2021).
77. M. Fisicaro, M. Witlox, H. van der Meer, W. Löffler. *Active stabilization of an open-access optical microcavity for low-noise operation in a standard closed-cycle cryostat*. *Rev. Sci. Instrum.* **95** (3): 033101 (2024).
78. Kiwamu Izumi. *Cavity response in transmission*. paper, Dept. of Astronomy, Univ. of Tokyo (2017).
79. Martin Regehr. *Signal Extraction and Control for an Interferometric Gravitational Wave Detector*. Ph.D. Thesis, California Institute of Technology (1995).
80. C. L. Mueller. *Techniques for resonant optical interferometry with applications to the advanced LIGO gravitational waves detectors*. Ph.D. Thesis, Florida university (2014). Pages 65-76.
81. R. W. Fox, C. W. Oates, and L. W. Hollberg. *Stabilizing diode lasers to high-finesse cavities*. Exp. Methods Phys. Sci., **40**, 1–46, (2003).
82. M. L. Gorodetsky. *Thermal noises and noise compensation in high-reflection multilayer coating*. Phys. Lett. A **372**, 6813 (2008).
83. J. F. S. Brachmann, H. Kaupp, T. W. Hänsch, and D. Hunger. *Photothermal effects in ultra-precisely stabilized tunable microcavities*. Opt. Express **24**, 21205-21215 (2016).
84. Almtireen, N., Brandner, J.J. & Korvink, J.G. *Pulse Tube Cryocooler: Phasor Analysis and One-Dimensional Numerical Simulation*. J Low Temp Phys **199**, 1179–1197 (2020).
85. Manufacture tests.
86. L. Greuter, S. Starosielec, D. Najer, A. Ludwig, L. Duempelmann, D. Rohner, R. J. Warburton. *A small mode volume tunable microcavity: Development and characterization*. Appl. Phys. Lett. **105** (12): 121105 (2014).
87. B. Merkel, A. Ulanowski, and A. Reiserer. *Coherent and Purcell-Enhanced Emission from Erbium Dopants in a Cryogenic High-Q Resonator*. Phys. Rev. X **10**, 041025 (2020).
88. Y. Herrmann, J. Fischer, S. Scheijen, C. F. J. Wolfs, J. M. Brevoord, C. Sauerzapf, L. G. C. Wienhoven, L. J. Feije, M. Eschen, M. Ruf, M. J. Weaver, R. Hanson. *A low-temperature tunable microcavity featuring high passive stability and microwave integration*. AVS Quantum Sci. **6** (4): 041401 (2024).

89. T. Ruelle, D. Jaeger, F. Fogliano, F. Braakman, M. Poggio. *A tunable fiber Fabry–Perot cavity for hybrid optomechanics stabilized at 4 K*. Rev. Sci. Instrum. **93** (9): 095003 (2022).
90. J. Gallego et al. *High-finesse fiber Fabry–Perot cavities: stabilization and mode matching analysis*. Appl. Phys. B **122**, 47 (2016).
91. A. Walther, L. Rippe, Y. Yan, J. Karlsson, D. Serrano, A. N. Nilsson, S. Bengtsson and S. Kröll. *High-fidelity readout scheme for rare-earth solid-state quantum computing*. Phys.Rev. A **92**, 022319 (2015).
92. K. Debnath, A. H. Kiilerich and K. Mølmer. *Ancilla-mediated qubit readout and heralded entanglement between rare-earth dopant ions in crystals*. Phys. Rev. A **103**, 043705 (2021).
93. Y. Yan. *Towards single Ce ion detection in a bulk crystal for the development of a single-ion qubit readout scheme*. PhD thesis Lund University (2013).
94. Y. Yan, J. Karlsson, L. Rippe, A. Walther, D. Serrano, D. Lindgren, M.e. Pistol, S. Kröll, P. Goldner, L. Zheng and J. Xu. *Measurement of linewidths and permanent electric dipole moment change of the Ce 4f-5d transition in Y_2SiO_5 for qubit readout scheme in rare-earth ion-based quantum computing*. Phys. Rev. B **87**, 184 205 (2013).
95. J. Karlsson. *Cerium as a quantum state probe for rare-earth qubits in a crystal*. PhD thesis Atomic Physics (2015).
96. J. H. Wesenberg, K. Mølmer, L. Rippe, and S. Kröll. *Scalable designs for quantum computing with rare-earth-ion-doped crystals*. Phys. Rev. A **75**, 012304 (2007).
97. R. W. Equall, Y. Sun, R. L. Cone and R. M. Macfarlane. *Ultraslow optical dephasing in Eu^{3+}: Y_2SiO_5*. Phys. Rev. Lett. **72**, 2179–2182 (1994).
98. G. Heinze, C. Hubrich and T. Halfmann. *Stopped Light and Image Storage by Electromagnetically Induced Transparency up to the Regime of One Minute*. Phys. Rev. Lett. **111**, 033601 (2013).
99. R. W. Equall, R. L. Cone and R. M. Macfarlane. *Homogeneous broadening and hyperfine structure of optical transitions in Pr^{3+}: Y_2SiO_5*. Phys. Rev. B **52**, 3963–3969 (1995).
100. B. Casabone, J. Benedikter, T. Hümmer, F. Oehl, K. de Oliveira Lima, T. W. Hänsch, A. Ferrier, P. Goldner, H. de Riedmatten and D. Hunger. *Cavity-enhanced spectroscopy of a few-ion ensemble in Eu^{3+}: Y_2O_3*. New J. Phys. **20**, 095006 (2018).
101. A. Khalid, K. Chung, R. Rajasekharan, D. W. M. Lau, T. J. Karle, B. C. Gibson and S. Tomljenovic-Hanic. *Lifetime Reduction and Enhanced Emission of Single Photon Color Centers in Nanodiamond via Surrounding Refractive Index Modification*. Sci. Rep. **5**, 1–12 (2015).
102. M. J. Sellars, E. Fraval and J. J. Longdell. *Investigation of static electric dipole–dipole coupling induced optical inhomogeneous broadening in Eu^{3+}: Y_2SiO_5*. J. Lumin. **107**, 150–154 (2004).
103. D. Serrano, J. Karlsson, L. Zheng, Y. Dong, A. Ferrier, P. Goldner, A. Walther, L. Rippe and S. Kröll. *Satellite line mapping in Eu^{3+}– Ce^{3+} and Pr^{3+} – Ce^{3+} co-doped Y_2SiO_5*. J. Lumin. **170**, 102–107 (2016).
104. D. Serrano, C. Deshmukh, S. Liu, A. Tallaire, A. Ferrier, H. de Riedmatten and P. Goldner. *Coherent optical and spin spectroscopy of nanoscale Pr^{3+}: Y_2O_3*. Phys. Rev. B **100**, 144304 (2019).
105. F. R. Graf, A. Renn, G. Zumofen and U. P. Wild. *Photonecho attenuation by dynamical processes in rare-earth-iondoped crystals*. Phys. Rev. B **58**, 5462–5478 (1998).

106. M. Mader. *A Scanning Cavity Microscope*. PhD thesis München (2018).

107. G. Kumar, J. Lu, A. Kaminskii, K.-I. Ueda, H. Yagi and T. Yanagitani. *Spectroscopic and stimulated emission characteristics of Nd^{3+} in transparent Y_2O_3 ceramics*. IEEE Journal of Quantum Electronics **42**, 643–650 (2006).
108. Y. Alizadeh, J.P.R. Wells, M.F. Reid, A. Ferrier, and P. Goldner. *Laser site-selective spectroscopy of Nd^{3+}doped Y_2SiO_5*. Journal of Lumin. **234**, p. 117959 (2021).
109. T. Eichhorn, N. Jobbitt, S. Bieling, S. Liu, T. Krom, D. Serrano, R. Huber, U. Lemmer, H. de Riedmatten, P. Goldner, D. Hunger. *Multimodal Purcell enhancement and optical coherence of Eu3+ ions in a single nanoparticle coupled to a microcavity*. arXiv:2412.06576 [quant-ph].
110. Ott, K. et al. Millimeter-long fiber Fabry-Perot cavities. Opt. Express **24**, (2016).
111. Gulati, G. K., Takahashi, H., Podoliak, N., Horak, P. & Keller, M. *Fiber cavities with integrated mode matching optics.* Sci. Rep. **7**, 5556 (2017).
112. I. Roos and K. Mølmer. *Quantum computing with an inhomogeneously broadened ensemble of ions: Suppression of errors from detuning variations by specially adapted pulses and coherent population trapping*. Phys. Rev. A, **69**, p. 022321, (2004).
113. A. Rolander, A. Kinos and A. Walther. *Quantum error correction in the noisy intermediate-scale quantum regime for sequential quantum computing*. Phys. Rev. A, **105**, no. 6, p. 062604, (2022).

114. A. Kinos, L. Rippe, S. Kröll and A. Walther. *Designing gate operations for single-ion quantum computing in rare-earth-ion-doped crystals*. Phys. Rev. A, **104**, no. 5, p. 052624, (2021).
115. A. Kinos, L. Rippe, A. Walther and S. Kröll. *Microscopic treatment of instantaneous spectral diffusion and its effect on quantum gate fidelities in rare-earth-ion-doped crystals*. Physical Review A, **105**, p. 032608, (2022).
116. F. Motzoi, J. M. Gambetta, P. Rebentrost and F. K. Wilhelm. *Simple Pulses for Elimination of Leakage in Weakly Nonlinear Qubits*. Phys. Rev. Lett., **103**, no. 11, p. 110501, 9 (2009).
117. T. Böttger, C. W. Thiel, R. L. Cone and Y. Sun. *Controlled compositional disorder in Er^{3+}: Y_2SiO_5 provides a wide-bandwidth spectral hole burning material at 1.5 µm*. Physical Review B, **77**, no. 15, p. 155125, (2008).
118. C. Monroe and J. Kim. *Scaling the Ion Trap Quantum Processor*. Science, **339**, p. 1164–1169, (2013).
119. I. Usmani, C. Clausen, F. Bussières. *et al. Heralded quantum entanglement between two crystals*. Nature Photon **6**, 234–237 (2012).
120. A.Ruskuc, C. Wu, E. Green, S. L. N. Hermans, J. Choi, A. Faraon. *Scalable Multipartite Entanglement of Remote Rare-earth Ion Qubits*. arXiv:2402.16224 [quant-ph].
121. A. Kinos, A. Walther, S. Kröll, L. Rippe. *Complete analysis of a realistic fiber-based quantum repeater scheme.* arXiv:2309.04151 [quant-ph].

Printed by Media-Tryck, Lund 2025 NORDIC SWAN ECOLABEL 3041 0903

Faculty of Engineering, LTH
Department of Physics

Lund Reports on Atomic Physics, LRAP-582
ISBN 978-91-8104-366-2
ISSN: 0281-2762

9 789181 043662